Strategies for Mechanical Metamaterial Design

Proefschrift

ter verkrijging van
de graad van Doctor aan de Universiteit Leiden,
op gezag van Rector Magnificus prof. mr. C.J.J.M. Stolker,
volgens besluit van het College voor Promoties
te verdedigen op woensdag 10 April 2019
klokke 15:00 uur

door

Nitin Singh

geboren te Barnala, India

in 1991

Promotor

prof. dr. M.L. van Hecke

Promotiecommissie

prof. dr. M. Dijkstra (*Universiteit Utrecht*)
dr. J.T.B. Overvelde (*AMOLF, Amsterdam*)
prof. dr. E.R. Eliel
prof. dr. J.M. van Ruitenbeek

Nederlandse titel

Strategieën voor mechanische metamateriaalontwerp.

Casimir PhD series, Delft-Leiden, 2016-30
ISBN 978-90-8593-274-1
An electronic version of this thesis can be found at openaccess.leidenuniv.nl

The work presented in this thesis was conducted mainly at the NWO institute AMOLF, Amsterdam and partially at the Leiden Institute of Physics (LION), Leiden University and is part of an industrial partnership programme (IPP) *'Computational Sciences for Energy Research (CSER)'* started jointly in 2012 by the Shell Global Solutions International B.V., the Netherlands Organization for Scientific Research (NWO) and the Foundation for Fundamental Research on Matter (FOM).

For my family.

Contents

Chapter 1

Introduction

1.1 Introduction

A branch of metamaterials [1–3], mechanical metamaterials are carefully engineered artificial structures prominent for their exotic and tunable mechanical properties, which are often not associated with the natural materials. These properties are governed by the macro-, micro- or nanoscale architecture and arrangement of the constituting unit cells, rather than directly by the (chemical) composition of the material. Often, these properties arise from the finite number of internal soft degrees-of-freedom in the system that govern the allowed deformations. In the last two decades, several surprising examples have been reported such as auxetic materials [4–6], materials with vanishing shear modulus [7, 8], materials with negative compressibility [9, 10], singularly nonlinear materials [11, 12], origami(-inspired) metamaterials [13–16], topological metamaterials [17–19], and multistable and programmable mechanical metamaterials [20] etc.

To a starter, the world of mechanical metamaterials can be best introduced by the help of examples that demonstrate which exotic properties and functionalities have been thus far realized. Below, we broadly categorize these featured properties and briefly mention some famous corresponding examples.

Extremal materials – Milton and Cherkaev theoretically proposed extremal materials in 1995 and defined them as materials that are extremely

stiff in certain modes of deformation, while extremely compliant in the other modes [21]. Kadic et al. demonstrated that the theoretically possible pentamode metamaterials, which have extremely large bulk modulus compared to the shear modulus, can be realized experimentally by periodic placement of a specially designed artificial crystal, thereby pushing the boundaries for materials with exceptional response parameters [Fig. 1.1(a)] [7]. The solid lattice structure shears or deforms easily. At the same time the lattice is extremely hard to compress. These pentamode materials are therefore sometimes also called *metafluids*. Based on the pentamode metamaterials, Buckmann et al. later showed an experimental demonstration of a mechanical cloak [Fig. 1.1(b)] [8].

Another class of extremal materials are dilational materials, where the bulk modulus is extremely low and the shear modulus is extremely high. Several examples of dilational metamaterials can be found in the literature [22–25]. For these materials the Poisson's ratio, ν takes on the value -1. Any material with a negative value of ν is called an *auxetic* material. An archetypal example would be a quasi-2D elastic slab pierced with circular holes on a square array [26, 27]. Upon compression, the elastic slab undergoes buckling at the connector ligaments and attains a state of mutually orthogonal ellipses [Fig. 1.1(c)]. This pattern transformation allows the sample to exhibit a negative value of the Poisson's ratio.

Shape Morphing and Multistability – Tunability in the response properties is a common theme in the area of metamaterial research, which includes optical and electromagnetic counterparts as well [28–31]. The reconfigurable design of mechanical metamaterials is aimed to do just that by allowing for multiple switchable states, which usually occur by the reconfiguration of the lattice or unit cell geometry. The most striking examples are rigid folding based origami metamaterials, in which the faces between the creases remain rigid during folding/unfolding and only the creases bend [32]. The most studied one is the Miura-ori and its derivative crease patterns [13, 14, 33]. Waitukaitis et al. demonstrated that the simplest building blocks of origami, the degree-4 vertices, can be multistable with upto six possible stable states. Further, these 4-vertices can be tiled periodically into large tessellations allowing to create multistable *metasheets* that can be externally actuated to morph from one state to another [Fig. 1.1(d)] [34]. Departing away from strict rigid folding, Pinson et al. presented

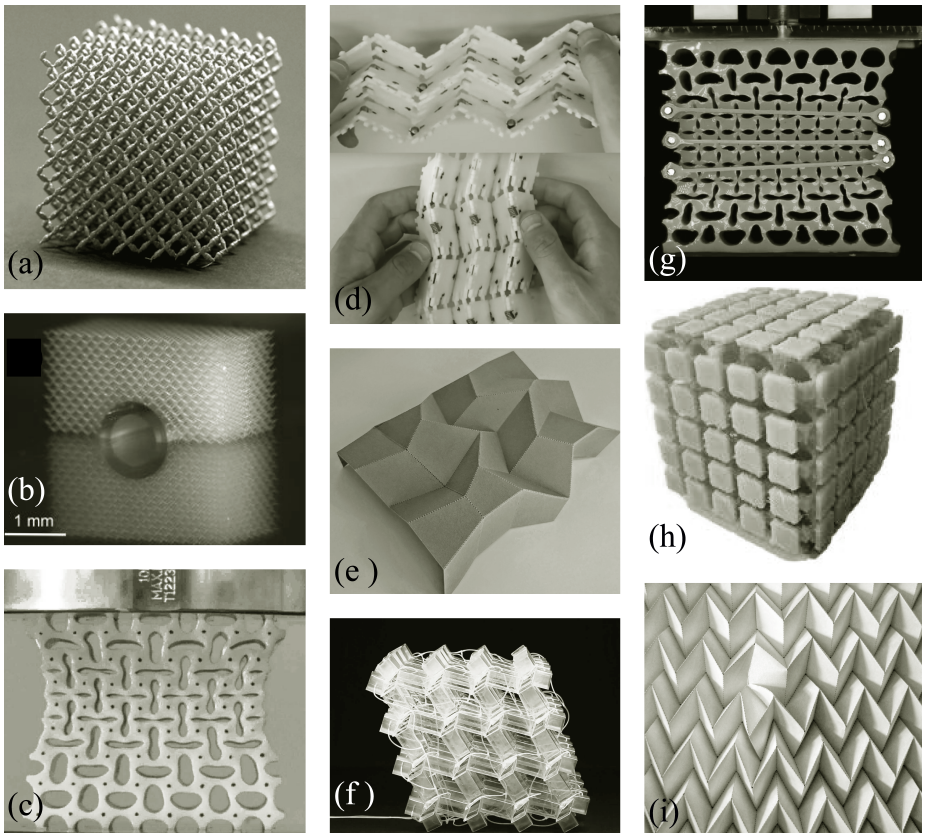

Figure 1.1: A gallery of some of the famous examples of mechanical metamaterials that demonstrate key concepts such as exceptional material response, shape morphability and programmability in the mechanical response. (a) pentamode metamaterials that are easy to shear but hard to compress [7], (b) a mechanical cloak based on pentamode metamaterials [8], (c) an auxetic material with a negative value of the Poisson's ratio [26], (d) rigid folding based multistable origami *metasheets* [34], (e) computer-designed novel foldable origami patterns that do not feature strict rigid folding [35], (f) an origami-inspired shape-transformable mechanical metamaterial [16], (g) a programmable mechanical metamaterial that exhibits programmability in the mechanical response [20], (h) a 3D mechanical metamaterial whose inner comprising unit cells can be stacked combinatorially to achieve diverse shape-shifting behavior [37], (i) a miura-ori origami pattern with local pop-through defects that control the compressive modulus of the overall structure [13]. Images are adopted from the respective cited sources.

a systematical approach to sample arbitrary origami crease patterns based on their folding energy and reported numerous near-perfect origami mechanisms, which can be deployed in situations where accidental self-folding needs to be avoided [Fig. 1.1(e)] [35]. Shape morphing and multistability are widespread in other categories of mechanical metamaterials as well. Rafsanjani et al. reported a class of switchable networks consisting of rigid rotating units connected with complaint hinges that simultaneously exhibit auxeticity and structural bistability [36].

Programmability – The essence of mechanical metamaterials is to let the structural design determine the mechanical response. Florijn et al. showed that if in the sample shown in Fig. 1.1(c), the alternate holes are made unequal in size [Fig. 1.1(g)], the sample retains the buckling induced auxeticity, albeit the buckled state is now dependent along which primary axis the sample is compressed. The precise tuning of these two decoupled deformations allowed to achieve programmability in the mechanical response [20]. Moving ahead from planar elastic metamaterials towards 3D shapes, Coulais et al. reported a class of aperiodic yet frustration-free architectures designed combinatorially using special cubic unit cells - *voxels* - such that their collective deformations can result in a shape morphing behavior, which can be preprogrammed due to multiple combinatorial possibilities in the arrangement of these voxels [Fig. 1.1(h)] [37]. Silverberg et al. demonstrated programmability in the mechanical response of the Miura-ori origami tessellation. There it was show that the mechanically bi-stable internal unit cells can be 'switched on' to act as local defects analogous to a crystal lattice and thus helping in tune the compressive modulus of the sheet [Fig. 1.1(i)] [13].

The examples of mechanical metamaterials cited above mainly deform by exploiting frustration-free low energy deformation pathways in the structure [37]. Very often its is possible to imitate the desired deformation mode by the free motion mode of an idealized mechanism consisting of hinging/rotating rigid geometrical parts [18, 38–41]. As a matter of fact, these mechanisms serve as an intuitive starting point to initiate and adapt the design to the requirements [20, 42]. Soft mechanical metamaterials can then be fabricated by joining stiffer elements with flexible, slender hinges allowing to achieve large deformations. Intuition based strategies to design mechanical metamaterials bottom-up from their base mechanisms can lead to a couple

of general limitations: *(i)* the designs can be generic and periodic, *(ii)* materials exhibiting simpler functionalities are simple to discover and vice-versa. These limitations can be mitigated by adopting inverse methods for material design, which we discuss in the details below.

1.2 Inverse Strategies for Material Design

Across wide areas, inverse strategies are emerging as a promising approach in the realm of rationally designing the materials with desired properties [43–51]. The central idea is to come up with a framework which takes functional requirements as input and delivers the macroscopic design of the structure that satisfies them as output. Following such a strategy possesses several advantages over traditional engineering methods for material design. In the absence of some physical theory that connects the response function of the material with its structural design, the usual method to optimize the former is via tweaking the later, followed by synthesizing and testing. This approach is severely limited as only the simpler tasks can be easily handled. For complex tasks, one usually is content with very suboptimal designs, and not to mention that the traditional methods can be very time consuming.

Significant improvements in the computational capabilities and state-of-the-art fabrication techniques such as 3D printing (to fabricate complex designs intricately) in recent times have led to new advancements towards more logical inverse methods, which have been in practice since much earlier [52, 53]. These methods allow to handle complex design tasks and the whole process can be fully automated too, allowing to design materials on demand with varying target properties [54]. Another major benefit of deploying such techniques is that they typically result in the discovery of many near-perfect designs that fit the target criteria *quite closely*, thus significantly enlarging the design space and enabling its systematic explorations, which further aids in gaining a better understanding of the design space [35].

One way to carry out the design is by following an optimization-based methodology. In here, the main task of finding the optimal material design is formulated as an optimization problem, to do which, one has to first identify the shape parameters of the design that control the target response - *design variables*. The next step is to construct a physical or numerical model that simulates the material functioning on a computer, and is able to estimate the quality of any valid arbitrary design. The formal terminology

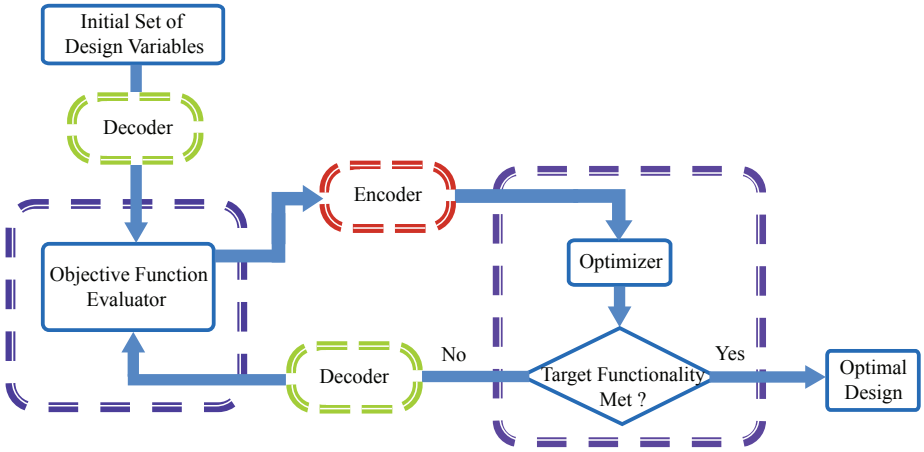

Figure 1.2: An optimization-based automated material design framework, that renders optimal design to match a given target property. Starting from an initial set of design variables, the optimizer searches for the optimal values of the design variables such that the objective function, which is a function of design variables, is maximized or minimized. Depending upon the implementation of the optimization algorithm, often the interfacing between the optimizer and the objective function evaluator consists of an intermediate encoding-decoding step that involves the mapping between coding space and the design space [55].

for this is *objective function* value which in effect is controlled by the values of design variables. The objective function measures the quality or *fitness* of a candidate design (solution). For example, if a minimization problem is formulated, low objective function values would correspond to better quality of design. With this framework, one is now set to optimize the design variables for the desired target behavior.

Complexity of a design optimization problem is dependent upon the dimensionality, which in turn is given by the total number of design variables. Higher dimensionality implies a very likely complex objective function landscape consisting of several local minima. This leads to an ineffectiveness of using gradient-based methods [56]. A far more promising choice in such cases is to use nature-inspired search heuristics that use a population-based method to efficiently explore the search space; think of genetic algorithms, evolutionary strategies, swarm intelligence algorithms, genetic programming

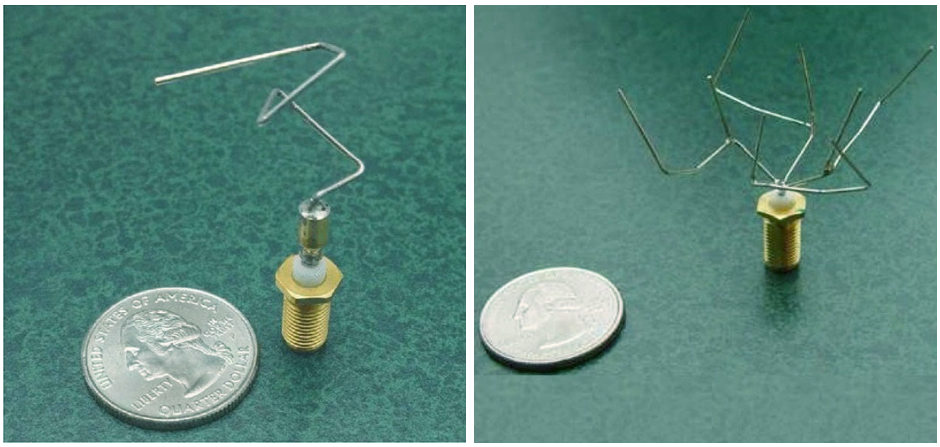

(a) **(b)**

Figure 1.3: Prototype photographs of evolved antenna designed by NASA for their Space Technology 5 (ST5) mission with set specific requirements for two desired radiation patterns: antenna's named (a) ST5-33-142-7 and (b) ST5-3-10 [63]. Images are adopted from the main source.

etc. [57–62]. The purpose of these algorithms is to optimize the values of design variables such that the target criteria is met. An objective function evaluator and an optimizer can together interface to form an automated design framework that takes a target material functionality as input and renders the optimal structural design as output. The process is schematically shown in Fig. 1.2.

In past, the employment of evolutionary (and related) search algorithms for design optimization purposes has delivered promising results across diverse fields such as in aerodynamics [53], structural engineering [64], design of mechanical components [51, 65], robotics [66, 67], Lithium-ion battery design [68], crystal structure prediction [47] and many more. We show in Fig. 1.3, *evolved antenna* designs reported by NASA in 2006, where evolutionary algorithms were utilized to discover sophisticated designs for prescribed radiation patterns of the antenna [63].

In this thesis, we present novel inverse strategies to design 2D mechanical metamaterials, whose internal deformations can be captured by underlying idealized mechanisms consisting of hinging rigid parts. We show that by optimizing for the characteristic trajectory of these single degree-of-freedom

mechanisms, one can design generic metamaterials that exhibit complex mechanics, atypical zero-energy deformations and shape-transformable behavior.

1.3 Outline of the Thesis

The second chapter of this thesis serves as a inspiration as to what level of insights can be obtained by modeling the deformation of a mechanical metamaterial by its base mechanism. Specifically, we discuss in details a physical approach to analytically model the experimentally observed different mechanical regimes of a laterally confined *biholar* mechanical metamaterial reported in [20]. We show that non only a simple one-degree-of-freedom mechanism - *soft mechanism* - consisting of pin-jointed rectangles qualitatively captures the mechanical trends, but - and as the most relevant result of the chapter - also, conversely provides with an inverse strategy to design mechanical metamaterials for many more complex confinement-controlled mechanical responses. We suggest that based on the trajectory of a mechanism, various complex bifurcation sequences can be encoded, which unfold as the control parameter (amount of horizontal confinement here) is varied. We then show that coupling the hinges of the soft mechanism with torsional springs models the ligament thickness well. Finally, we utilize the soft mechanism to probe the limiting case, where the neighboring holes of the biholar sheet approach to be of equal size, and mathematically show that these regimes emerge from the unfolding of an imperfect pitchfork bifurcation.

In the third chapter of this thesis, we demonstrate a nature-inspired search strategy to design the optimal geometry of 2D unit cells that are not periodic but can still allow for atypical (approximate) zero-energy modes. We pursue it by the design of its underling mechanism. We begin with a single degree-of-freedom *precursor mechanism* consisting of pin-jointed polygons, whose internal motion can be captured by a characteristic curve. We then optimize the geometrical design of the mechanism such that the curve encoding the internal motion matches a prescribed target curve. We show that via this strategy, our search algorithm is able to discover plethora of *pseudo-mechanisms* with a very soft deformation mode that are far away from a true mechanism with a strict zero-energy mode. Further, we investigate the functioning of our algorithm and characterize it to gain

insights into its search quality, solution distribution and exploration behavior of the search space. We then demonstrate a simple but elegant method to tile these unit cells into regular tessellations - *metatilings*, while still preserving the original soft more. Finally, we bring these unit cells and metatilings to life via 3D printing and confirm the expected deformation modes experimentally.

In the fourth chapter of this thesis, we demonstrate a crucial capability of an automated material design framework, which is the ability to optimize the structural shape for not just one but for multiple target properties. We input different target curves into our model in order to: *(i)* quantify the functioning of our model versus the complexity of the design task (target curves), and *(ii)* design and fabricate 2D bi-stable and tri-stable unit cells consisting of rigid units connected together through flexible slender linkages. Finally, we show that by carefully harnessing the elastic-frustration, one can tessellate copies of these unit cells and obtain larger shape-transforming mechanical metamaterials.

Chapter 2

The Soft Mechanism

Abstract – In this chapter, we show that the experimentally observed different mechanical regimes in a laterally (x-) confined *holey* elastic mechanical metamaterial [20] can qualitative be captured by a spring-coupled mechanism consisting of rotating rigid rectangles - *soft mechanism* - and discuss the physical method to do so in details. The soft mechanism allows us to understand these regimes from a geometrical perspective, extending which, we suggest a general design strategy for confinement-programmable response of mechanical metamaterials. Mainly, we propose that based on the trajectory of the mechanism, it is theoretically possible to encode plenty of other sequence of equilibria that unfold as the control parameter (x-confinement in our case) is varied. We model the inter-hole ligament in the real samples by coupling the hinges of soft mechanism with torsional springs and observe some qualitative agreements with [70] in terms of the critical values of x-confinement that separate the four successive regimes. We finally, consider the limiting case where the neighboring holes in the sample approach to be of equal size and mathematically show that these regimes result from the unfolding of an imperfect pitchfork bifurcation.

2.1 Introduction

We begin with presenting a brief review of the work reported in [20]. The reader is encouraged to refer to the main source for a more detailed understanding.

Programmable mechanical metamaterials – It has been observed both experimentally and numerically that the mechanical response of a quasi-2D elastic slab perforated with an alternating pattern of large and small equi-sized circular holes in such a manner that the center of the holes lie on a square array, called a *biholar sheet*, can be controlled by the amount of a prior external *horizontal confinement* (strain, also called x-confinement), ϵ_x by means of fixed size plastic clamps. Fig. 2.1(a) shows a biholar sheet, whose geometry is set by the parameters D_1, D_2 and p, where D_1, D_2 are the respective hole diameters of the smaller and larger holes and p is the hole-separating *pitch*. We use here also the dimensionless quantities defined in the original work - *biholarity*, χ,

$$\chi = (D_2 - D_1)/p, \tag{2.1}$$

and minimum *thickness of the interhole ligaments*, t_l,

$$t_l = 1 - (D_1 + D_2)/2p. \tag{2.2}$$

Fig. 2.1(b) shows a biholar sheet that is horizontally confined by using the plastic clamps. The force response (P) to vertical compression (ϵ_y) can be changed from monotonic to non-monotonic to hysteretic and lastly back to monotonic again all for the same biholar sheet, when the x-confinement is increased. Fig. 2.2(a-d) shows, experimentally realized, the four different force-deformation responses of a biholar sheet ($\chi = 0.30$, $t_l = 0.15$) for different values of ϵ_x [69]. Inside each figure, the insets show the biholar sample in its initial x-confined state i.e. $\epsilon_y = 0.0$.

Brief explanation – Upon compression, an *unconfined* biholar sheet undergoes a smooth pattern transformation to attain a state containing alternate mutually orthogonal ellipses. Depending upon the direction of compression, such a pattern of mutually orthogonal ellipses can exist in the following two arrangements: *(i)* the major axes of the larger ellipses are

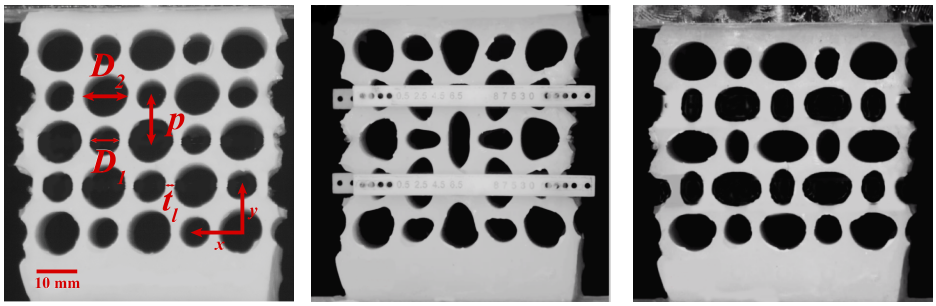

(a) **(b)** **(c)**

Figure 2.1: (a) Biholar sheet: an elastic slab perforated with an alternating pattern of large and small circular holes on a square array, characterized by the respective hole diameters D_1, D_2 of smaller and larger holes, the hole-separating *pitch* - p , and the minimum ligament thickness, t_l. Compressing the biholar sheet results in the formation of mutually orthogonal ellipses, which however, depending upon the direction of compression, can exist in two different arrangements. A biholar sheet in two differently polarized states: (b) *x-polarized* state - the sample is compressed along x-direction as a result of which the larger ellipses have their major axis oriented along the y-axis, and (c) *y-polarized* state - the sample is compressed along the y-direction, which leads to the larger ellipses orient their major axis parallel to the x-direction. These images are adopted from [69].

oriented parallel to the y-direction. This happens when the biholar sheet is compressed along the x-direction, and likewise *(ii)* the major axes of the larger ellipses are oriented along to the x-direction. This happens when the biholar sheet is compressed along the y-direction. The difference in the hole sizes breaks the 90° rotational symmetry that is present when the holes are of equal size. This causes a difference in the polarization of the hole pattern, depending along which direction the sample is compressed. In the original work, these two differently *polarized* states are referred to as *x-polarized* and *y-polarized* states respectively and are shown in Fig. 2.1(b,c).

It can be imagined that the application of an initial x-confinement followed by a subsequent vertical compression can lead to a pattern switch from a x-polarized state to a y-polarized state. Depending upon the magnitude of the x-confinement, such a pattern switch can be both smooth or discontinuous. As a result of the symmetry breaking, the deformations along

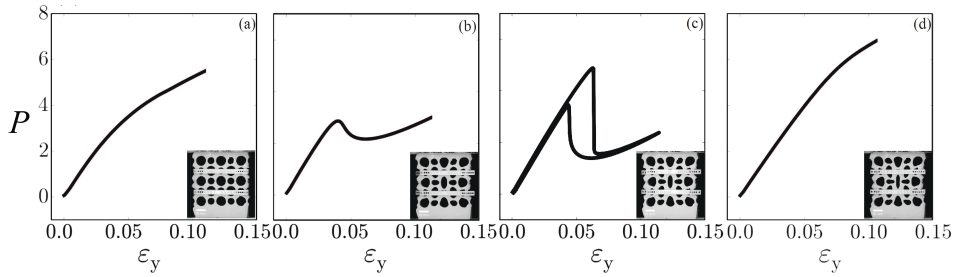

Figure 2.2: Experimentally observed mechanical response of a x-confined 5x5 biholar sheet with geometrical parameters $D_1 = 7$ mm, $D_2 = 10$ mm, $t_l = 0.15$. ϵ_x denotes the x-confinement. (a) $\epsilon_x = 0.0$, $P(\epsilon_y)$ is monotonic. (b) $\epsilon_x = 0.12$, $P(\epsilon_y)$ is non-monotonic. (c) $\epsilon_x = 0.15$, $P(\epsilon_y)$ is hysteretic. (d) $\epsilon_x = 0.18$, $P(\epsilon_y)$ is monotonic. The insets within the figures show the initial state of the confined biholar sheet i.e. at $\epsilon_y = 0.0$. The figures are adopted from [69].

the two primary axes interact nonlinearly. Indeed, this nonlinear coupling between the x- and the y-polarized states set up by the interacting forces of horizontal confinement and vertical compression results in the nontrivial mechanics of a confined biholar sheet [Fig. 2.2].

In this chapter, we first show that the experimentally realized mechanics of a confined biholar sheet can qualitatively be captured by a spring coupled one-degree-of-freedom mechanism consisting of pin-jointed rectangles. We call this the *soft mechanism*. We discuss in details the physical method to model the experiments in §2.2. We employ the mechanism to understand the different mechanical regimes from a geometrical perspective and based on which, we layout a general design strategy in §2.3, following which, plenty of other sequences of equilibria can be constructed leading to diverse confinement controlled responses. We take into account the thickness of the hole-connector ligaments by coupling the hinges of the mechanism with torsional springs in §2.4. Finally in §2.5, we explore the mechanism for the limiting case where the neighboring holes become 'almost' equi-sized, $\chi \to 0$, and mathematically show that the different regimes emerge from the unfolding of a pitchfork bifurcation.

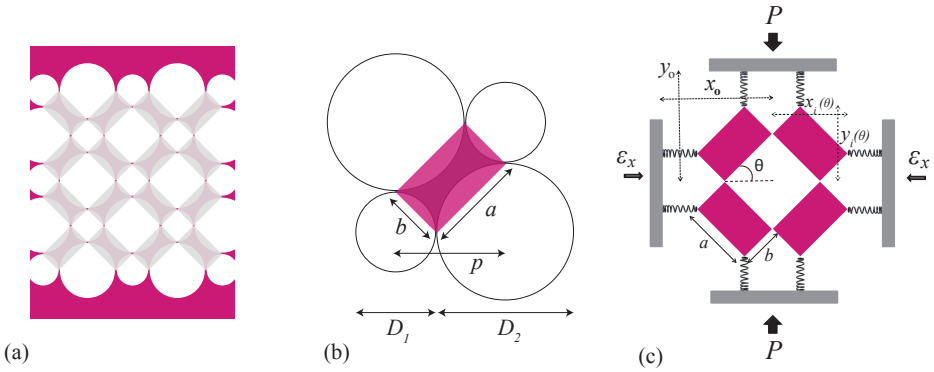

Figure 2.3: Soft mechanism - a mechanical model that is aimed to qualitatively captures the mechanical response of an x-confined biholar sheet [Fig. 2.2]. (a) In a biholar sheet with thin interhole ligaments, the deformations primarily occur via the bending of the ligaments and can be approximated by a mechanism consisting of pin-jointed, rigid rectangles. (b) The mapping between the rectangular rigid unit of the mechanism and the elastic unit of a biholar sheet. (c) Soft mechanism - spring coupled representative unit of the full mechanism shown in (a). The enclosing walls model the lateral confinement (ϵ_x) and vertical strain (ϵ_y).

2.2 Soft Mechanism Model

In this section, we derive a simple geometry-based model that captures important aspects of the mechanics of a confined biholar sheet, based on [20].

Soft mechanism – The deformations in a biholar sheet with vanishingly small thickness of the interhole ligaments (denoted by t_l in Fig. 2.1(a)) occur primarily via the bending of these ligaments. In such a case, the deformation of the elastic units is minimal, and thus the process can be modeled via an equivalent one-degree-of-freedom mechanism consisting of pin-jointed rigid rectangles [Fig. 2.3(a)]. The mapping of these rectangular units of length a and width b onto the elastic units is shown in Fig. 2.3(b). One unit cell of such a mechanism is sufficient for our purpose [Fig. 2.3(c)], which we use to capture the mechanical response. To incorporate the storage of the elastic energy into the system, the free corners of the rectangular units are coupled to the enclosing walls both horizontally and vertically

by a set of four linear springs. The enclosing horizontal and vertical walls model the lateral confinement (ϵ_x) and the vertical strain (ϵ_y), respectively.

Biholarity – With the mapping shown in Fig. 2.3(b), we express the dimensionless biholarity [Eq. (2.1)] in terms of a and b. We note that $D_1 = b\sqrt{2}$, $D_2 = a\sqrt{2}$ and $p = (a+b)/\sqrt{2}$. Substituting these values in Eq. (2.1) gives:

$$\chi = 2\frac{(a-b)}{(a+b)}. \tag{2.3}$$

In the remainder of the work, we choose our lengths so that $a + b = \sqrt{2}$. Therefore,

$$\chi = \sqrt{2}(a-b). \tag{2.4}$$

For simplicity, considering $a \geq b$ (a and b are interchangeable), the allowed range of biholarity is $\chi \in [0, 2]$.

2.2.1 Load-Deformation Response

We mathematically model the displacement controlled loading of a biholar sheet by following a quasi-static deformation approach for the soft mechanism. We begin with the total internal energy stored inside the soft mechanism, U, under the influences of the external x-confinement, ϵ_x, and the vertical load, P. The total internal energy U is given by

$$U = E_x + E_y, \tag{2.5}$$

where E_x and E_y are the total elastic energies stored in the horizontal and vertical springs respectively. A quasi-static approach implies that at any given instant, the system is in equilibrium. Hence, E_y in the above equation can be replaced by the work done on the system by the acting load P. We denote it with W. Therefore, Eq. (2.5) becomes

$$U = E_x + W. \tag{2.6}$$

We know that since the soft mechanism contains only one internal degree-of-freedom, its state can completely be parameterized in terms of one variable. We use θ for this purpose [Fig. 2.3(c)]. In effect, $\theta = \pi/4$ represents the neutral state of the biholar sheet, whereas, $\theta > \pi/4$ and $\theta < \pi/4$ represent the x-polarized and y-polarized states respectively [Fig.

2.1(b,c)]. In terms of θ, we define two more quantities: $x_i(\theta)$ and $y_i(\theta)$, which denote the maximum x and y dimensions of the rectangular unit of the mechanism. With the length a and the width b of the rectangular unit, $x_i(\theta)$ and $y_i(\theta)$ can be expressed as:

$$x_i(\theta) = a\cos\theta + b\sin\theta, \tag{2.7}$$

and,

$$y_i(\theta) = a\sin\theta + b\cos\theta. \tag{2.8}$$

Let us suppose that upon the application of some initial x-confinement, ϵ_x, the soft mechanism changes from its *neutral state* at $\theta = \pi/4$ to some other state given by θ. E_x at this perturbed state can be expressed as

$$\begin{aligned} E_x &= 4 \times \frac{1}{2} k_x \left(\epsilon_x + x_i(\theta) - x_i\left(\frac{\pi}{4}\right)\right)^2, \\ &= 2k_x \left(\epsilon_x + x_i(\theta) - x_i\left(\frac{\pi}{4}\right)\right)^2, \\ &= 2k_x \left(\epsilon_x + x_i(\theta) - 1\right)^2, \quad \text{(because } x_i(\pi/4) = 1\text{)}, \end{aligned} \tag{2.9}$$

where k_x is the spring constant of the horizontal springs. The term inside the parentheses of the above equation denotes the net compression or extension of the horizontal springs [1]. ϵ_x is positive for compression and negative for extension.

The total work done on the system, W can be written as

$$\begin{aligned} W &= 2P\left(y_i(\theta) - y_i\left(\frac{\pi}{4}\right)\right), \\ &= 2P(y_i(\theta) - 1), \quad \text{(because } y_i(\pi/4) = 1\text{)}. \end{aligned} \tag{2.10}$$

Substituting the values of E_x and W respectively from the Eq. (2.9) and Eq. (2.10) into Eq. (2.6) (along with utilizing the expressions for $x_i(\theta)$ and $y_i(\theta)$ from Eq. (2.7) and Eq. (2.8)), an expression of U in terms of θ can be obtained. Since the equilibrium state of the mechanism is changed to

[1] Let us assume that L denotes the rest length of the horizontal springs [Fig. 2.3(c)]. Then, $L + x_i(\pi/4) = x_o$. If the application of the horizontal strain ϵ_x changes the length of the spring to L', one can then write $\epsilon_x + L' + x_i(\theta) = x_o$. ϵ_x is positive for compression and negative for extension. Therefore, change in the length of the springs $|L - L'| = \epsilon_x + x_i(\theta) - x_i(\pi/4) = \epsilon_x + x_i(\theta) - 1$.

another adjacent equilibrium state in response to the change in the vertical load P, then in order to maintain that, the condition of $\partial U/\partial\theta = 0$ must be met. Setting up this condition leads to an equation relating P with the other variables:

$$P = -2k_x\left(\epsilon_x + x_i(\theta) - 1\right)\left(\frac{-a\sin\theta + b\cos\theta}{a\cos\theta - b\sin\theta}\right). \tag{2.11}$$

The vertical strain ϵ_y can be expressed as

$$\epsilon_y = (1 - y_i(\theta)) + \frac{P}{2k_y}, \tag{2.12}$$

where k_y is the spring constant of the vertical springs. In Eq. (2.12), $(1 - y_i(\theta))$ is the vertical deformation in the mechanism apart from the compression in the springs and $P/2k_y$ is the compression in the springs (because the load is always quasi-statically balanced by the spring force).

For fixed a, b and ϵ_x, Eq. (2.11) and Eq. (2.12) together with Eq. (2.7) and Eq. (2.8) establish explicit functions of θ to P and ϵ_y, and hence provide an implicit relationship between the load, P and the vertical strain, ϵ_y. Given the values of a, b (i.e. the biholarity χ, Eq. 2.4) and ϵ_x, and the values of the spring constants, k_x and k_y, one can implicitly obtain the load-deformation curve, $P(\epsilon_y)$. Numerically, this is done by varying the value of θ from 0 to $\pi/2$ and separately calculating the values of P and ϵ_y from Eq. (2.11) and Eq. (2.12) respectively, thereby obtaining a discretized version of the $P(\epsilon_y)$ curve.

Load-deformation curves – We now utilize the derived Eq. (2.11) and Eq. (2.12) and show $P(\epsilon_y)$ for a system with $\chi = 0.30$ ($a \approx 0.81$ and $b \approx 0.60$) [2]. We use the same value for the two spring constants : k_x, $k_y = 0.50$. For four different values of ϵ_x, $P(\epsilon_y)$ is shown in the Fig. 2.4(a-d). Each figure displays a different qualitative trend, which we refer to as regimes ***(i-iv)*** [3]. Below we discuss them separately :

[2] Unless otherwise mentioned, we keep the value of χ fixed to 0.30 in the rest of the chapter as well.

[3] For now only the *primary branches* (shown in black) in Fig. 2.4 are relevant. In §2.3.1, we describe the emergence of the secondary red branches in detail. By the primary branch we mean the solution branch which connects to the unique solution branch that exists for $\epsilon_y << 0$.

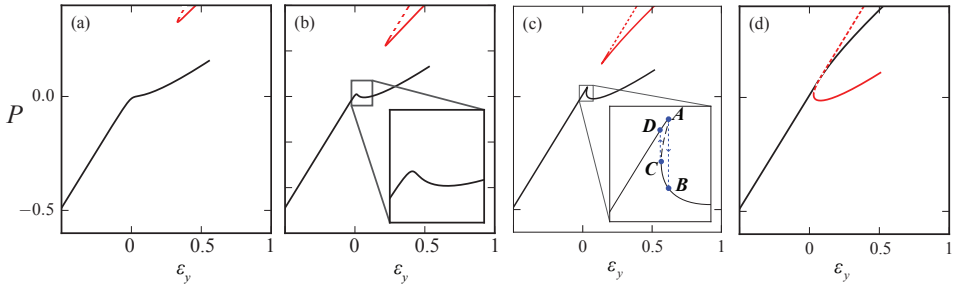

Figure 2.4: $P(\epsilon_y)$ for a system with $\chi = 0.30$ ($a \approx 0.81$ and $b \approx 0.60$). Within each figure, the primary branch (of current relevance) is shown in black and the secondary branch is shown in red (discussed in §2.3.1), and on these branches, the stable and the unstable equilibria are shown in the solid and the dashed curves respectively. **(a)** ϵ_x = -0.015, $P(\epsilon_y)$ increases monotonically. **(b)** $\epsilon_x = 0.010$, $P(\epsilon_y)$ is non-monotonic. **(c)** $\epsilon_x = 0.028$, $P(\epsilon_y)$ exhibits hysteresis. Hysteretic jumps are shown in the dashed blue lines in the inset with $\boldsymbol{A - B}$ and $\boldsymbol{C - D}$ jumps corresponding to the loading and the unloading deformation paths respectively. We discuss this more clearly in the text. **(d)** $\epsilon_x = 0.040$, $P(\epsilon_y)$ becomes monotonic again. With these four regimes, the soft-mechanism successfully models the experimentally observed mechanical response [Fig. 2.2]. Unlabeled axis ticks and tick labels are shared.

Regime *(i)*: For ϵ_x= -0.015 [Fig. 2.4(a)], the $P(\epsilon_y)$ curve increases monotonically with ϵ_y. However, the slope of the curve varies. The initial value of slope = 0.50, which is equal to k_y. This is true for all the four regimes ***(i)-(iv)***. The slope of the curve then decreases, and finally increases again. The mechanism behaves as a nonlinear elastic material in this regime.

Regime *(ii)*: For $\epsilon_x = 0.010$ [Fig. 2.4(b)], the $P(\epsilon_y)$ curve becomes non-monotonic; displaying a *dip*. As we will show in §2.3.1, the dip in the $P(\epsilon_y)$ curve results from a polarization change [4]. Positive value of ϵ_x makes the mechanism x-polarized [Fig. 2.2(b) inset]. The polarization changes to y-polarized state under the influence of P.

[4]Here, and while discussing the regimes ***(iii)***, ***(iv)*** in the following discussion, we very briefly mention the related polarization states and switches. We discuss them in details in §2.3.1.

Regime *(iii)*: For $\epsilon_x = 0.028$ [Fig. 2.4(c)], the $P(\epsilon_y)$ curve is clearly non-monotonic but different from the one in Fig. 2.4(b). The formation of a cusp and multi-valuedness of $P(\epsilon_y)$ signals hysteresis with characteristic hysteretic jumps (see inset). During loading the mechanism follows the path that includes a *jump* from $\boldsymbol{A-B}$, while during unloading the mechanism follows another path that includes a jump from $\boldsymbol{C-D}$. This also makes the path $\boldsymbol{A-C}$ unstable and thus is shown as a dashed curve. From a polarization point of view, these jumps result from a *sudden* polarization switch: x to y polarization switch during $\boldsymbol{A-B}$ jump and y to x polarization switch during $\boldsymbol{C-D}$ jump. Quick jumps from one polarization state to another at a fixed ϵ_x, ϵ_y demonstrates bistability. In the experiments these jumps are associated with *snap-through buckling* [71].

Regime *(iv)*: For $\epsilon_x = 0.040$ [Fig. 2.4(d)], the $P(\epsilon_y)$ curve becomes monotonic again. This is however not the same as in regime ***(i)***, but is indeed exactly opposite from a polarization perspective - the previously secondary branch is now primary and vice-versa. High values of ϵ_x makes the sample *strongly* x-polarized (see biholar sample in Fig. 2.2(d), inset) which gets further accentuated with the application of the load.

A qualitative match with the experimental and finite element simulation results shown in the original work confirms the robustness of the soft mechanism to model the mechanical response of a laterally confined biholar sheet. We point out that the above discussed regimes ***(i)-(iv)*** exist for a range of ϵ_x. The switch from one regime to another (which may or may not involve a bifurcation [5]), however, occurs at fixed critical values of ϵ_x. If given that k_x and k_y have the same values, both the range and the critical values of ϵ_x demarcating the four regimes depends on the value of χ. We derive the general analytical expressions for these critical strain values in the next section.

2.2.2 Internal Energy of the System

We will now have a closer look at the energy curves. Using Eq. (2.5), the total elastic energy, U is equal to $E_x + E_y$. The expression for E_x is given

[5] This depends on whether there are some equilibrium points whose stability has been altered or not.

by Eq. (2.9), and below the expression for E_y is provided:

$$E_y = 2 \times 2 \times \frac{1}{2} \times k_y \left(\frac{P}{2k_y} \right)^2 , \\ = \frac{P^2}{2k_y}. \tag{2.13}$$

Therefore,

$$U = 2k_x \left(\epsilon_x + x_i(\theta) - 1 \right)^2 + \frac{P^2}{2k_y}. \tag{2.14}$$

Energy curves – Utilizing Eq. (2.14) and Eq. (2.12), one can numerically obtain the $U(\epsilon_y)$ curves for a system with given χ and ϵ_x. We now discuss $U(\epsilon_y)$ for the same system and the same four values of ϵ_x as in Fig. 2.4(a-d). The results are shown in Fig. 2.5(a-d). Within each figure, we show the primary branch (black) in the main panel and both the primary and secondary (red) branches in the inset panel. We focus on the primary branches to characterize the regimes:

Regime *(i)*: For ϵ_x= -0.015 [Fig. 2.5(a)], the $U(\epsilon_y)$ curve has one global minimum ($U = 0.0$), which occurs for the value of ϵ_y when $P = 0$ because $P = \Delta U/\Delta\epsilon_y$. As we can clearly notice from the inset that the primary and the secondary branches are well-separated, making the later 'infeasible'.

Regime *(ii)*: For ϵ_x= 0.010 [Fig. 2.5(b)], the $U(\epsilon_y)$ curve consists of two global minima separated by a shallow maximum - $P(\epsilon_y)$ is non-monotonic

Regime *(iii)*: For ϵ_x= 0.028 [Fig. 2.5(c)], the $U(\epsilon_y)$ provides another perspective to the hysteresis and the associated bistability. The labeled points $\boldsymbol{A, B, C}$ and $\boldsymbol{D}$ in the inset correspond to the same points previously shown in Fig. 2.4(c). The paths $\boldsymbol{DAB}$ and $\boldsymbol{BCD}$ correspond to the loading and unloading respectively. Hysteretic jumps occur from $\boldsymbol{A - B}$ during loading and from $\boldsymbol{C - D}$ during unloading. The path $\boldsymbol{A - C}$ is unstable and is therefore shown in a dashed curve.

Regime *(iv)*: For ϵ_x= 0.040 [Fig. 2.5(d)], the $U(\epsilon_y)$ once again has only one global minimum - $P(\epsilon_y)$ is monotonic. In the inset, we notice that

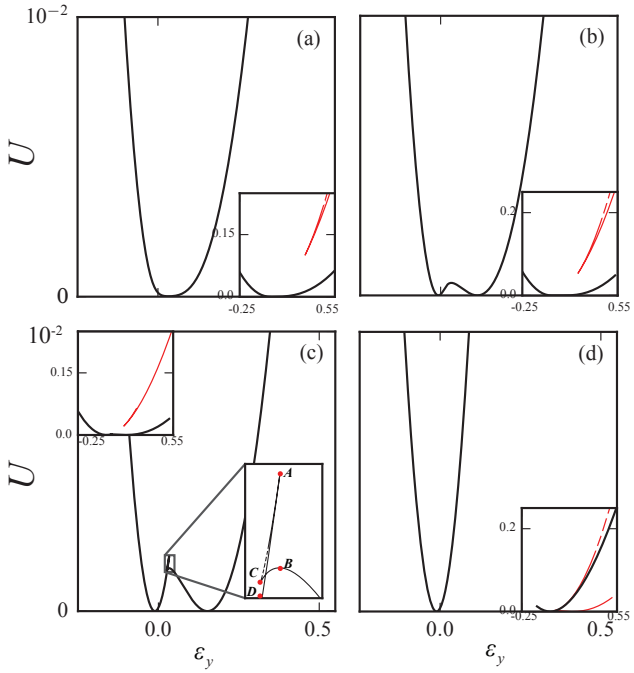

Figure 2.5: $U(\epsilon_y)$ for a system with $\chi = 0.30$ ($a \approx 0.81$ and $b \approx 0.60$), and for the same four values of ϵ_x as shown in Fig. 2.4(a-d). Within each figure, the primary branch (of current relevance) is shown in black (main panel) and the secondary branch is shown in red (inset panel), and the stable and the unstable equilibria are shown in the solid and dashed curves respectively. (a) ϵ_x = -0.015, $U(\epsilon_y)$ consists of only one global minimum. (b) $\epsilon_x = 0.010$, $U(\epsilon_y)$ consists of two local minima separated by a local maximum. (c) $\epsilon_x = 0.028$, $U(\epsilon_y)$ exhibits hysteresis. The labeled points $\boldsymbol{A, B, C, D}$ are the same as in Fig. 2.4(c). (d) $\epsilon_x = 0.040$, $U(\epsilon_y)$ consists of a global minimum. Because, $P = \Delta U/\Delta\epsilon_y$, $P(\epsilon_y)$, we can verify that the figures (a)-(d) correspond to the regimes ***(i)-(iv)***.

the primary and the secondary branches intersect. The system however does not switch from one state branch to another. As we will show in the next section: two values of θ can exist for a single value of ϵ_y for this case. So, although, when extracted numerically, the primary and the secondary branches intersect on a $U(\epsilon_y)$ graph, they are separated in the $\theta(\epsilon_y)$ graph; and the system only follows the primary branch of θ.

2.3 Geometrical Interpretation

For fixed biholarity χ, we have essentially two control parameters: the horizontal confinement, ϵ_x and the vertical strain, ϵ_y. The values of these control parameters dictate the number of possible equilibria and their stability. In this section, we introduce a geometrical interpretation of the model, through which we gain new insights about equilibria and their stability. Based on such an interpretation, we ultimately demonstrate a novel geometrical interpretation of the previously described regimes ***(i)-(iv)***. Simultaneously, we also explain the existence of the primary and the secondary solution branches and the stable and unstable equilibria that constitute them. We conclude this section by suggesting an inverse strategy to programme other new confinement controlled responses in mechanical metamaterials whose deformations can be modeled by one-degree-of-freedom mechanisms. We propose that based on the trajectory of the mechanism, we can encode plenty of other equilibria sequence that unfold as the control parameter ϵ_x is varied.

We begin with deriving a convenient expression for the total elastic energy stored in the system U. We reuse the expression for the elastic energy stored in the horizontal springs, E_x from Eq. (2.9). Setting $k_x = 0.50$, we get

$$E_x = (x_i(\theta) - (1 - \epsilon_x))^2 \,. \tag{2.15}$$

We define a new quantity: $X_o = 1 - \epsilon_x$. The above equation now becomes:

$$E_x = (x_i(\theta) - X_o)^2 \,. \tag{2.16}$$

In a corresponding manner, we can write down the elastic energy stored in the vertical springs, E_y as:

$$E_y = (y_i(\theta) - Y_o)^2 \,, \tag{2.17}$$

where $Y_o = 1 - \epsilon_y$. Adding together the Eq. (2.16) and Eq. (2.17), we obtain a new expression for U:

$$U = (x_i(\theta) - X_o)^2 + (y_i(\theta) - Y_o)^2 \,. \tag{2.18}$$

M curve – The dependence of the internal coordinates x_i and y_i on θ are given by Eq. (2.7) and Eq. (2.8) respectively. In the (x, y) plane, the

locations of x_i and y_i as function of θ trace out an elliptical curve oriented at an angle $\pi/4$ with respect to the positive x-axis, but, for the relevant range $0 \leq \theta \leq \pi/2$, only a part of it. We refer to the curve relating x_i and y_i as **M** curve (**M** for mechanism). The eccentricity of this ellipse depends on the values of a and b and hence χ. The ellipse *approaches* a straight line $(x_i(\theta) = y_i(\theta))$ for $\chi \to 0$ and a circle $\left(x_i(\theta)^2 + y_i(\theta)^2 = \sqrt{2}\right)$ for $\chi \to 2$. For $\chi = 0.30$ ($a \approx 0.81$ and $b \approx 0.60$), **M** is shown in pink in Fig. 2.6(b).

Equi-energy circles – Eq. (2.18) implies that the equilibrium state(s) for fixed (X_o, Y_o) are given by the extrema of $U(\theta)$. These equilibrium state(s) determine the state of the soft mechanism. It is possible to extract these equilibria geometrically as follows: curves of equal energy in the (x, y) plane are circles with their center at (X_o, Y_o) and radius $\sqrt{U}$. With the center at (X_o, Y_o), the intersections of these circles with **M** form an *energy landscape*: $U(\theta)$, the extrema of which correspond to the equilibrium states of the mechanism. Through four different constructions, we will now cover some unique scenarios for fixed (X_o, Y_o). Mainly, these constructions will be helpful for the forthcoming discussion.

Fig. 2.6(a) shows examples of two concentric *equi-energy* circles originating from the center (X_o, Y_o). The circle $\mathbf{C_1}$, shown in blue, is a tangent to **M**, *touching* it at M_1, whereas the circle $\mathbf{C_2}$ (in red) with slightly larger radius, intersects **M** at two distinct points M_2 and M_3, which lie on the opposite sides of M_1. Circles intersecting **M** at the immediate vicinity of M_1 have larger radii than $\mathbf{C_1}$ and thus higher U. The local $U(\theta)$ landscape for the given (X_o, Y_o) has therefore a minimum at the value of θ_{M_1}, resulting in a stable equilibrium state.

Such constructions also find unstable equilibria. In Fig. 2.6(b), the positioning of the point (X_o, Y_o) allows to draw three tangential circles $\mathbf{C_1}, \mathbf{C_2}, \mathbf{C_3}$ to **M**, shown in the color blue, green and red respectively. These circles intersect **M** at M_1, M_2 and M_3. θ_{M_1}, θ_{M_2} corresponds to stable equilibrium states. The explanation is the same as earlier: the energy along the **M** increases away from the points of tangency. The case for M_3 is however opposite. Circles with slightly smaller radii than $\mathbf{C_3}$ can intersect **M** (at two distinct points) in the vicinity of M_3. The local $U(\theta)$ landscape has a maximum and hence θ_{M_3} corresponds to an unstable equilibrium configuration. Consistent with Fig. 2.6(b), we will, in the future, show the tangential circles for unstable states in dashed and solid for the stable

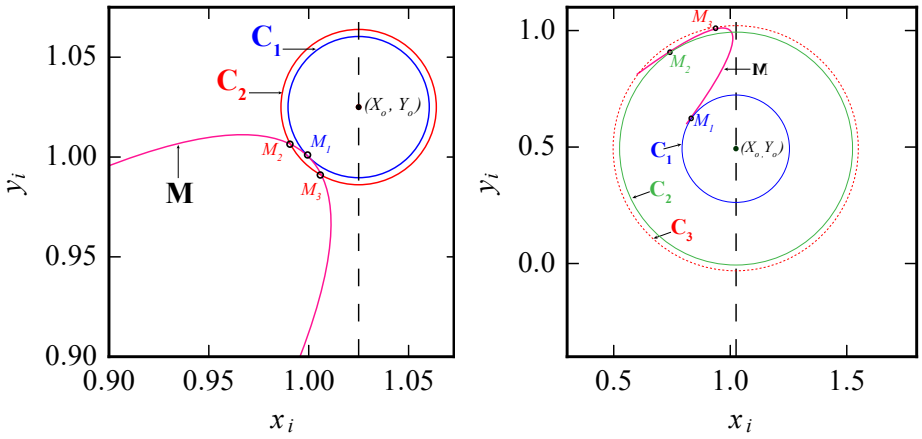

Figure 2.6: Given a fixed (X_o, Y_o), the equilibrium states (and their stability) of the soft mechanism can be geometrically determined by drawing tangential circles [Eq. (2.18)]. Positioning of the point (X_o, Y_o) can lead to different scenarios. (a) Circle $\mathbf{C_1}$, shown in blue, centered at (X_o, Y_o) touches $\mathbf{M}$ (in pink) at M_1. The internal energy U increases for a slightly larger circle $\mathbf{C_2}$ (in red) that intersects $\mathbf{M}$ at M_2 and M_3. The local $U(\theta)$ landscape has a local minimum at θ corresponding to M_1; θ_{M_1} corresponds to a stable equilibrium point. (b) From (X_o, Y_o), three tangential circles $\mathbf{C_1}, \mathbf{C_2}, \mathbf{C_3}$ to $\mathbf{M}$ (shown in blue, green and red respectively) can be constructed. These circles intersect $\mathbf{M}$ at M_1, M_2, M_3 respectively. With the same argument as in (a), it can be shown that θ_{M_1} and θ_{M_2} correspond to stable equilibrium points. θ_{M_3} however corresponds to an unstable solution; it is possible to construct circles with slightly smaller radii than $\mathbf{C_3}$ that intersect $\mathbf{M}$ at two distinct points in the immediate vicinity of M_3. The local $U(\theta)$ landscape thus has a maximum at θ_{M_3}.

states.

We now demonstrate two cases where the point (X_o, Y_o) is inside $\mathbf{M}$. (X_o, Y_o) in Fig. 2.7(a) is 'contained within' the cusp of the *evolute* $\sum$ (in black). The evolute of a curve is the locus of all its centers of curvature. The x and y coordinates of $\sum$, x_e, y_e can be expressed in terms of θ by the

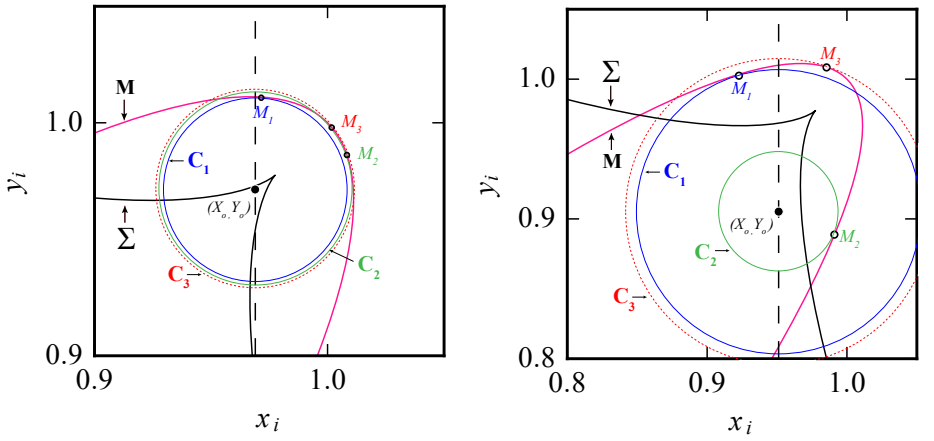

(a) (b)

Figure 2.7: Given a fixed (X_o, Y_o), the equilibrium states (and their stability) of the soft mechanism can be geometrically determined in terms of θ by drawing tangential circles [Eq. (2.18)]. We demonstrate it for two different constructions where the point (X_o, Y_o) is 'inside' $\mathbf{M}$ (in pink). **(a)** (X_o, Y_o) is *contained within* the cusp of evolute of $\mathbf{M}$, $\sum$ (in black). Three concentric circles - $\mathbf{C_1}, \mathbf{C_2}, \mathbf{C_3}$ (colored blue, green and red) can be constructed from (X_o, Y_o) that are tangential $\mathbf{M}$. $\mathbf{C_1}, \mathbf{C_2}, \mathbf{C_3}$ touch $\mathbf{M}$ at M_1, M_2 and M_3 respectively. M_1 and M_2 correspond to stable equilibrium solutions. M_3 however corresponds to an unstable equilibrium solution. This is true for any point on the dashed vertical line that is *contained within* $\sum$. **(b)** The three tangential circles $\mathbf{C_1}, \mathbf{C_2}, \mathbf{C_3}$ (colored blue, green and red) touch $\mathbf{M}$ at M_1, M_2 and M_3 respectively. Solutions are stable at M_1, M_2 and unstable at M_3.

following parametric equations:

$$x_e = x_i(\theta) - \frac{(a\cos\theta - b\sin\theta)(a^2 + b^2 - 2ab\sin 2\theta)}{a^2 - b^2}, \tag{2.19}$$

$$y_e = y_i(\theta) - \frac{(a\sin\theta - b\cos\theta)(a^2 + b^2 - 2ab\sin 2\theta)}{a^2 - b^2}. \tag{2.20}$$

Centered at (X_o, Y_o), it is possible to draw three tangential circles $\mathbf{C_1}, \mathbf{C_2}, \mathbf{C_3}$ (colored blue, green and red respectively) to $\mathbf{M}$ that form

tangencies at the points M_1, M_2, M_3. $\theta_{M_1}, \theta_{M_2}$ correspond to stable solutions whereas θ_{M_3} corresponds to an unstable solution. Similarly, the existence of two stable and one unstable equilibrium solution can be proved for any point on the dashed line in Fig. 2.7(a) that is contained within $\sum$. We will later encounter this case again when we discuss the geometrical interpretation of the regime ***(iii)***.

Fig. 2.7(b) shows the fourth and last example. We construct the three tangential circles $\mathbf{C_1}, \mathbf{C_2}, \mathbf{C_3}$ (colored blue, green and red respectively) to $\mathbf{M}$. These circles touch $\mathbf{M}$ at the points M_1, M_2, M_3. θ_{M_1}, θ_{M_2} correspond to stable equilibrium solutions whereas θ_{M_3} is an unstable equilibrium solution.

2.3.1 Mechanical Regimes from Geometrical Viewpoint

Loading with a fixed horizontal confinement requires fixing X_o and varying Y_o. Following this protocol, we present the geometrical interpretation of the regimes ***(i-iv)***.

Regime *(i)* – In Fig. 2.8(a), we show the result of following the procedure of fixing X_o and varying Y_o for $X_o = 1.015$ ($\epsilon_x = -0.015$). A set of circles $\{\mathbf{C}\}$ (shown in the color blue) with their center lying on the vertical line $x = X_o$ form a tangent to $\mathbf{M}$. The points of tangency are labeled by the black markers. As explained previously [Fig. 2.6(a)], these points correspond to (stable) equilibrium solutions, θ_{eq}. For a number of such circular constructions we find θ_{eq} and plot it against the vertical strain ϵ_y in Fig. 2.8(b) (color black). ϵ_y is calculated as 1 - Y_o. As explained previously through Fig. 2.6(b), for lower values of Y_o, one finds two additional equilibrium states - one stable and one unstable. The corresponding tangential circles are not shown in Fig. 2.8(a) to avoid cluttering. We show these additional θ_{eq} solutions in red in Fig. 2.8(b). The unstable states are shown in dashed. We now understand the genesis of the secondary solution branch for higher values of ϵ_y [Fig. 2.4(a)]. We note that the primary branch (in black) corresponds to $\theta < \tan^{-1}(a/b)$ and the secondary branch (in red) corresponds to $\theta > \tan^{-1}(a/b)$ [6].

Following the primary branch, the value of U initially decreases with ϵ_y, reaches a minimum (at $\theta = \tan^{-1}(b/a)$), and increases again. $U(\epsilon_y)$ looks similar to Fig. 2.5(a). $P(\epsilon_y)$ can be calculated as: $P = \Delta U/\Delta\epsilon_y$, which

[6] Note that at $\theta = \tan^{-1}(a/b)$, Eq. (2.11) is undefined.

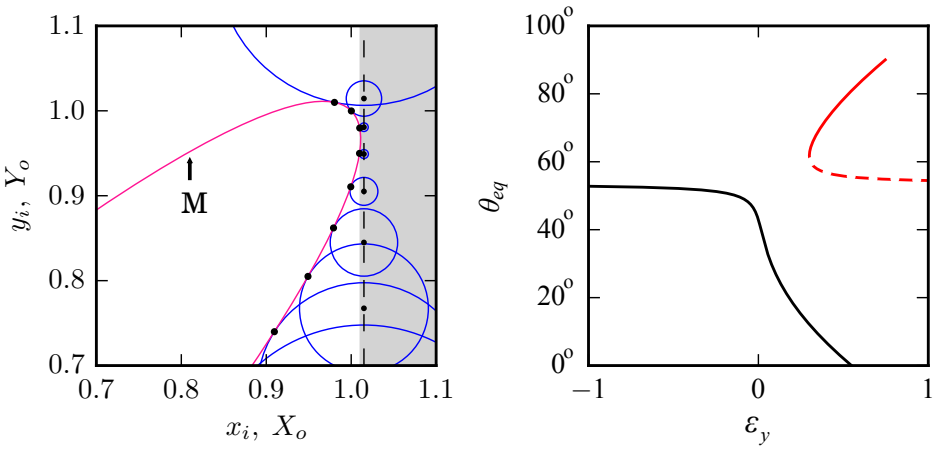

(a) **(b)**

Figure 2.8: (a) The geometrical interpretation of regime ***(i)***. The set of tangential circles $\{\mathbf{C}\}$ (in blue) to $\mathbf{M}$ (in pink) centered on the line $X_o = 1.015$ ($\epsilon_x = -0.015$), touch $\mathbf{M}$ at the labeled black markers. The points of tangency denote the equilibrium states of the soft mechanism, θ_{eq}. The shaded region belongs to the regime ***(i)***. (b) θ_{eq} vs ϵ_y. The primary branch is shown in black and the secondary branch is shown in red. Stable and unstable equilibria are shown in solid and dashed curve styles.

leads to a monotonic curve. The example corresponds to the regime ***(i)***. In fact the same arguments applies for any value of X_o within the gray-shaded region in Fig. 2.8(a).

Regime *(ii)* – Fig. 2.9(a) shows the geometrical approach for a smaller value of $X_o = 0.99$ ($\epsilon_x = 0.01$). In this case U reaches zero at two values of Y_o, which is where the line $x = X_o$ intersects $\mathbf{M}$. In between, U reaches a local maximum. Evidently, the graph of U vs ϵ_y would appear similar to the one shown in Fig. 2.5(b). This example corresponds to the regime ***(ii)***. Just as in the previous case, one still finds the secondary equilibria branch for lower values of Y_o. Both the primary and the secondary state branches are shown in Fig. 2.9(b) on a $\theta_{eq}(\epsilon_y)$ graph. In the previous section, we remarked that the 'dip' in the $P(\epsilon_y)$ curve in Fig. 2.4(b) occurs because of the polarization switch from x-polarized state to y-polarized

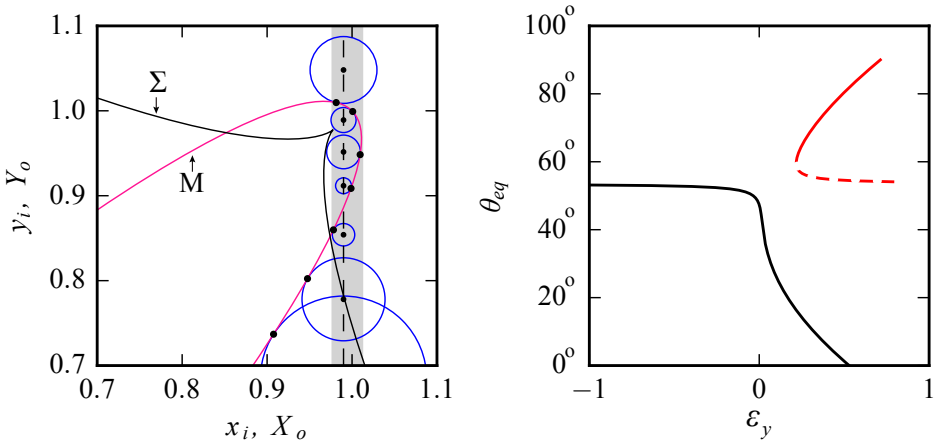

(a) **(b)**

Figure 2.9: (a) The geometrical interpretation of regime ***(ii)***. The set of tangential circles $\{\mathbf{C}\}$ (in blue) to $\mathbf{M}$ (in pink) centered on the line $X_o = 0.99$ ($\epsilon_x = 0.01$), touch $\mathbf{M}$ at the labeled black markers. The points of tangency denote the equilibrium states of the soft mechanism, θ_{eq}. The shaded region includes the values of X_o for regime ***(ii)***. (b) θ_{eq} vs ϵ_y. The primary branch is shown in black and the secondary branch is shown in red. Stable and unstable equilibria are shown as solid and dashed curves respectively.

state. $\theta_{eq}(\epsilon_y)$ graph substantiates the argument. $\theta_{eq}(\epsilon_y = 0.0) > \pi/4$ making the mechanism initially x-polarized. The polarization state changes to y-polarized state ($\theta_{eq}(\epsilon_y >> 0.0) < \pi/4$) under the application of the load P.

The transition between the regime ***(i)*** and the regime ***(ii)*** occurs where the line $x = X_o$ is tangent to the $\mathbf{M}$, at which point $x = (x_i(\theta))_{max}$ i.e. the maximum value of $x_i(\theta)$. We know that $\epsilon_x = 1 - X_o$. An analytic expression for the critical value of horizontal strain $(\epsilon_{xc})_{(i)-(ii)}$ marking the transition between regime ***(i)*** and regime ***(ii)*** can be given as:

$$(\epsilon_{xc})_{(i)-(ii)} = 1 - X_{o_{x=(x_i(\theta))_{max}}}. \tag{2.21}$$

We know that $x_i(\theta) = a\cos(\theta) + b\sin(\theta)$. $x_i(\theta)$ attains a maximum value at

$\theta = \tan^{-1}(b/a)$. Therefore,

$$(x_i(\theta))_{max} = a\cos\left(\tan^{-1}\left(\frac{b}{a}\right)\right) + b\sin\left(\tan^{-1}\left(\frac{b}{a}\right)\right). \tag{2.22}$$

Using the trigonometric identities: $\cos(\tan^{-1} x) = \dfrac{1}{\sqrt{1+x^2}}$ and $\sin(\tan^{-1} x) = \dfrac{x}{\sqrt{1+x^2}}$ and simplifying, we get:

$$(x_i(\theta))_{max} = \sqrt{a^2+b^2}. \tag{2.23}$$

Therefore,

$$(\epsilon_{xc})_{(i)-(ii)} = 1 - \sqrt{a^2+b^2}. \tag{2.24}$$

We will shortly show that the lower range of values of X_o which belong to regime ***(ii)*** are restricted unto where the vertical line $x = X_o$ intersects the 'nose' of the evolute $\sum$. Hence, the shaded region in Fig. 2.9(a) corresponds to regime ***(ii)***.

Regime *(iii)* – With a further decrease in the value of X_o, the vertical line $x = X_o$ crosses the evolute $\sum$ at three different points. Fig. 2.10(a) shows geometrical construction of tangential circles for one such case with $X_o = 0.972$ ($\epsilon_x = 0.028$). The present case is slightly non-trivial. We gradually decrease the value of Y_o, construct the *tangent circles*, and discuss the stability of the equilibrium states. For a proper demonstration, we make use of different colors. In Fig. 2.10(a), each (X_o, Y_o) and their point(s) of tangency are marked by a different color. We use the dashed curves to draw circles that correspond to unstable equilibrium. The first two equilibrium states are clearly stable (labeled by the *black* and *blue* markers). Consider now the case when the point (X_o, Y_o) lies on $\sum$ (***D***, ***C***, *red* marker). Emanating from this point, it is possible to construct two tangential circles. These circles touch **M** at the two labeled points D_M and C_M. The circles are shown in solid and dashed curve styles respectively because D_M corresponds to a stable equilibrium and C_M corresponds to an unstable equilibrium point. Similar is the argument for the other point (X_o, Y_o), lying on $\sum$ (***A***, ***B***, *green* marker). Once again, two tangential circles touch **M** at A_M and B_M which correspond to unstable and stable states respectively. As a matter of course, every point on **M** which lies *between* A_M and C_M corresponds to an unstable equilibrium solution. The trajectory

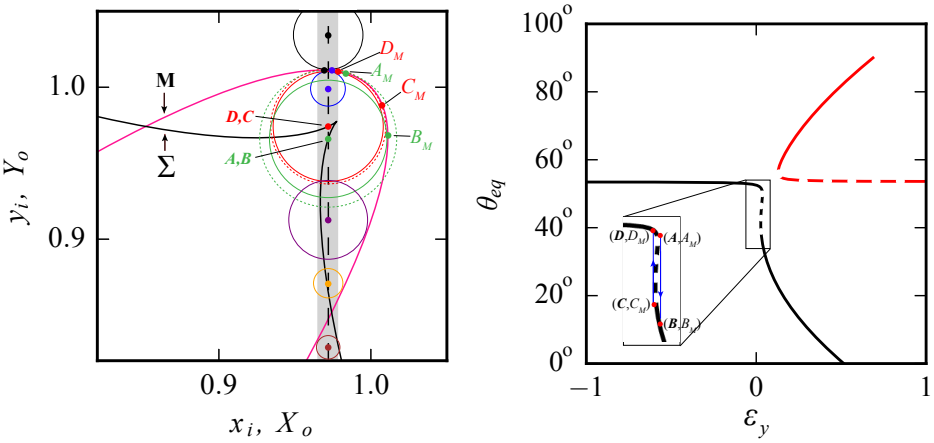

(a) **(b)**

Figure 2.10: (a) (a) The geometrical interpretation of regime ***(iii)***. The set of tangential circles {**C**} (in blue) to **M** (in pink) centered on the line $X_o = 0.972$ ($\epsilon_x = 0.028$), touch **M** at the labeled black markers. The points of tangency denote the equilibrium states of the soft mechanism, θ_{eq}. Shaded region belongs to the regime ***(iii)***. (b) θ_{eq} vs ϵ_y. The primary branch is shown in black and the secondary branch is shown in red. Stable and unstable equilibria are shown in solid and dashed curve styles. The primary branch encloses an unstable section, and multivaluedness is due to hysteresis.

of the mechanism along **M** from the point A_M to C_M corresponds to the movement from $\boldsymbol{A}$ to $\boldsymbol{C}$ of the point (X_o, Y_o) on the line $x = X_o$. This 'reverse course' is shown in dashed in Fig. 2.10(b). The result is an 'enclosed' unstable section on the primary branch. The points $\boldsymbol{A, B, C, D}$ are indeed the same points previously shown in Fig. 2.4(c), Fig. 2.5(c). We are in the regime ***(iii)***. In terms of θ, the mechanism makes hysteretic jumps from A_M to B_M during loading and from C_M to D_M during unloading. For lower values of Y_o, the equilibrium are stable (shown in the color purple, orange and brown). And, similar to the regimes ***(i)*** and ***(ii)***, additional equilibria are born for an even lower values of Y_o (not shown in the figure).

The transition from regime ***(ii)*** to regime ***(iii)*** occurs where the line $x = X_o$ just touches the cusp of $\sum$. This happens at $\theta = \pi/4$. The critical

value of the horizontal strain, $(\epsilon_{xc})_{(ii)-(iii)}$ marking the transition between regime ***(ii)*** and regime ***(iii)*** is given by:

$$(\epsilon_{xc})_{(ii)-(iii)} = 1 - X_{o_{x_e = x_e(\theta=\pi/4)}}. \tag{2.25}$$

From Eq. (2.19), we can calculate $x_e(\theta = \pi/4)$. We know that $x_i(\theta = \pi/4) = 1$.

$$x_e(\theta = \pi/4) = 1 - \frac{(a/\sqrt{2} - b/\sqrt{2})\,(a^2 + b^2 - 2ab)}{a^2 - b^2},$$

$$= 1 - \frac{(a-b)^2}{\sqrt{2}\,(a+b)},$$

$$= 1 - \frac{a^2 + b^2 - 2ab}{\sqrt{2}(a+b)}. \tag{2.26}$$

Because we have set $a+b = \sqrt{2}$, squaring both sides, we get $a^2+b^2 = 2-2ab$, we get:

$$x_e(\theta = \pi/4) = 2ab. \tag{2.27}$$

Therefore,

$$(\epsilon_{xc})_{(ii)-(iii)} = 1 - 2ab. \tag{2.28}$$

Regime *(iv)* – Fig. 2.11(a) shows the set of tangential circles $\{\boldsymbol{C}\}$ to $\mathbf{M}$ whose center lies on the vertical line $X_o = 0.96$ ($\epsilon_x = 0.04$). Black markers show the corresponding equilibrium states. We only show the equilibrium solutions that lie on the primary solution branch. Additional equilibrium states also exist which form the secondary solution branch [Fig. 2.7(b)]. We plot the equilibrium solutions on the $\theta_{eq}(\epsilon_y)$ graph [Fig. 2.11(b)]. U exhibits a single global minima and attains a value of zero where the line $x = X_o$ intersects $\mathbf{M}$. We are in the regime ***(iv)***. Unlike the previous three cases, the primary equilibrium solutions admit $\theta_{eq} > \tan^{-1}(a/b)$ while for the secondary solutions $\theta_{eq} < \tan^{-1}(a/b)$. In the vicinity of $\tan^{-1}(a/b)$, the solutions that were previously stable are now unstable and vice-versa. According to *bifurcation theory*, this corresponds to a *transcritical bifurcation* where at the critical value of the control parameter (ϵ_x), the two solutions meet and exchange stability. The transition between the regime ***(iii)*** and the regime ***(iv)*** occurs where the line $x = X_o$ is tangent to the evolute $\sum$, at which point $y = (y_i(\theta))_{max}$ i.e. the maximum value of $y_i(\theta)$. Therefore,

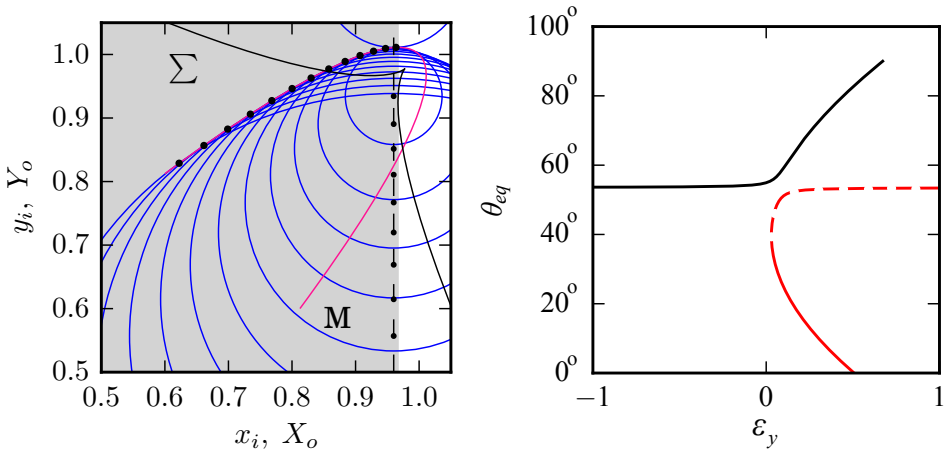

(a) **(b)**

Figure 2.11: (a) (a) The geometrical interpretation of regime ***(iv)***. The set of tangential circles $\{\mathbf{C}\}$ (in blue) to $\mathbf{M}$ (in pink) centered on the line $X_o = 0.96$ ($\epsilon_x = 0.04$), touch $\mathbf{M}$ at the labeled black markers. The points of tangency denote the equilibrium states of the soft mechanism, θ_{eq}. Shaded region belongs to the regime ***(iv)***. (b) θ_{eq} vs ϵ_y. The primary branch is shown in black and the secondary branch is shown in red. Stable and unstable equilibria are shown in solid and dashed curve styles.

the critical value of horizontal strain, $(\epsilon_{xc})_{\textit{(iii)}-\textit{(iv)}}$, marking the transition between regime ***(iii)*** and regime ***(iv)*** is given by:

$$(\epsilon_{xc})_{\textit{(iii)}-\textit{(iv)}} = 1 - X_{o_{x=(y_i(\theta))_{max}}}. \tag{2.29}$$

We know that $y_i(\theta) = a\sin(\theta) + b\cos(\theta)$. $y_i(\theta)$ attains a maximum value at $\theta = \tan^{-1}(a/b)$. Therefore,

$$\begin{aligned}(y_i(\theta))_{max} &= a\sin\left(\tan^{-1}\left(\frac{a}{b}\right)\right) + b\cos\left(\tan^{-1}\left(\frac{a}{b}\right)\right), \\ &= \frac{2ab}{\sqrt{a^2+b^2}}.\end{aligned} \tag{2.30}$$

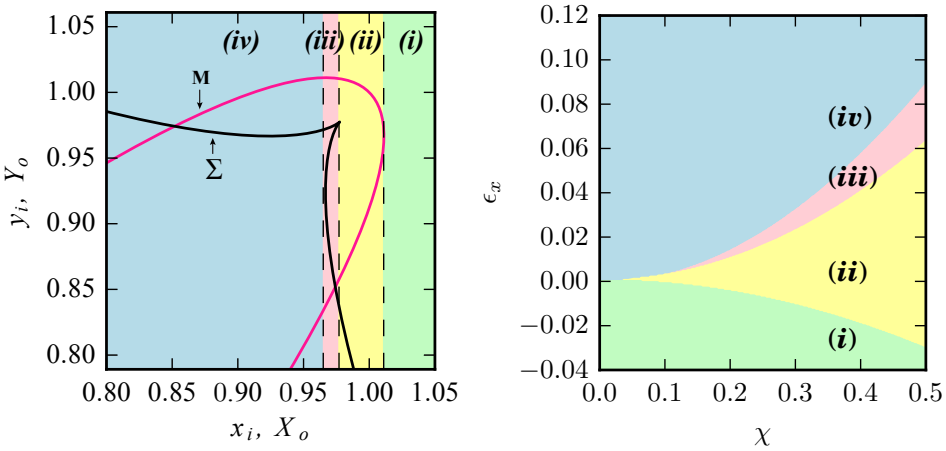

(a) **(b)**

Figure 2.12: (a) For $\chi = 0.30$, **M** and $\sum$ shown in pink and black respectively. The regimes ***(i)-(iv)*** are displayed in different colors and labeled. The dashed vertical lines demarcate the neighboring regimes. The critical value of ϵ_{xc}, which marks the transition from regime ***(i)*** to ***(i+1)*** can be calculated as: $(\epsilon_{xc})_{(i)-(i+1)} = 1 - X_{o_{(i)-(i+1)}}$. The generalized expressions for which are given by Eq. (2.24, 2.28, 2.31). (b) A regime transition plot for a range of χ based on the generalized expressions for transition among the subsequent regimes ***(i)-(iv)***. The four regimes are labeled and shown in the different colors.

The analytical expression for the critical value of horizontal strain $(\epsilon_{xc})_{(iii)-(iv)}$ is given as:

$$(\epsilon_{xc})_{(iii)-(iv)} = 1 - \frac{2ab}{\sqrt{a^2 + b^2}}. \tag{2.31}$$

For $\chi = 0.30$, we assemble the regimes ***(i)-(iv)*** together in one plot and show them in Fig. 2.12(a).

Regime transition plot – The generalized analytical expressions derived in Eq. (2.24, 2.28, 2.31) provide clear-cut boundaries for ϵ_{xc} which mark the transition between the successive regimes. We use these expressions to construct a *regime transition plot* for a range of values of χ.

In Fig. 2.12(b), we plot ϵ_{xc} for transitions between the regimes ***(i)-(iv)*** versus the biholarity χ. We vary χ from [0, 0.50]. We draw a couple of observations: *(i)* for low χ, the distinction among the four regimes diminishes which results in their convergence at $\epsilon_{xc} = 0.0$ for $\chi \to 0$ - weak symmetry breaking leads to a weak nonlinear coupling between ϵ_x and ϵ_y, making the two non-monotonic regimes ***(ii),(iii)*** vanish; monotonic regimes ***(i),(iv)*** dominate. *(ii)* With an increase in χ, we observe an expansion of the strain range over which regime ***(ii)*** prevails. This qualitatively matches with the experimental findings reported in [70], where it was found that for fixed ligament thickness t_l, $(\epsilon_{xc})_{(i)-(ii)}$ decreases with χ.

2.3.2 A General Design Strategy

The above described geometrical interpretation of the soft mechanism provides with an inverse strategy to rationally design metamaterials with confinement controlled response. The scheme is stated below.

Procedure – An inverse strategy to rationally design mechanical metamaterials with confinement controlled response.

Steps :

1: First, formulate a continuous sequence of equilibria that emerges as the control parameter ϵ_x is varied.

2: Second, construct the involute (evolute) curve that is consistent with the sequence of these equilibria.

3: Third, design a physical mechanism that posses this particular involute (evolute) trajectory, hypothetically which is possible as shown by Milton [24] - an extension of Kempe's universality theorem [72] for materials - where the main results states that "periodic structures made up of rigid bars and pivots can realize any given trajectory to an arbitrary high degree of approximation".

4: Finally, based on the underlying mechanism, construct a soft deformable metamaterial with slender hinge connectors.

2.4 Modeling the Finite Thickness Interhole Ligaments with Torsional Springs

Previously, we did not take into account the thickness of the interhole ligaments, t_l [Fig. 2.1(a)] and assumed the hinges in the mechanism to be ideal with zero energy costs for bending. In this section, we model the finite thickness of the interhole ligaments by coupling the hinges of the soft mechanism with torsional springs of $\pi/2$ rest angle. In this way, we introduce an additional penalty to change θ away from the neutral state, $\theta = \pi/4$. The total internal energy U now contains an extra term accounting for the bending energy stored in the torsional springs, E_t.

$$U = E_x + E_y + E_t, \tag{2.32}$$

where E_x and E_y are the elastic energies stored in the horizontal and vertical springs and are the same as given by Eq. (2.9) and Eq. (2.13) respectively. We will use the notation E_l to denote the total elastic energy stored in the linear springs, $E_l = E_x + E_y$. E_t at a general angle θ is given by:

$$\begin{aligned} E_t &= 2 \times \left(\frac{1}{2}\right) \times k_t \left(2\theta - \frac{\pi}{2}\right)^2 + 2 \times \left(\frac{1}{2}\right) \times k_t \left(\frac{\pi}{2} - 2\theta\right)^2, \\ &= 8k_t \left(\theta - \frac{\pi}{4}\right)^2. \end{aligned} \tag{2.33}$$

E_t is quadratic in θ with the minimum located at $\theta = \pi/4$. The expression for U is given as:

$$U = 2k_x \left(\epsilon_x + x_i(\theta) - 1\right)^2 + \frac{P^2}{2k_y} + 8k_t \left(\theta - \frac{\pi}{4}\right)^2, \tag{2.34}$$

where k_x, k_y and k_t are the horizontal, vertical and torsional spring constants respectively, ϵ_x is the external x-confinement, P is the load, and the expressions for $x_i(\theta)$ and $y_i(\theta)$ are given by Eq. (2.7), Eq. (2.8) respectively. We aim to derive an expression for P, the approach for which is same as described in §2.2.1, following which, we obtain:

$$P = \frac{-2k_x \left(\epsilon_x + x_i(\theta) - 1\right)\left(-a\sin\theta + b\cos\theta\right) - 4k_t\left(2\theta - \pi/2\right)}{\left(a\cos\theta - b\sin\theta\right)}. \tag{2.35}$$

The expression for ϵ_y is the same as earlier and is given by the Eq. (2.12).

With the help of an example, we now demonstrate the effect of k_t on the energy curves - E_l, E_t and U. In Fig. 2.13, energy curves are shown as a function of ϵ_y, and as a function of θ in Fig. 2.14 for a system with $\chi = 0.30$. Within each figure, E_l, E_t and U are shown in the color red, green and blue respectively. Note that only the primary equilibrium solution branches are shown. Fig. 2.13(a) displays the energy curves for $\epsilon_x = 0.028$ and $k_t = 0.0$. In this case, $U = E_l$ and the system is in regime ***(iii)***. U exhibits two global minima where $U = 0$. These minima exist on both the sides of $\theta = \pi/4$ in $U(\theta)$ plot [Fig. 2.14(a)]. Recall from the geometrical interpretation that this happens precisely where the vertical line $x = 0.028$ intersects the trajectory curve $\mathbf{M}$ [Fig 2.10(a)]. We now increase k_t, keeping ϵ_x fixed at 0.028. Fig. 2.13(b) shows the energy curves for $k_t = 5 \times 10^{-4}$. An emerging trend in the $U(\theta)$ curves should be noticed: an increase in the value of k_t gradually 'elevates' the energy landscape. In Fig. 2.14(b), we notice the gradual elimination of the minimum in U for $\theta < \pi/4$. The system is still in regime ***(iii)***, however. This, we confirm by plotting the force curves, $P(\epsilon_y)$. Utilizing the Eq. (2.34), Fig. 2.15 shows $P(\epsilon_y)$ for the same system as in Fig. 2.13 and Fig. 2.14. $P(\epsilon_y)$ in Fig. 2.15(a-b) is typical of regime ***(iii)*** - a non-monotonic multi-valued curve.

With a further increase in the value of k_t, its effect on the energy landscape grows. Fig. 2.13(c) and Fig. 2.14(c) shows the energy curves for $k_t = 3 \times 10^{-3}$. At this value of k_t, the nature of $P(\epsilon_y)$ is non-monotonic but single-valued [Fig. 2.15(c)] - characteristic of regime ***(ii)***. Ultimately for a high enough value of $k_t = 8 \times 10^{-3}$ [Fig. 2.13(d) and Fig. 2.14(d)], $U(\epsilon_y)$ ceases to display any sharp curvature change. The derivative of it, $P(\epsilon_y)$ is monotonic [Fig. 2.15(d)]. The system now is in regime ***(i)***. We conclude that high values of k_t push the mechanical response towards the regime ***(i)***.

Regime transition plots with torsional springs – Torsional springs alter the values of ϵ_{xc}, the critical horizontal strain values marking the transition among the successive regimes. We have already demonstrated that an increase in the value of k_t pushes the mechanical response of the system towards the regime ***(i)***; the values of ϵ_{xc} are expected to shift-up with k_t. Fig. 2.16 shows the regime transition plots for $k_t = 3 \times 10^{-3}$ in (a) and for $k_t = 8 \times 10^{-3}$ in (b). The values of ϵ_{xc} are now captured numerically unlike in Fig. 2.12(b), where we utilized direct analytical expressions. We

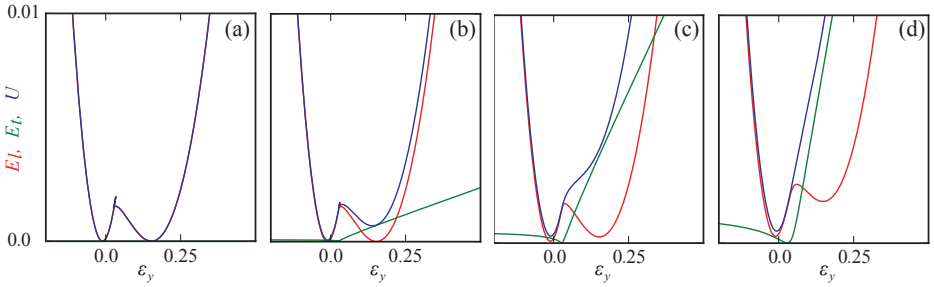

Figure 2.13: Energy curves shown as a function of ϵ_y for a system with $\chi = 0.30$, $\epsilon_x = 0.028$ and increasing values of k_t. E_l, E_t and U denote the elastic energy stored in the linear springs, torsional springs and total internal energy of the system and are shown in the color red, green and blue respectively. Note that we only show the primary solution branches. (a) $k_t = 0.0$, $U = E_l$. The plot is familiar [Fig. 2.5(c)]. The system is in the regime ***(iii)***. (b) $k_t = 5 \times 10^{-4}$, $U(\epsilon_y)$ displays multivaluedness and hysteresis. The system is in regime ***(iii)*** still. (c) $k_t = 3 \times 10^{-3}$, $U(\epsilon_y)$ displays curvature change. The system is in regime ***(ii)***. (d) $k_t = 8 \times 10^{-3}$, $U(\epsilon_y)$ consists of a single global minimum with no curvature change. The system now is in regime ***(i)***.

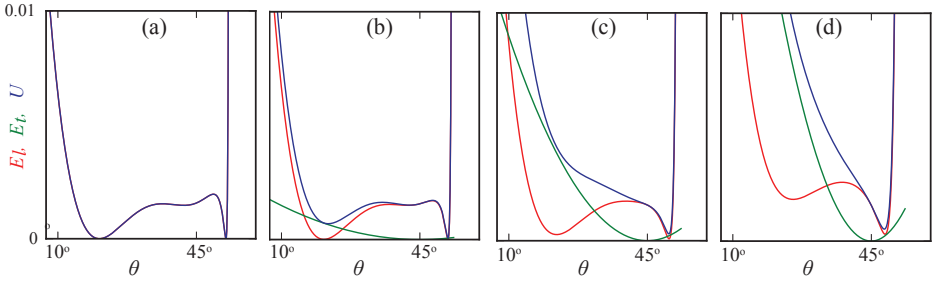

Figure 2.14: Energy curves shown as a function of θ for a system with $\chi = 0.30$, $\epsilon_x = 0.028$ and for the same four values of k_t as in Fig. 2.13. Symbols have the same meaning. We notice an emerging trend from (a)-(d) as the value of E_t dominates over E_l: gradual elevation of the minimum in U that exist on the either side of $\theta = 45°$. As E_t has a minimum at $\theta = 45°$, the minimum for $\theta < 45°$ gets strongly affected.

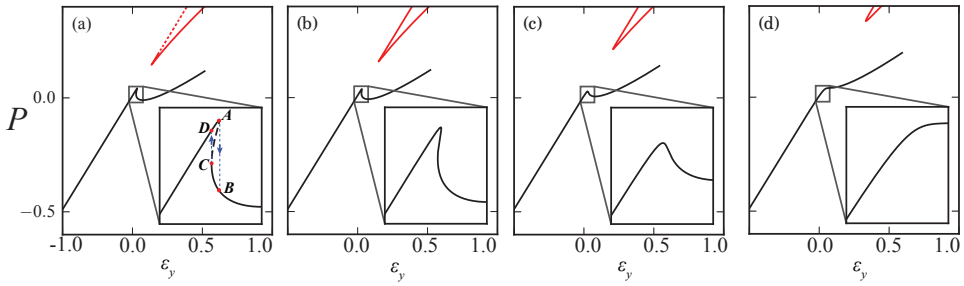

Figure 2.15: $P(\epsilon_y)$ for a system with $\chi = 0.30$, $\epsilon_x = 0.028$ and for increasing values of k_t. (a) $k_t = 0.0$, and (b) $k_t = 5{\times}10^{-4}$. $P(\epsilon_y)$ displays multi-valued owing to the hysteretic behavior in both the figures. The system is in the regime ***(iii)***. (c) $k_t = 3{\times}10^{-3}$, $P(\epsilon_y)$ is non-monotonic. The system is in the regime ***(ii)***. (c) $k_t = 8{\times}10^{-3}$, $P(\epsilon_y)$ is monotonic. The system is in the regime ***(i)***. We conclude that with an increase in the values of k_t, the mechanical response shifts towards regime ***(i)***.

fix the value of χ, the ϵ_{xc} values for transition between the consecutive regimes are then captured based on the change in the trajectory of the $P(\epsilon_y)$ curves. We notice the expected upward shift in the regime domains. It is worth noting that *(i)* an increase in the values of critical strain value, $(\epsilon_{xc})_{(i)-(ii)}$ which marks onset of regime ***(ii)*** with ligament thickness t_l and fixed χ is also observed in [70], *(ii)* increase in k_t makes the existence of all the four regimes for non-negative ϵ_x values, making them consistent with the experiments [Fig. 2.2].

We further characterize the results by plotting a variation in ϵ_{xc} with k_t for three different values of χ in Fig. 2.17 - (a) $\chi = 10^{-3}$, (b) $\chi = 0.30$, (c) $\chi = 0.50$. There, within each figure, we show $(\epsilon_{xc})_{(i)-(ii)}$ in blue, $(\epsilon_{xc})_{(ii)-(iii)}$ in green and $(\epsilon_{xc})_{(iii)-(iv)}$ in red. We draw several conclusions. *(i)* For $\chi = 10^{-3}$ [Fig. 2.17(a)], we do not observe the prevalence of non-monotonic regimes but effectively only the regimes ***(i)*** and ***(iv)*** exist. The scaling of ϵ_{xc} with k_t is linear with slope ≈ 4.0. We attempt to justify this in the next section. *(ii)* For $\chi = 0.30, 0.50$ [Fig. 2.17(b,c)], we observe that ϵ_{xc} for all the regime transitions scales linearly, although their slope values vary in a slightly complicated manner. Fig. 2.17(d) shows the variation in these slope values versus the biholarity χ. We vary χ in the range [0, 1]. Immediately we can notice that for $\chi \to 0$, the distinction among the four regimes

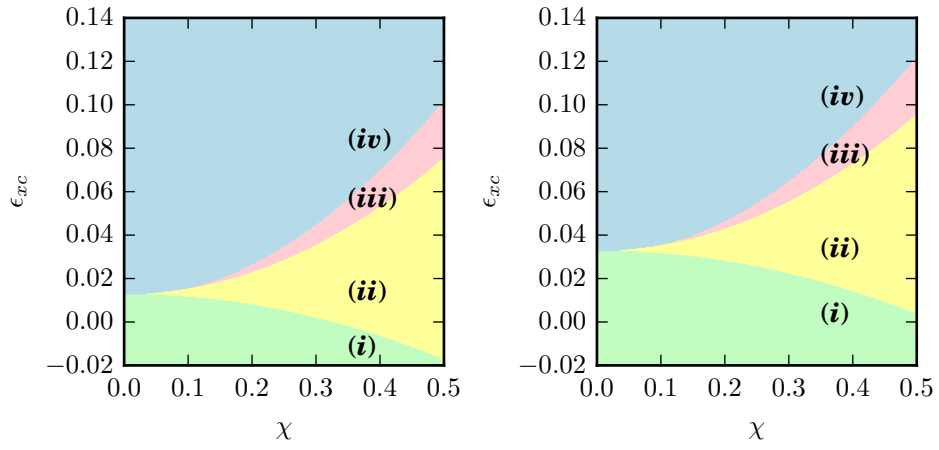

Figure 2.16: The effect of torsional spring constant k_t on ϵ_{xc}, the critical horizontal strain values that separate the contiguous regimes ***(i-iv)***. (a) $k_t = 3 \times 10^{-3}$, (b) $k_t = 8 \times 10^{-3}$. Regimes ***(i-iv)*** are labeled and shaded in different colors. Overall, we observe that for all biholarity χ, an increase in k_t shifts ϵ_{xc} towards higher values. We duly characterize our findings in Fig. 2.17.

vanishes and the value of $\Delta\epsilon_{xc}/\Delta k_t \to 4$. Moving away towards higher χ values, we interestingly notice that $(\Delta\epsilon_{xc}/\Delta k_t)_{(ii)-(iii)}$ is not dependent on χ and maintains a constant value equal to 4. $(\Delta\epsilon_{xc}/\Delta k_t)_{(i)-(ii)}$ and $(\Delta\epsilon_{xc}/\Delta k_t)_{(iii)-(iv)}$, however exhibit an exponential increase with χ, with the effect being stronger in the former than later.

2.5 Weak Symmetry Breaking in Monoholar Systems

In this section, we probe the limiting case where the biholarity χ, of the system approaches the value zero. We remember that χ serves as a measure of the relative difference between the diameters of the two neighboring holes (§2.2). We first briefly introduce the case where the holes are of exactly the same size, and through the help of concepts from *bifurcation theory*,

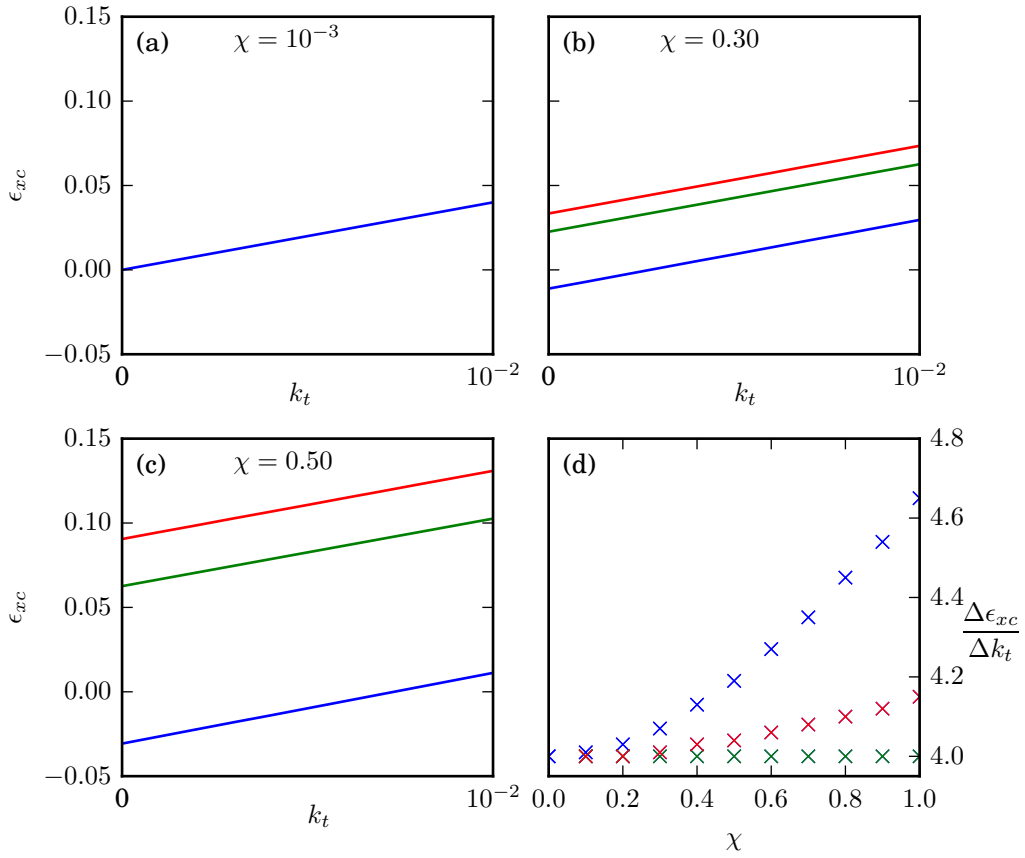

Figure 2.17: (a-c) The scaling of ϵ_{xc} with k_t for different χ values. (a) $\chi = 10^{-3}$, (b) $\chi = 0.30$ and (c) $\chi = 0.50$. Within each figure, $(\epsilon_{xc})_{(i)-(ii)}$ is shown in blue, $(\epsilon_{xc})_{(ii)-(iii)}$ is shown in green and $(\epsilon_{xc})_{(iii)-(iv)}$ is shown in red. The variation of slopes of these linear curves is shown in (d). We observe that $(\Delta\epsilon_{xc}/\Delta k_t)_{(ii)-(iii)}$ is independent of χ and maintains a constant value equal to 4. $(\Delta\epsilon_{xc}/\Delta k_t)_{(i)-(i)}$ and $(\Delta\epsilon_{xc}/\Delta k_t)_{(iii)-(iv)}$, however exhibit an exponential increase with χ. The distinction among the four regimes vanishes for $\chi \to 0$ with $\Delta\epsilon_{xc}/\Delta k_t \to 4$.

show how the original pitchfork bifurcation structure gets disturbed upon inducing small symmetry breaking by making the hole sizes slightly unequal. This is called *unfolding* of the bifurcation. We derive the equation describing

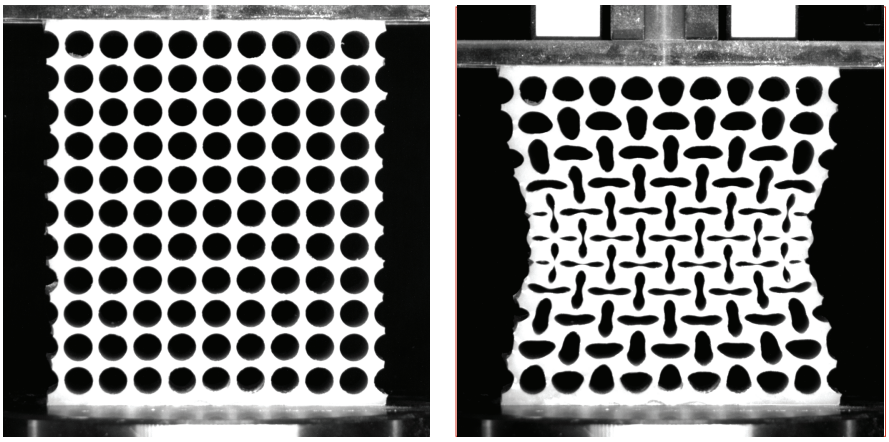

(a) **(b)**

Figure 2.18: (a) Monoholar sheet: an elastic slab perforated with an alternating pattern of equi-sized circular holes on a square array. (b) When compressed beyond a critical value of the vertical strain, the monoholar sheet undergoes a pattern transformation triggered by elastic instability and reaches a state of mutually orthogonal ellipses. Monoholar sheet exhibits a negative value of the Poisson's ratio (μ) [74] and forms a classical example of the auxetic materials. The hole diameter of the sample is 8.5 mm, the connector filament thickness (previously denoted by t_l for the biholar sheet) is 1.5 mm and the out-of-plane thickness of the sample is 35 mm. These images are adopted from [73].

this unfolding in §2.5.1 and deploy it to understand the case where $\chi \to 0$ in §2.5.2. We ultimately provide with a justification for the observed value of $(\Delta\epsilon_{xc}/\Delta k_t) \to 4.0$ for $\chi \to 0$ in the previous section [Fig. 2.17(d)].

Monoholar sheet, $\chi = 0$ – Fig. 2.18(a) shows a quasi-2D elastic slab patterned with equal sized circular holes [73]. We call this a *monoholar sheet*. The hole diameter of the sample is 8.5 mm, the connector filament thickness (previously denoted by t_l for the biholar sheet) is 1.5 mm and the out-of-plane thickness of the sample is 35 mm. A monoholar sheet with finite interhole ligament thickness such as this undergoes an initial gradual and homogeneous compression in the linear elastic range, where the circular holes deform in a uniform fashion. Upon reaching a critical vertical strain,

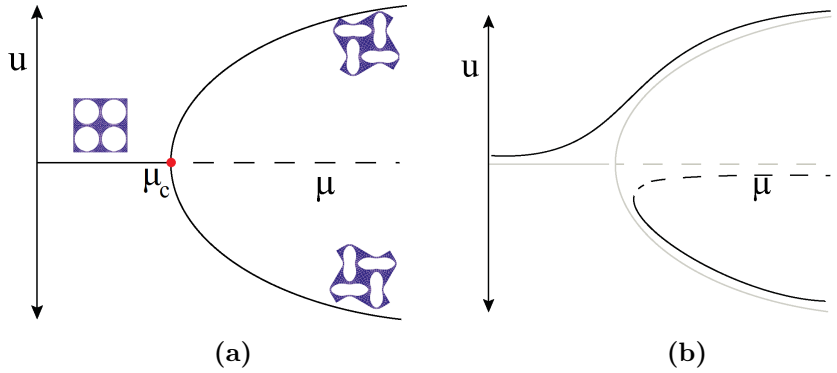

Figure 2.19: (a) Compression of a monoholar sheet illustrated through a perfect pitchfork bifurcation diagram. The vertical axis (u) represents the angular displacement of the 'center line' connecting the interhole ligaments and the horizontal axis (μ) denotes the vertical compression. Beyond the critical value μ_c, there is equal probability that the system forms either of the two (shown) elliptic arrangements. (b) Introduction of slight symmetry breaking into the system, $\chi \neq 0$ disturbs the original bifurcation diagram, making it imperfect. The system displays a tendency to follow either of the two non-trivial solutions. In the two diagrams, the stable and the unstable equilibria are shown in solid and dashed curves respectively.

the interhole ligaments undergo a buckling instability, thereby triggering a pattern transformation to a state with mutually orthogonal ellipses [Fig. 2.18(b)] [74]. After buckling, the stability gets transferred from the original symmetric state to the symmetry broken state. If the memory effects are discounted, the alternating polarization pattern of the elliptical holes is completely arbitrary because of the equal likeliness of a particular ellipse to orient its major axis along the x-direction or along the y-direction. In bifurcation theory, this case of equal likeliness of a system to follow either of the two solution branches once the critical value of a control parameter (vertical strain in this case) is reached is referred to as the system being at the *bifurcation point* of a *perfect pitchfork bifurcation* [75].

The situation can be illustrated through a pitchfork bifurcation diagram [Fig 2.19(a)] [7]. The vertical axis, u represents the state of the system such as the angular displacement of the 'center line' connecting the neighboring

[7] We explain this case mathematically in §2.5.2.

elastic units, while the horizontal axis, μ denotes the vertical compression. In the diagram, the stable equilibrium solution branches are shown in solid while the unstable branches are shown in dashed. One usually concentrates on the stable solutions since these are the only ones one observes in experiments [76]. For $\mu < \mu_c$, the critical value of the *control parameter*, there is only one equilibrium solution branch - corresponding to elastic compression without any formation of the elliptic pattern. Beyond μ_c, this solution becomes unstable and instead two new stable solutions are born. These new solutions correspond to the two 'oppositely' buckled states, wherein the holes are oppositely polarized and which are equally likely to occur.

Perturbed monoholar sheet, $\chi \neq 0$. Imperfect bifurcation diagrams occur when small symmetry breaking terms destroy the original bifurcation structure [77]. Weak symmetry breaking leads to an *imperfect* pitchfork bifurcation, causing the system to prefer one of the two solution branches [Fig 2.19(b)]. A monoholar system with a weak symmetry breaking, $\chi \neq 0$ forms one such example. Upon compression, the mutually orthogonal ellipse pattern is no longer arbitrarily selected by the bifurcation but in fact can be manipulated. Specifically from the point of view of confinement controlled experiments, the polarization pattern depends on the values of strains in the horizontal and vertical directions. Unlike for a perfect monoholar system, where the horizontal strain ϵ_x and the vertical strain ϵ_y play a similar role, in a system with broken symmetry, these strains each favor a different polarization of the pattern (§2.1, [Fig. 2.1(b,c)]). Their interactions typically results in the system to prefer one out of the two stable solution branches. The interactions between these two branches result in the complex mechanics of a confined biholar sheet [20].

Several bifurcation scenarios emerge as we perturb the perfect monoholar system and vary the parameters ϵ_x and ϵ_y. These scenarios arise from the unfolding of the pitchfork bifurcation [75]. To understand the local bifurcation scenarios, in the following section, we probe the system for the limiting case. Our aim is to obtain a *general equation* valid around the singular point that provides us with the complete description of the nature of the bifurcations and transitions. We will establish that the general equation resembles the *normal form* [8] of an imperfect pitchfork bifurcation

[8] Normal form of a bifurcation are in a sense, the simplest possible polynomial equation which contains the bifurcation [77].

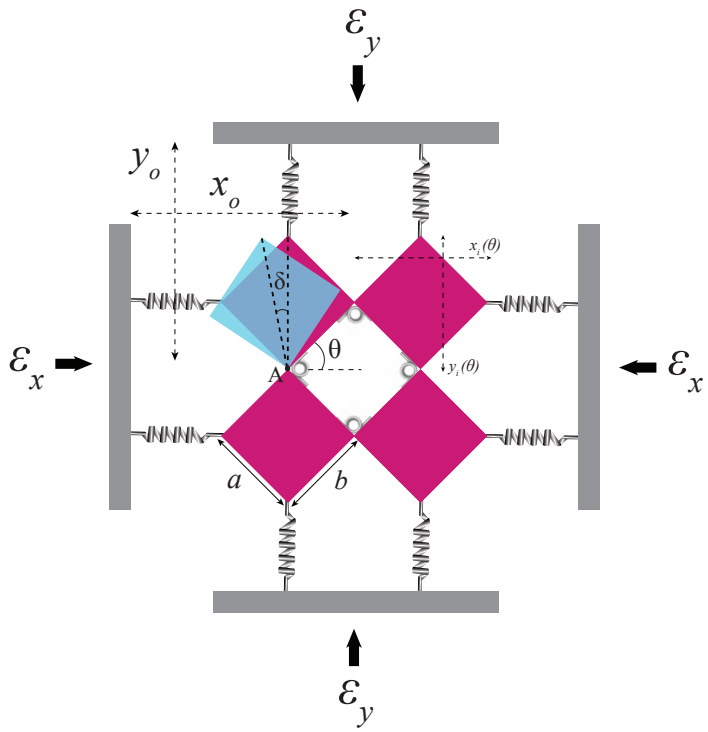

Figure 2.20: Soft mechanism for a monoholar system, $\chi \to 0$ ($a \approx b$) consisting of pin-jointed squares. We examine the system for small torsional spring constant k_t and small angular displacement δ.

and utilize this equation to describe the physics of the perfect monoholar as well as a perturbed monoholar system. To this end, we exploit the soft mechanism for a system with $\chi \to 0$ under external loading [Fig. 2.20] and conduct the analysis for weak angular displacements by following an approach based on the method of *Lagrange multipliers*.

2.5.1 Soft Mechanism for a Perturbed Monoholar System

In this section, we derive an equation describing the equilibrium states of the mechanism shown in Fig. 2.20 under the application of horizontal strain ϵ_x and vertical strain ϵ_y for small torsional spring constant k_t and small biholarity χ. To achieve this, we minimize the total internal energy

of the system, U [Eq. (2.32)], subjected to geometrical constraints in the horizontal and vertical directions. The Lagrangian $\mathcal{L}$ can be expressed as:

$$\mathcal{L} = U + \lambda_1 C_1 + \lambda_2 C_2,$$

$$= E_x + E_y + E_t + \lambda_1 C_1 + \lambda_2 C_2, \tag{2.36}$$

where the familiar symbols: E_x, E_y and E_t have the same meaning as previous (§2.4). λ_1 and λ_2 are the Lagrange multipliers for the associated geometrical constraints C_1 and C_2. Below, we explain these constraints.

Horizontal constraint C_1 – Let $l_{i,h}$ denote the rest length of the horizontal springs. For the initial state of the mechanism, we can then write:

$$l_{i,h} + x_i\,(\pi/4) = x_o \tag{2.37}$$

where $x_i(\pi/4)$ is the initial x-dimension of the rigid unit of the mechanism [Eq. (2.7)]. Suppose that upon the application of a small horizontal strain, ϵ_x, the diagonal of the rigid unit rotates about the point A by a small angle δ. One can then write:

$$\epsilon_x + l_{f,h} + x_i\,(\pi/4 + \delta) = x_o, \tag{2.38}$$

where $l_{f,h}$ denotes the final length of the horizontal spring upon the application of ϵ_x. We denote the net change in the length of the springs by e_x, given by:

$$e_x = l_{i,h} - l_{f,h},$$

$$= \epsilon_x + x_i\,(\pi/4 + \delta) - 1. \tag{2.39}$$

Using Eq. (2.7), we can expand $x_i(\pi/4 + \delta)$ and write e_x as:

$$\begin{aligned} e_x &= \epsilon_x + a\cos\,(\pi/4 + \delta) + b\sin\,(\pi/4 + \delta) - 1, \\ &= \epsilon_x + \cos\delta - \frac{\sin\delta(a-b)}{\sqrt{2}} - 1. \end{aligned} \tag{2.40}$$

We term $(a-b)/\sqrt{2}$ as *symmetry breaking parameter* and denote it with m. For a monoholar system, m takes on the value zero. Substituting $(a-b)/\sqrt{2}$ with m, the above equation can be written as:

$$e_x = \epsilon_x + \cos\delta - m\sin\delta - 1 \tag{2.41}$$

The constraint C_1 is therefore given by:

$$C_1 = e_x - \epsilon_x - \cos\delta + m\sin\delta + 1 = 0. \tag{2.42}$$

Vertical constraint C_2 – Similarly, we impose the geometrical constraint for the vertical direction and find that:

$$C_2 = e_y - \epsilon_y - \cos\delta - m\sin\delta + 1 = 0. \tag{2.43}$$

Expressions for E_x, E_y and E_t – The energy stored in the horizontal springs, E_x can be expressed as:

$$E_x = 4 \times \frac{1}{2} k_x e_x^2 = 2k_x \left(\epsilon_x + cos\delta - msin\delta - 1\right)^2. \tag{2.44}$$

The energy stored in the vertical springs, E_y is given by:

$$E_y = 4 \times \frac{1}{2} k_y e_y^2 = 2k_y \left(\epsilon_y + cos\delta + msin\delta - 1\right)^2. \tag{2.45}$$

The energy stored in the torsional springs, E_t is given by:

$$E_t = 4 \times \frac{1}{2} k_t \times (2\delta)^2 = 8k_t\delta^2. \tag{2.46}$$

Using Eq. (2.42)-(2.46), the Lagrangian, $\mathcal{L}$ [Eq. (2.36)] can now be written as:

$$\begin{aligned}\mathcal{L} = {} & 2k_x \left(\epsilon_x + cos\delta - msin\delta - 1\right)^2 + 2k_y \left(\epsilon_y + cos\delta + msin\delta - 1\right)^2 + 8k_t\delta^2 \\ & + \lambda_1(e_x - \epsilon_x - \cos\delta + m\sin\delta + 1) + \lambda_2(e_y - \epsilon_y - \cos\delta - m\sin\delta + 1).\end{aligned} \tag{2.47}$$

We impose the following equilibrium conditions in order to maintain quasi-staticity:

$$\frac{\partial \mathcal{L}}{\partial e_x} = 0 \implies \lambda_1 = -4k_x(\epsilon_x + cos\delta - msin\delta - 1) \tag{2.48}$$

$$, \frac{\partial \mathcal{L}}{\partial e_y} = 0 \implies \lambda_2 = -4k_y(\epsilon_y + cos\delta + msin\delta - 1) \tag{2.49}$$

$$\begin{aligned} \frac{\partial \mathcal{L}}{\partial(\delta)} = 0 \implies & 4k_x(\epsilon_x + cos\delta - msin\delta - 1)(-\sin\delta - m\cos\delta) + \\ , \quad & 4k_y(\epsilon_y + cos\delta + msin\delta - 1)(-\sin\delta + m\cos\delta) + \\ & 16k_t\delta + \lambda_1(\sin\delta + m\cos\delta) + \\ & \lambda_2(\sin\delta - m\cos\delta) = 0. \end{aligned} \tag{2.50}$$

Substituting the values of λ_1 and λ_2 from Eq. (2.48) and Eq. (2.49) respectively in the Eq. (2.50), we obtain:

$$\begin{aligned} & k_x(\epsilon_x + cos\delta - msin\delta - 1)(\sin\delta + m\cos\delta) + \\ & k_y(\epsilon_y + cos\delta + msin\delta - 1)(\sin\delta - m\cos\delta) - 2k_t\delta = 0. \end{aligned} \tag{2.51}$$

We set $k_x = k_y = k_l$ and obtain:

$$\begin{aligned} & (\epsilon_x + cos\delta - msin\delta - 1)(\sin\delta + m\cos\delta) + \\ & (\epsilon_y + cos\delta + msin\delta - 1)(\sin\delta - m\cos\delta) - \frac{2k_t\delta}{k_l} = 0. \end{aligned} \tag{2.52}$$

Since we are interested in small angular displacements, we expand the expressions for $\sin\delta$ and $\cos\delta$ around $\delta = 0$ up to the third order, and thus writing $\sin\delta$ as $\delta - \delta^3/6$ and $\cos\delta$ as $1 - \delta^2/2$, we obtain:

$$\begin{aligned} & \left(\epsilon_x - \frac{\delta^2}{2} - m\delta + m\frac{\delta^3}{6}\right)\left(\delta - \frac{\delta^3}{6} + m - m\frac{\delta^2}{2}\right) + \\ & \left(\epsilon_y - \frac{\delta^2}{2} + m\delta - m\frac{\delta^3}{6}\right)\left(\delta - \frac{\delta^3}{6} - m + m\frac{\delta^2}{2}\right) - \frac{2k_t}{k_l}\delta = 0. \end{aligned} \tag{2.53}$$

Simplifying the above equations and neglecting the terms higher than δ^3 and m, we end up with the final equation:

$$m(\epsilon_x-\epsilon_y)+(\epsilon_x+\epsilon_y-\frac{2k_t}{k_l})\delta-\frac{m}{2}(\epsilon_x-\epsilon_y)\delta^2-\left(\frac{\epsilon_x}{6}+\frac{\epsilon_y}{6}+1\right)\delta^3=0. \quad (2.54)$$

Reorganizing the above equation, we obtain:

$$\frac{m(\epsilon_x-\epsilon_y)}{(\frac{\epsilon_x}{6}+\frac{\epsilon_y}{6}+1)}+\frac{(\epsilon_x+\epsilon_y-\frac{2k_t}{k_l})}{(\frac{\epsilon_x}{6}+\frac{\epsilon_y}{6}+1)}\delta-\frac{m}{2}\frac{(\epsilon_x-\epsilon_y)}{(\frac{\epsilon_x}{6}+\frac{\epsilon_y}{6}+1)}\delta^2-\delta^3=0. \quad (2.55)$$

We recognize this as an unfolding of a pitchfork bifurcation. The normal form of a perfect (*supercritical*) pitchfork bifurcation is given by:

$$\mu u-u^3=0, \quad (2.56)$$

where u characterizes the state of the system and μ is the bifurcation parameter. The normal form of a perturbed pitchfork bifurcation is given by:

$$\alpha+\mu u-\beta u^2-u^3=0, \quad (2.57)$$

where, α and β are two real unfolding parameters [78]. Clearly, Eq. (2.55) resembles the normal form of an imperfect pitchfork bifurcation. We further confirm this by plotting a bifurcation diagram in the (ϵ_y,δ) space. We can reshuffle Eq. (2.55) and express ϵ_y explicitly as a function of δ and other parameters:

$$\epsilon_y=\frac{m\epsilon_x+\left(\epsilon_x-\frac{2k_t}{k_l}\right)\delta-m\epsilon_x\frac{\delta^2}{2}+\left(\frac{-\epsilon_x}{6}-1\right)\delta^3}{\left(m-\delta-m\frac{\delta^2}{2}+\frac{\delta^3}{6}\right)}. \quad (2.58)$$

We use the above equation to plot the bifurcation diagram shown in Fig. 2.21 for a system with $m=10^{-2}$, $k_t=0$ and for a range of small values of horizontal strain ϵ_x (see colorbar on the right) and confirm visually that indeed Eq. (2.55) represents unfolding of a pitchfork bifurcation as we vary ϵ_x. In principle, the trends in Fig. 2.17(d) are contained in Eq. (2.55). Here, we focus on the $\chi\to 0$ ($m\to 0$) limit, which allows us to establish $(\Delta\epsilon_{xc}/\Delta k_t)=4.0$ for $\chi\to 0$.

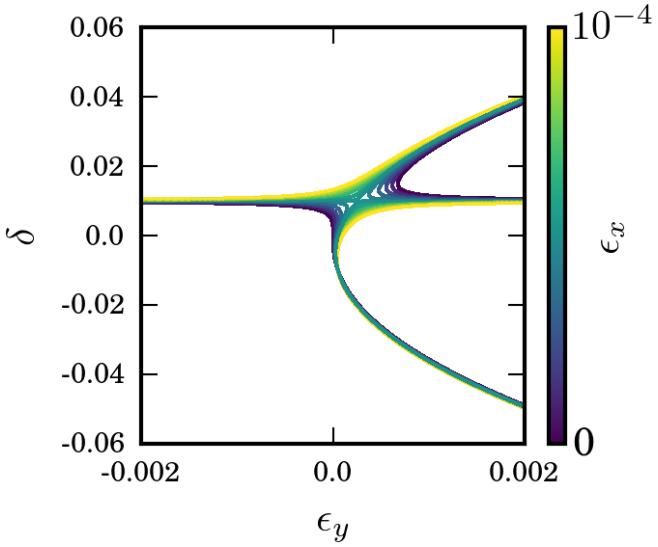

Figure 2.21: Based on Eq. (2.58), the unfolding of an imperfect pitchfork bifurcation confirmed for a system with $\chi \to 0$ ($m = 10^{-2}$), $k_l = 0.50$, $k_t = 0.0$ in the (ϵ_y, δ) space and for a series of small values of ϵ_x.

2.5.2 Perfect Pitchfork Bifurcation

We consider the case for a monoholar system for which the value of the symmetry breaking parameter $m = 0$. Substituting $m = 0$ in Eq. (2.55) leads to:

$$\frac{(\epsilon_x + \epsilon_y - \frac{2k_t}{k_l})}{(\frac{\epsilon_x}{6} + \frac{\epsilon_y}{6} + 1)}\delta - \delta^3 = 0. \tag{2.59}$$

Clearly, the above equation resembles the normal form of the pitchfork bifurcation given by Eq. (2.56). Let us assume $\left(\epsilon_x + \epsilon_y - \dfrac{2k_t}{k_l}\right) / \left(\dfrac{\epsilon_x}{6} + \dfrac{\epsilon_y}{6} + 1\right) = \mu$. The critical points then become:

$$\delta_1 = 0, \quad \delta_2 = \sqrt{\mu}, \quad \delta_3 = -\sqrt{\mu}. \tag{2.60}$$

These three solution branches intersect at the bifurcation point $\mu = 0$ (i.e. $\epsilon_x + \epsilon_y = 2k_t/k_l$), $\delta = 0$. We can rewrite Eq. 2.59 as:

$$f(\delta, \mu) = \mu\delta - \delta^3 = 0. \tag{2.61}$$

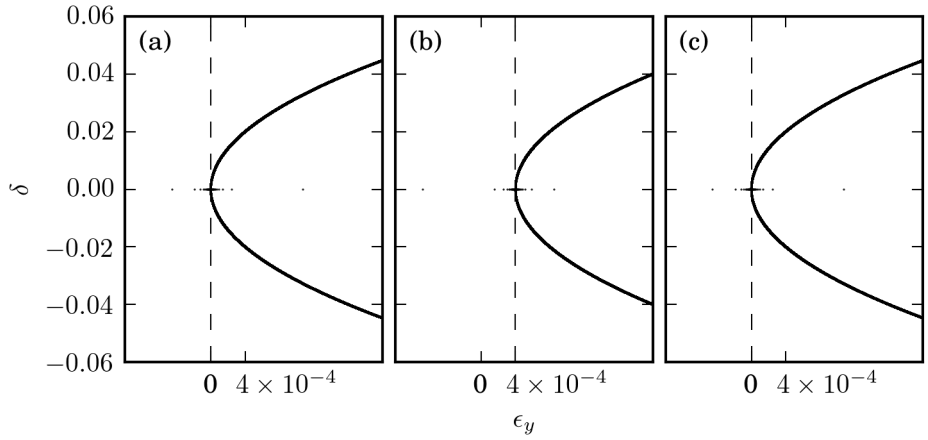

Figure 2.22: Pitchfork bifurcations diagrams for a monoholar system with symmetry breaking parameter $m = 0$ in (ϵ_y, δ) phase space (based on Eq. 2.59), $k_l = 0.50$ and for specific values of ϵ_x and k_t. (a) $\epsilon_x = 0.0, k_t = 0.0$. $\epsilon_y = 0.0, \delta = 0.0$ is the bifurcation point. (b) $\epsilon_x = 0.0, k_t = 10^{-4}$. The bifurcation point shifts horizontally towards the right at $\epsilon_y = 4\times10^{-4}$. (c) $\epsilon_x = 4 \times 10^{-4}, k_t = 10^{-4}$ brings the bifurcation point back at $\epsilon_y = 0.0, \delta = 0.0$.

Thus,

$$f_\delta(\delta_1, \mu) = \mu, \quad f_\delta(\delta_{(2,3)}, \mu) = -2\mu. \tag{2.62}$$

Therefore, the solution branch δ_1 is stable if $\mu < 0$, whereas the branches δ_2 and δ_3 are stable if $\mu > 0$. δ_1 and $\delta_{2,3}$ have opposite stability and exchange stability at $\mu = 0$,$\delta = 0$. We use Eq. 2.59 to construct bifurcation diagrams for a monoholar system in the phase space (ϵ_y, δ) for specific values of ϵ_x and k_t. We keep k_l fixed at 0.50. Fig. 2.22(a) shows the bifurcation diagram for $\epsilon_x = 0, k_t = 0$. We have a perfect pitchfork bifurcation with $\epsilon_y = 0, \delta = 0$ being the bifurcation point. From an experimental point of view, the monoholar sheet with negligible bending stiffness of the interhole ligaments buckles right at the application of the vertical strain. Fig. 2.22(b) shows the diagram for $\epsilon_x = 0, k_t = 10^{-4}$. We notice a horizontal shift towards right in the bifurcation diagram. The new bifurcation point is now at $\epsilon_y = 4 \times 10^{-4}, \delta = 0$, which is where μ takes on the value zero. Hence, in our model, a monoholar sheet with a finite stiffness of the interhole ligaments

initially undergoes an elastic compression before undergoing bucking and the subsequent pattern transformation. Finally, keeping $k_t = 10^{-4}$, we change the value of ϵ_x to 4×10^{-4} - the bifurcation diagram shifts to the left, thus retaining $\epsilon_y = 0, \delta = 0$ as the bifurcation point - a finite critical value of ϵ_x tightly compresses the horizontal ligaments, whose buckling occurs right at the onset of the vertical strain.

We draw a couple of important conclusions based on Eq. (2.59): *(i)* ϵ_x and ϵ_y are interchangeable and play similar roles for a symmetrical monoholar system, and *(ii)* from the point of view of confinement controlled experiments, it can be seen that if $\epsilon_x = 2k_t/k_l$, the system is at the bifurcation point. We have also shown this diagrammatically through Fig. 2.22. We use this observation to justify the scaling of ϵ_{xc} with k_t for systems with $\chi \to 0$ [Fig. 2.17(a)]. We notice that for $k_l = 0.50$, the critical value of ϵ_x required to set the system at the bifurcation point scales linearly with slope 4. Hence, we rationalize the numerical observation shown in Fig. 2.17(a).

2.6 Conclusions

We have shown that the physics of confined quasi-2D mechanical metamaterials can be captured by a seemingly simple mechanisms of rotating polygons. As a particular example, we demonstrated that a spring-coupled mechanism consisting of pin-jointed rectangles, called the soft mechanism (§2.2), is able to fully model the experimentally observed complex mechanical behavior (regimes $\boldsymbol{(i)} - \boldsymbol{(iv)}$) of a confined biholar sheet [20].

We then understood the transition from one regime to another and the involved bifurcations from solely a geometrical perspective, and outlined a generic strategy to rationally design the mechanical metamaterials with the desired confinement controlled response. To model a more realistic scenario, we coupled the hinges of the soft mechanism with torsional springs. We found out that this leads to an increase in the values of ϵ_{xc}, the critical strain values at which the regime transitions occur. Finally, we explored the soft mechanism for the limiting case where $\chi \to 0$. We demonstrate that, near this singularity, the different mechanical regimes emerge from the unfolding of an imperfect pitchfork bifurcation.

Acknowledgments

The work presented in this chapter is part of an industrial partnership programme (IPP) *'Computational Sciences for Energy Research (CSER)'* started in 2012, and funded by the Shell Global Solutions International B.V., the Netherlands Organization for Scientific Research (NWO) and the Foundation for Fundamental Research on Matter (FOM).

Chapter 3

Rational Design of Flexible Yet Generic 2D Mechanical Metamaterials

Abstract – In this chapter, we describe a nature-inspired algorithm based optimization methodology to design flexible yet generic 2D mechanical metamaterials. The procedure is based on optimizing the design of the underlying idealized hinging mechanism such that a target curve that characterizes the internal motion is achieved. To perform this, we utilize *Particle Swarm Optimization (PSO)* [60]. Through hyperparameter optimization for the governing PSO parameters, i.e. ω - *inertial weight*, c_1 - *cognition parameter* and c_2 - *social parameter*, we will demonstrate that the search behavior of PSO gets strongly influenced by these parametric setting. We will locate the 'sweet-spot' in the parameter space and establish that low values of c_1 and high values of c_2 are conducive for our particular problem, while ω plays a minor role. To verify the role of parametric setting, we adopt *Sammon's Mapping* as a technique to reduce dimensionality and visualize the search process. We further show that these parametric settings affect the statistical distribution type of the final solution. We show PSO generated a vast number of unique structures whose hinging motion is very close to that of a single degree-of-freedom mechanism, while their spatial structure shows that they are far from true single degree-of-freedom mechanisms. We characterize PSO by probing the search from a statistical point of view and distinguish solutions corresponding to true local

minima from those that are not. Finally, we introduce a method to obtain regular 2D tesselations that shadows the deformation pattern of its constituting unit cell. We bring these computer-designed structures to real life through 3D printing and retrieve ideal deformation patterns experimentally.

3.1 Introduction

In several cases, the deformation behavior of 2D mechanical metamaterials can be mapped onto hinging structures consisting of rotating rigid units connected together through *pin-joints* (hinge-joints). Such structures can consist of polygons or rods or a combination of both [18,38–41], . Well known examples include a rich variety of systems describing the observed *auxetic* (*Poisson's ratio*, $\nu < 0$) behavior. For example, the *NPR polyurethane foam* with re-entrant structure reported by Lakes et al. that had a negative value of ν = -0.70, can be idealized to a hinging/flexing re-entrant honeycomb structure [Fig. 3.1] [79]. J.N. Grima et al. and others identified numerous single degree-of-freedom mechanisms that show auxetic behavior emerging from rotating rigid units, eg. triangles, squares, different-sized squares, or rectangles [Fig. 3.2 (a-b)] [40, 80–82]. Al Grant examined which 'irregular' polygons can render fully hinging tessellation and showed that similar mechanisms can be constructed through trapezoids and cyclic quadrilaterals by connecting them together in a special manner, [Fig. 3.2 (c-d)] [83]. In a more recent work, A. Rafsanjani reported a class of reconfigurable 2D materials exhibiting simultaneous auxeticity and structural bistability, the deformation pattern of which can essentially be mapped onto hinging mechanisms [36].

In fact, the main scheme behind the design of these *mechanism-based metamaterials* is to base the desired deformation mode of the unit cell upon the zero-energy, free motion mode of an underlying idealized mechanism [38]. Suitable arrangements of such unit cells enable to achieve highly nonlinear bulk behavior [37]. For the *low-energy deformations* of these materials to closely follow the zero-energy motion of the underlying mechanism, hinge geometry plays a critical role, the elastic-distortions introduced by which are ideally minimized by connecting stiffer elements with slender, flexible connectors [38, 39].

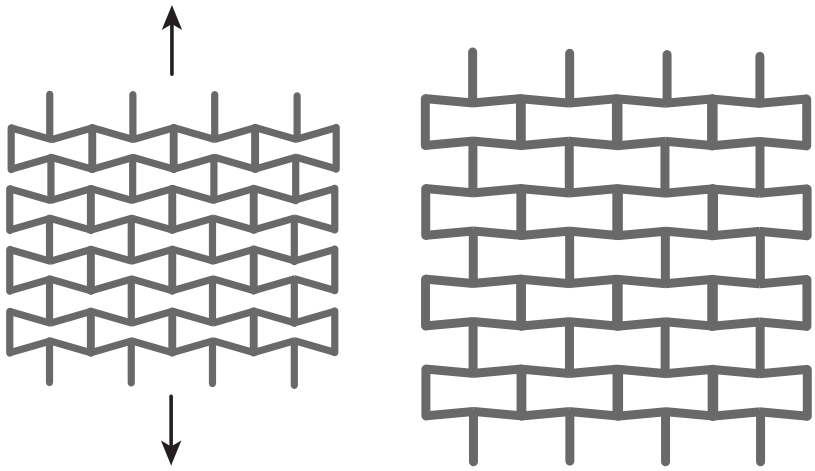

Figure 3.1: (a) Contracted, and (b) expanded states of a re-entrant honeycomb structure which deforms predominantly via the hinging mechanism of the diagonal ribs. Re-entrant honeycomb is a typical example among structures exhibiting negative Poisson's ratio, ν , also known as auxetics [79].

Rational design – Mechanism-based metamaterials are prevalent - careful geometrical design of the constituting rigid elements of the mechanism allows to achieve arbitrary complex internal deformations [41]. Concurrently, this also opens up the opportunities to come up with rational strategies to reversely design for a desired target behavior. Surprisingly, little attention has been paid towards this. Important contributions include [84–86]. Still, majority of the earlier reported examples have been designed through intuition or trial based strategies; thus the mechanical properties emerge as a result of the design. This explains why many of the examples have a periodically repeating subunit element. However, aperiodic structures lying hidden in the design space can be discovered by an optimization-based strategy to design a structure such that it meets a certain target criteria. Following this approach, the focus of this chapter is to design generic flexible 2D mechanical metamaterials consisting of hinging blocks, when a target functionality characterizing the internal deformation of the underlying mechanism consisting of pin-jointed quadrilaterals is desired.

It is important to note that generic pin-jointed quadrilaterals can never

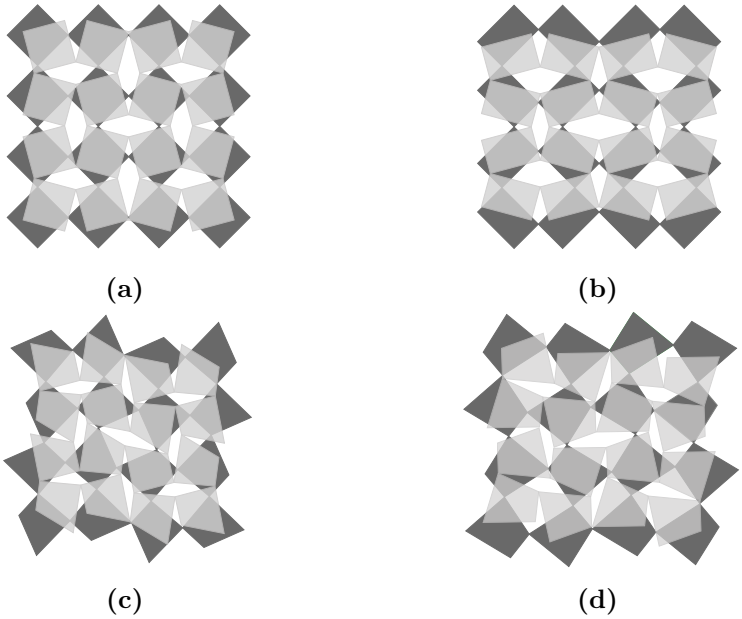

Figure 3.2: Single degree-of-freedom (DOF) mechanisms consisting of pin-jointed (a) squares, (b) rectangles, (c) trapezoids and (d) cyclic quadrilaterals. These mechanisms exhibit scale-independent auxetic behavior. The neutral states are shown in the color dark gray and the deformed states are shown in the color light gray [40, 80, 83].

form *exact mechanisms*. We show this through a counting argument on a limiting case in the following discussion and provide a formal proof in §3.2. There we also demonstrate the possibility that (fortunately) such systems can at best form *approximate mechanisms* i.e. near-perfect mechanisms [35]. From an optimization point of view, it means that these systems correspond to approximate solutions situated at deep local minima in the *objective function landscape* (assuming a minimization problem at hand), and the global minima are occupied by the exact mechanisms. This is not entirely bad considering: *(i)* the tendency of metaheuristics to get trapped inside the deep local minima, and *(ii)* that the 'good-quality' approximate solutions serve well for practical purposes.

Maxwell's counting rule – Before sketching the design process, we will first present the possibility for the existence of generic approximate mechanisms consisting of pin-jointed quadrilateral polygons. Maxwell introduced a simple rule for calculating the *degree(s)-of-freedom (DOF)* of networks consisting of bars and pin-joints according to which a system having n rigid bodies connected through j joints will have $3n - 2j - 3$ *non-trivial DOF* i.e. excluding the global translational and rotational DOF [87]. The explanation is as follows: each rigid body independently can have 3 DOF i.e. translation in x and y directions and a global rotation. Thus, n rigid bodies should have $3n$ DOF. Coupling these bodies through pin-joints brings constraints into the system with each joint removing 2 DOF [1], leading to a total count of $3n - 2j - 3$ non-trivial DOF.

We utilize this counting argument now. We begin with a closed network formed by four arbitrarily shaped pin-jointed polygons [Fig. 3.3(a), color dark gray]. Maxwell's formula predicts that the network has 1 non-trivial DOF, which corresponds to the internal deformation mode. Essentially the polygons form the boundary of a four-bar linkage, which is the simplest movable closed-chain linkage. The system in its deformed state is shown in light gray. Through the same counting argument, one can confirm that the networks shown in Fig. 3.3(b,c) also have 1 non-trivial DOF, thereby forming a mechanism [2]. However, applying Maxwell's formula to a 3x3 network [Fig. 3.3 (d)] leads to a 0 non-trivial DOF. This implies that generally 3x3 networks do not contain any internal mechanism and are instead rigid, monostable systems.

States of self-stress and isostaticity – However, Maxwell's formula does not takes into account the geometry of the system - non-generic examples, such as the 3x3 network sections of Fig. 3.2 contain an internal mechanism! The counting of redundant constraints in Maxwell's formula causes this discrepancy. In order to correctly calculate the non-trivial DOF for systems consisting of possible redundant constraints, Calladine extended Maxwell's rule as: number of non-trivial DOF $= 3n - 2j - 3 + n_{ss}$, where n_{ss}

[1] Imagine a system where two rigid polygons are connected through a pin-joint. If for the first polygon, its position in terms of x and y coordinates and rotational information is provided, then we only require the rotational information of the second polygon to specify the full configuration of the system.

[2] Although to what degree does the mechanism deforms internally cannot be answered immediately.

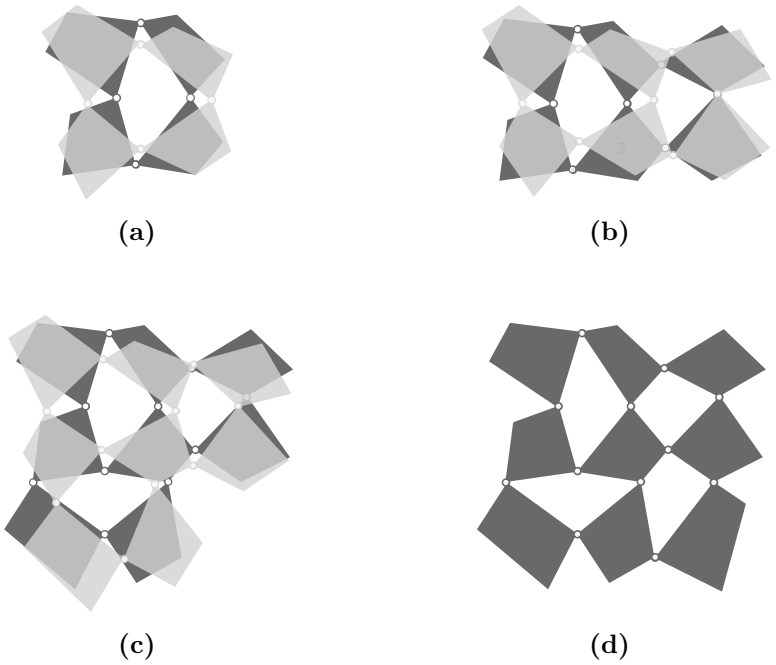

Figure 3.3: Networks of pin-jointed generic polygons. Counting of the non-trivial degree(s) of freedom (DOF) by the Maxwell's rule [87] reveals that (a)-(c) has 1 DOF and (d) has 0 DOF. Such generic 3x3 networks cannot form perfect mechanisms, however special geometric configurations may allow to form *approximate mechanisms*.

is the total number of *states of self-stress* [88]. Non-generic 3x3 networks contain one internal non-trivial DOF. Hence, for these systems $n_{ss} = 1$. On the other hand, generic 3x3 networks generally have zero non-trivial DOF and have therefore $n_{ss} = 0$. Such marginal systems that do not contain any internal zero mode nor have any states of self-stress are called *isostatic systems* [11, 89].

> Still, if the polygonal shape is such that one out of the total 24 constraints is 'almost' redundant, the possibility of generic 3x3 networks forming approximate mechanisms exists.

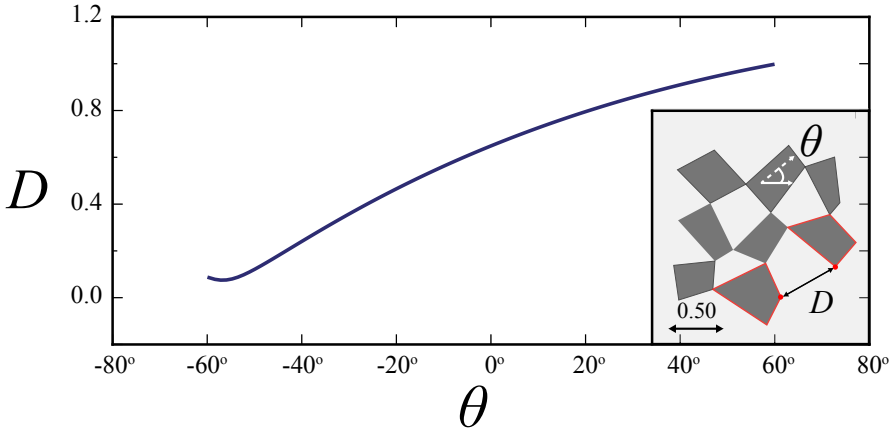

Figure 3.4: The $D(\theta)$ curve. A characteristic curve that captures the internal deformation of the eight-polygon mechanism shown in the inset figure. D (labeled) records the distance between the 'open vertices' of the specific red-bordered polygons and θ records the amount of internal deformation of the mechanism. The method of measuring θ is explained in §3.4.1 and for now it suffices to know θ as a parameter that measures the amount of internal deformation.

***D*(*θ*) curve** – We focus on the network shown in Fig. 3.3(c) that has an internal mechanism. Once the geometric information of each individual polygon is specified, only one independent variable is required, in terms of which the complete configuration of the system can be described. We use the parameter θ shown in Fig. 3.4(inset) as a measure of how much the *eight-polygon mechanism* has deformed internally[3] and plot the distance D between the 'open' unconnected corners as a function of θ. We will refer to this characteristic plot as $D(\theta)$ curve or $D(\theta)$ function. The $D(\theta)$ curve of one such example is shown in Fig. 3.4. The shape of individual polygons determines the trajectory of $D(\theta)$ curve, which can result in different possibilities if the 3x3 network is completed:

(i) Monotonic $D(\theta)$ curves — A rigid system: a monotonic $D(\theta)$ curve

[3] θ is more clearly defined in §3.4.1 but for now it suffices to know θ as a parameter that measures the amount of internal deformation.

implies that for every value of θ, there is a unique value of D. Therefore, with the connecting edge length of the ninth polygon within the given range of D, there is only one configuration of the 3x3 network that can be realized.

(ii) Quasi-constant and constant $D(\theta)$ curves — An approximate mechanism : a $D(\theta)$ curve with a *quasi-constant* value of D corresponds to an approximate 3x3 mechanism when the ninth polygon has edge length equal to the mean value of D. With suitable material type and hinge geometry, mechanical metamaterials based on these approximate mechanisms can feature a single low-energy deformation mode. In the current chapter, we focus on this case. Strictly constant $D(\theta)$ curve would lead to exact 3x3 mechanisms.

(iii) Parabolic (or more complex) $D(\theta)$ curves — A bi(multi)-stable 3x3 system consisting of stiffer elements connected with flexible hinges is possible if the $D(\theta)$ curve has same values of D for two (multiple) values of θ. We explore this case in the next chapter.

The $D(\theta)$ curve of the eight-polygon mechanism serves as a functionality to measure the flexibility of the 3x3 networks. The question of designing flexible 3x3 networks can thus be framed as a typical design optimization problem: optimize the design parameters which specify the polygonal shapes such that a specified constant target curve $D_t(\theta)$ is achieved to an arbitrarily high degree of approximation. Classical techniques, mainly based on gradient-finding methods, are likely to fail in such optimization problems concerning high dimensionality [56]. A much more advantageous choice in such cases are population based evolutionary search heuristics such as genetic algorithms, genetic programming, evolutionary strategies, swarm algorithms and other nature-inspired algorithms which rely on the principles of selection (competition) and reproduction (cooperation) among the population members [57–62]. In the current work, we implement one such algorithm inspired by the food searching capability of a bird flock: *Particle Swarm Optimization (PSO)* [60, 90, 91].

The outline of this chapter is as follows. In the next section, §3.2, we describe the ideal *loop condition* which allows a 3x3 network of polygons to form a perfect mechanism; forming the mathematical basis for our search. We describe the numerical tool to obtain discretized $D(\theta)$ curve of an arbitrary eight-polygon mechanism in §3.3. We lay down the entire

machinery for optimization-based design methodology in §3.4-§3.6, which includes the description of PSO, its optimal parameter settings and their effect on the distribution type of final solutions. We utilize Sammon's mapping to visualize the search process in §3.7 and gain understandings about the effect of PSO parameters on the search behavior. We show the actual optimized structures and characterize the search exploration of PSO in §3.8. Finally, in §3.9, we show the 3D printed samples and suggest a method to tile the flexible unit cells into periodic tessellations - the *metatilings*.

3.2 Mathematical Loop Condition

In the previous section, we learned that generically the 3x3 networks are rigid or monostable, although special polygonal shapes can possibly exist for which the network approaches to a mechanism. In this section, we will establish an ideal *loop condition*, the proximity of whose fulfillment determines how close a 3x3 network can get to form a mechanism.

Transmission function — Consider a (hypothetical) 3x3 mechanism shown in Fig. 3.5. The network consists of 'internally connected' four four-bar linkages, $\Lambda_1, \Lambda_2, \Lambda_3$ and Λ_4. In order to analyze this system, we will begin with a single constituent four-bar linkage and relate its input and output angles in terms of its bar lengths.

Consider a planar four-bar linkage O_AABO_B show in Fig. 3.6. The linkage consists of four pin-connected rigid bars with bar lengths a_1, a_2, a_3 and a_4 (grounded). The input bar a_1 makes an angle α, while the output bar makes an angle β with the grounded bar a_4. In terms of the geometrical parameters a_1, a_2, a_3 and a_4, our aim would be to relate the input angle α with the output angle β of the linkage. Consider the rectangular coordinate system O_Axy with respect to which the x and y coordinates of A - (x_2, y_2) and B - (x_3, y_3) may be written as follows:

For A: $\quad x_2 = a_1 \cos\alpha; \quad y_2 = a_1 \sin\alpha \ ,$

For B: $\quad x_3 = -a_4 + a_3 \cos\beta; \quad y_3 = a_3 \sin\beta.$

Since the distance AB is fixed and is equal to a_2, application of Pythagoras'

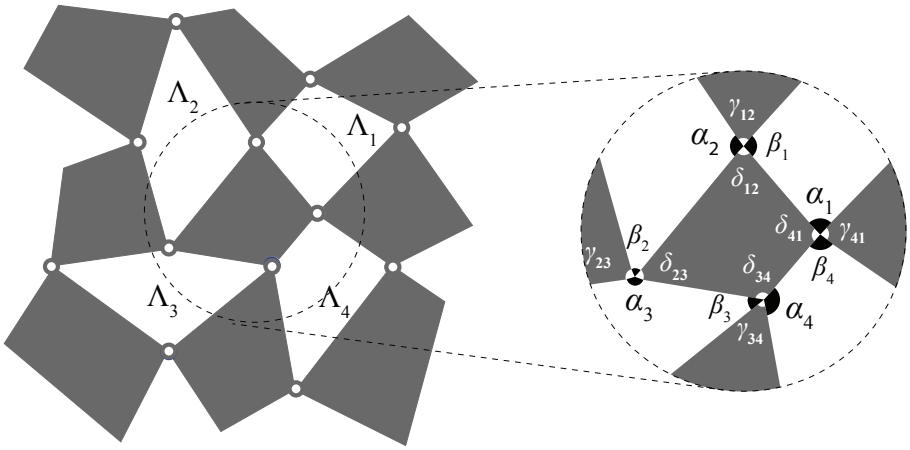

Figure 3.5: A (hypothetical) 3x3 mechanism consisting of four internal four-bar linkages: $\Lambda_1, \Lambda_2, \Lambda_3$ and Λ_4. For a linkage Λ_i, the input and the output angles are labeled as α_i and β_i respectively. $\gamma_{i,i+1}$ and $\delta_{i,i+1}$ are the fixed vertex angles that conjugate the linkages Λ_i and Λ_{i+1}. Subscripts follow a cyclic order.

theorem yields:

$$(x_2 - x_3)^2 + (y_2 - y_3)^2 = a_2^2 \,. \tag{3.1}$$

Substituting the values of x_2, y_2, x_3 and y_3 in Eq. (3.1) gives:

$$(a_1 \cos\alpha + a_4 - a_3 \cos\beta)^2 + (a_1 \sin\alpha - a_3 \sin\beta)^2 = a_2^2 \,. \tag{3.2}$$

After trigonometric simplifications, the above equation may be written as:

$$A \sin\beta + B \cos\beta = C, \tag{3.3}$$

where:

$$A = \sin\alpha, \qquad B = \frac{a_4}{a_1} - \cos\alpha, \qquad C = -\frac{a_4}{a_3}\cos\alpha + \frac{a_1^2 - a_2^2 + a_3^2 + a_4^2}{2a_1a_2} \,.$$

Expressing $\sin\beta$ and $\cos\beta$ in terms of $\tan(\beta/2)$:

$$\sin\beta = \frac{2\tan(\beta/2)}{1+\tan^2(\beta/2)}, \qquad \cos\beta = \frac{1-\tan^2(\beta/2)}{1+\tan^2(\beta/2)} \,.$$

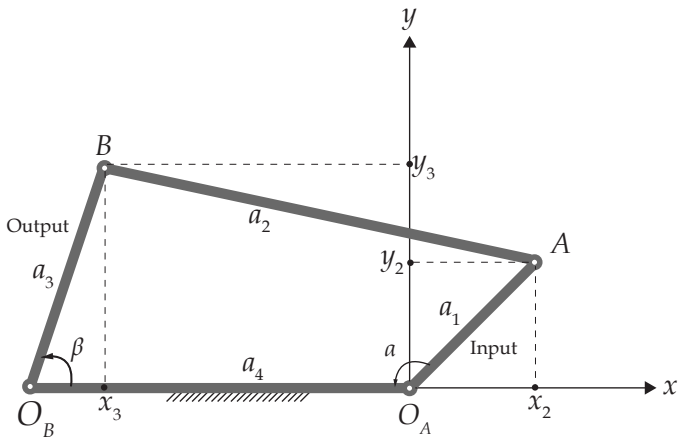

Figure 3.6: A planar four-bar linkage. Bar lengths are labeled as a_1, a_2, a_3 and a_4 (grounded). Input arm a_1 makes an angle α, and the output arm makes an angle β with the grounded bar a_4.

Substituting these values in Eq. 3.3 and solving for the solutions of the resulting quadratic equation, β can be found explicitly as a function of α and the parameters $a_1, a_2, a_3,\ a_4$.

$$\tan(\beta/2) \;=\; \frac{A \;\pm\; \sqrt{A^2 \;+\; B^2 \;+\; C^2}}{B \;+\; C}\,. \tag{3.4}$$

Thus, for one single value of α, two distinct solutions can be obtained which correspond to the two configurations in which a four bar linkage can exist. These two configurations are: *(i)* non self-intersecting, and *(ii)* self-intersecting. Ignoring the latter case, the relevant solution is:

$$\beta = 2\tan^{-1}\left(\frac{A \;+\; \sqrt{A^2 \;+\; B^2 \;+\; C^2}}{B \;+\; C}\right). \tag{3.5}$$

Relating the input angle α with the output angle β, Eq. 3.5 represents the *transmission function* of a four-bar linkage. The transmission functions of a parallelogram and a generic four-bar linkages are shown in Fig. 3.7.

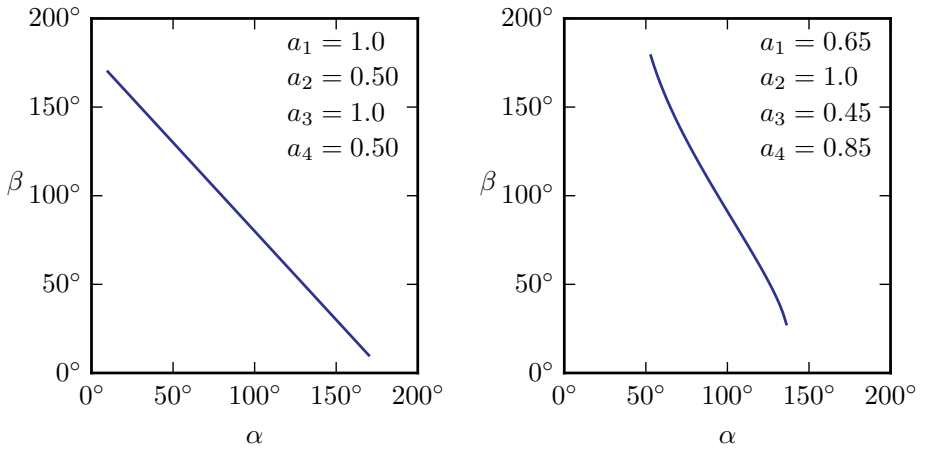

(a) **(b)**

Figure 3.7: The transmission function for (a) a parallelogram four-bar linkage is linear with slope -1, i.e. $\beta = \pi - \alpha$, and (b) a generic four-bar linkage is nonlinear. Bar lengths a_1, a_2, a_3 and a_4 are labeled inside the figures.

Loop condition – We will now utilize the transmission function to derive the loop condition to form a 3x3 mechanism. We refer back to the network shown in Fig. 3.5. For the linkage Λ_1, α_1 can be mapped to β_1 using the transmission function given by Eq. 3.5. Since,

$$\alpha_2 = 2\pi - \gamma_{12} - \delta_{12} - \beta_1 \,, \tag{3.6}$$

we also have a mapping between α_1 to α_2. Let's denote this mapping function that relates the input angle α_i of linkage Λ_i with the input angle α_{i+1} of linkage Λ_{i+1} (cyclic permutations understood) by $\boldsymbol{M}_{i,i+1}$, $i \in \{1,2,3,4\}$,

$$\alpha_2 = \boldsymbol{M}_{1,2}(\alpha_1) \,. \tag{3.7}$$

Extending the same argument to the remaining adjacent pair of linkages:

$$\alpha_3 = \boldsymbol{M}_{2,3}(\alpha_2) \quad \text{or} \quad \alpha_3 = \boldsymbol{M}_{2,3}(\boldsymbol{M}_{1,2}(\alpha_1)) \,, \tag{3.8}$$

$$\alpha_4 = \boldsymbol{M}_{3,4}(\alpha_3) \quad \text{or} \quad \alpha_4 = \boldsymbol{M}_{3,4}(\boldsymbol{M}_{2,3}(\boldsymbol{M}_{1,2}(\alpha_1))) \,. \tag{3.9}$$

The final circularly transported angle $\bar{\alpha_1}$ is given by:

$$\bar{\alpha_1} = \boldsymbol{M}_{4,1}(\alpha_4) \quad \text{or} \quad \bar{\alpha_1} = \boldsymbol{M}(\alpha_1), \tag{3.10}$$

where $\boldsymbol{M} = \boldsymbol{M}_{4,1}(\boldsymbol{M}_{3,4}(\boldsymbol{M}_{2,3}(\boldsymbol{M}_{1,2})))$

For an exact 3x3 mechanism, the mapping function $\boldsymbol{M}$ over α_1 should be an identity function. This precisely happens when every four-bar linkage Λ_i in Fig. 3.5 is a parallelogram linkage and the graph between β_i and α_i is linear with slope -1 $i \in \{1,2,3,4\}$ [Fig. 3.7(a)].

The non-linear input-output response of every linkage Λ_i in some generic 3x3 network may so 'adjust' themselves such that the final mapping function $\boldsymbol{M}$ is extremely close to an identity function, leading to an approximate mechanism and indeed this is the mathematical motivation behind the search for optimal design of perfect or near-perfect mechanisms. Thus, by generic flexible systems, we refer to those systems where all the internal four-bar linkages are not simultaneously parallelograms.

> Throughout the rest of the text, we mainly concern ourselves with systems of eight pin-jointed polygons forming a mechanism and therefore simply use the word *mechanism* while referring to these systems.

3.3 Numerical Model

In this section, we present the precise implementation of a numerical model based on the principle of energy minimization that is suitable to obtain the $D(\theta)$ curve of an arbitrary mechanism. Mathematically, the problem is to connect all eight polygons $(P_1, P_2.....P_8)$ [Fig. 3.8] precisely at their corners for every θ configuration. To turn this into a numerically tractable optimization problem, we connect the polygons that share a connection with zero rest length linear springs. This ensures that zero energy states correspond to the configurations where the polygons are precisely connected at the corner tips. With this understanding, the problem is now reduced to finding the zero energy states of the spring-connected polygon system for different θ configurations.

We start with initial position of each polygon in the 2D plane. From this high energy state, the springs are allowed to relax which can result in either of the two scenarios: *(i)* the system relaxes to a numerically zero energy value implying that such a system forms a mechanism, *(ii)* or else, the system

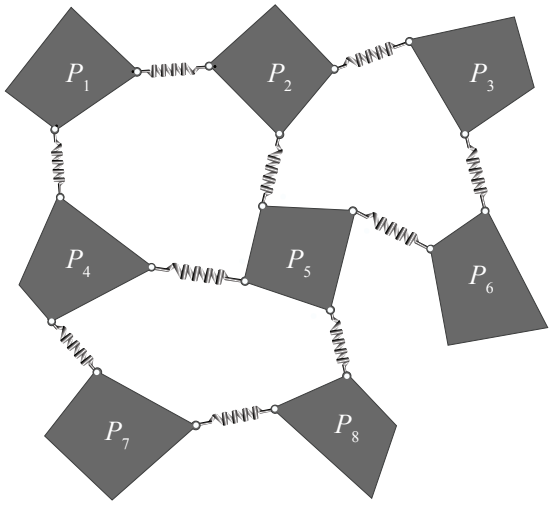

Figure 3.8: A system of eight polygons (labeled $P_1, P_2 ... P_8$) connected with linear springs of zero rest length in such a manner that if able to relax to a zero energy state, we end up with a system of eight polygons (similar to Fig. 3.3(c)) that are precisely connected at their corners.

relaxes to a non-zero finite energy value implying that such a system cannot form a mechanism. Given the total elastic energy stored in the springs as a function of position and orientation of each polygon, gradient based methods like *Steepest Descent*, *Conjugate Gradient (CG)*, *LBFGS* etc. can be employed to solve for the stable configuration of the system [92, 93]. We use a nonlinear CG method, specifically the version suggested by Flethcher-Reeves with Newton Raphson line search modification [94]. The details of the numerical model are presented in the following subsections.

3.3.1 Energy Functional

The position and orientation of a polygon are specified through three independent parameters:
- x: x-coordinate of the centroid of the polygon.
- y: y-coordinate of the centroid of the polygon.
- ϕ: orientation of the polygon measured *w.r.t.* the positive x-axis.

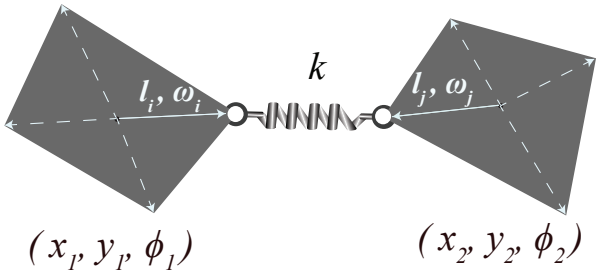

Figure 3.9: Two polygons sharing a spring connection k of zero rest length. (x, y, ϕ) denotes the centroid position and orientation of a polygon *w.r.t.* the positive x-axis. i^{th} corner of a polygon is parameterized through a vector of length l_i emanating from the centroid and making an angle ω_i *w.r.t.* the positive x-axis. The i^{th} corner of the first polygon is connected to the j^{th} corner of the second polygon.

Shape parameterization – The shape of a polygon is completely parameterized by four vectors emerging from the centroid. The polygon is constructed by joining the outer tip of these vectors. Each of the four vectors have a length l_i and oriented at ω_i w.r.t. the positive x-axis, $i \in \{1, 2, 3, 4\}$. In Fig. 3.9, we show two polygons sharing a connection k. The position and orientation of the first polygon are defined by the tuple (x_1, y_1, ϕ_1) while that of the second polygon are defined by (x_2, y_2, ϕ_2). The i^{th} corners of the first polygon is connected to the j^{th} corner of the second polygon. The corners involved in the connection belong to the tip of the vectors (l_i, ω_i) and (l_j, ω_j) of the respective polygons. Elastic energy stored in the linear spring k can be expressed as:

$$E_k = ((x_1 + l_i \cos(\phi_1 + \omega_i)) - (x_2 + l_j \cos(\phi_2 + \omega_j)))^2 +$$

$$((y_1 + l_i \sin(\phi_1 + \omega_i)) - (y_2 + l_j \sin(\phi_2 + \omega_j)))^2 \tag{3.11}$$

Given the position, orientation and shape information of each polygon, the total *energy functional*, $\boldsymbol{E}$ for the spring-connected system shown in Fig. 3.8 is given by:

$$\boldsymbol{E} = \sum_{k=1}^{10} E_k \tag{3.12}$$

3.3.2 Energy Minimization

To contain the complete information about the configuration of the system at any instant, we store the position and orientation of all the eight polygons in a single vector called *position vector*, $\boldsymbol{p}$. A more natural choice should have been $\boldsymbol{x}$, which is saved for some later use. $\boldsymbol{p}$ is given by:

$$\boldsymbol{p} = [x_1, y_1, \phi_1, x_2, y_2, \phi_2 .....x_8, y_8, \phi_8]^{\mathbf{T}} \tag{3.13}$$

where subscripts denote the polygon number [Fig. 3.8]. If a small change from $\boldsymbol{p}$ to $\boldsymbol{p}+\Delta\boldsymbol{p}$ changes the energy functional value from $\boldsymbol{E(p)}$ to $\boldsymbol{E}(\boldsymbol{p}+\Delta\boldsymbol{p})$, then through the second order Taylor expansion of $\boldsymbol{E}$ around $\boldsymbol{p}$, $\boldsymbol{E}(\boldsymbol{p}+\Delta\boldsymbol{p})$ can be expressed as:

$$\boldsymbol{E(p}+\Delta\boldsymbol{p}) = \boldsymbol{E}(\boldsymbol{p}) + \boldsymbol{J}|\Delta\boldsymbol{p} + \Delta\boldsymbol{p}^{\boldsymbol{T}}|\boldsymbol{H}|\Delta\boldsymbol{p} \tag{3.14}$$

where *w.r.t.* all 24 elements in $\boldsymbol{p}$, $\boldsymbol{J}$, the *Jacobian* is the first derivative vector and $\boldsymbol{H}$, the *Hessian* is the second order partial derivative matrix of the total energy functional $\boldsymbol{E}$. We want to find $\Delta\boldsymbol{p}$ such that $\boldsymbol{E}(\boldsymbol{p}+\Delta\boldsymbol{p})$ corresponds to the minima of $\boldsymbol{E}$. We seek to solve the equation that sets the derivative of $\boldsymbol{E}(\boldsymbol{p}+\Delta\boldsymbol{p})$ *w.r.t.* $\Delta\boldsymbol{p}$ to zero:

$$\frac{d}{d\Delta p}\left(\boldsymbol{E}(\boldsymbol{p}) + \boldsymbol{J}|\Delta\boldsymbol{p} + \Delta\boldsymbol{p}^{\boldsymbol{T}}|\boldsymbol{H}|\Delta\boldsymbol{p}\right) = 0 \tag{3.15}$$

We get:

$$\boldsymbol{H}|\Delta\boldsymbol{p} = -\boldsymbol{J}(\boldsymbol{p}) \tag{3.16}$$

Eq. 3.16 represents a set of 24 nonlinear equations, which we solve using the nonlinear Conjugate Gradient (CG) method, the main reason being that CG is well suited for problems where $\boldsymbol{H}$ is a sparse matrix and requires fairly small storage requirements [94]. Although, the performance may vary, other gradient based methods are also expected to work. The detailed working and pseudocode of the algorithm that we implemented can be found elsewhere [94].

CG convergence and the cutoff value of $\boldsymbol{E}$ – As pointed out earlier, depending upon the polygonal shapes, the system shown in Fig. 3.8 can or cannot relax to a mechanism. This can be understood more intuitively

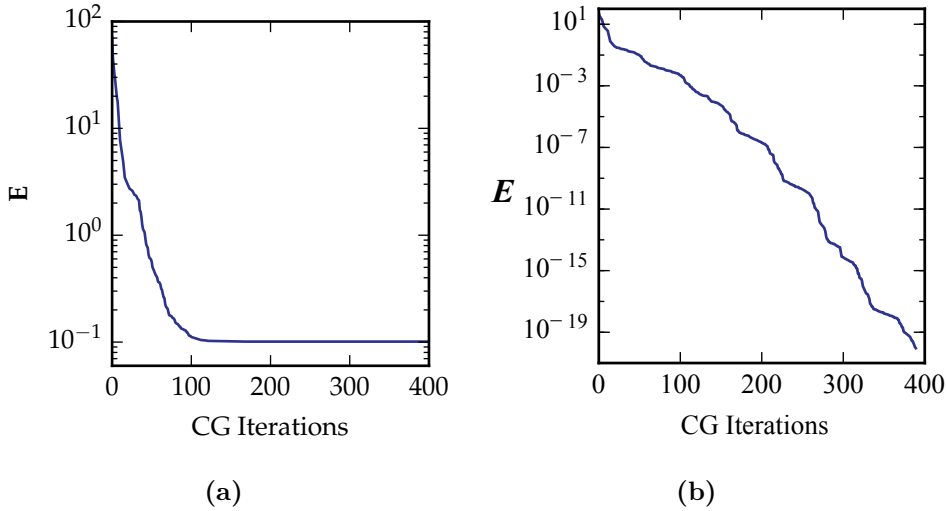

Figure 3.10: Conjugate Gradient (CG) convergence curve of a eight-polygon spring connected system [Fig. 3.8] that: (a) relaxes to a finite energy state and (b) relaxes to a zero energy state and forms a mechanism, at least in the vicinity of the relaxed state.

through an extreme case where the sizes of the polygons are so disproportionate that they do not 'fit in' together. In Fig. 3.10, we plot the convergence curve of CG algorithm i.e. the value of $\boldsymbol{E}$ versus each iteration step of CG for two different systems. The final value of $\boldsymbol{E}$ indicates that the system for which the convergence curve is shown in Fig. 3.10(a) equilibrates to a finite energy whereas the one corresponding to Fig. 3.10(b) equilibrates to numerically zero energy value, thus forming a mechanism at least in the vicinity of the relaxed state.

In Fig. 3.11, through a histogram plot, we summarize the final value of $\boldsymbol{E}$ for 10^4 randomly generated/relaxed systems. There are two distinct clusters of $\boldsymbol{E}$ with the left one corresponding to the equilibrated systems while the right one to the systems that could not. The correspondence between the final value of $\boldsymbol{E}$ and whether or not the system relaxes to a mechanism is utilized to save considerable computational power. We set the cutoff value of $\boldsymbol{E}$ to be 10^{-10}, below which CG is terminated as the system is assumed to be practically at zero energy state.

Generating a $D(\theta)$ curve appears straightforward now: relax a system

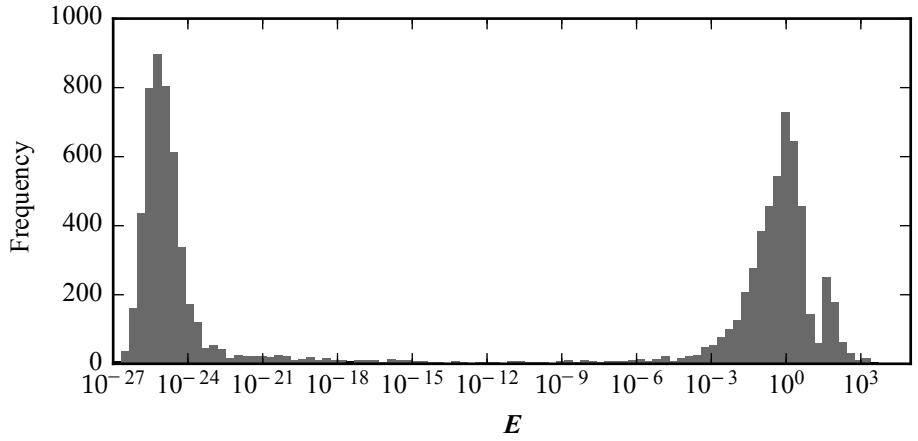

Figure 3.11: Distribution of the final value of $\boldsymbol{E}$ for 10^4 randomly generated/relaxed spring-connected eight-polygon systems [Fig. 3.8]. The left and the right clusters represent systems that relax to a zero energy state and a finite energy state respectively. The two well separated clusters allow to set a cutoff value of $\boldsymbol{E}$, below which the system can be assumed to be at practically the zero-energy state and in which case CG can be terminated. This saves a considerable amount of computational power. We set the cutoff value of $\boldsymbol{E}$ to be at 10^{-10}.

of spring-connected polygons over fixed predetermined θ configurations and measure D. This is stated more clearly in the §3.4.1, where we present a precise definition of θ as well.

3.4 Design Problem Formulation

Complex design problems where the relationship between the *design variables* and the *target functionality* is non-trivial and difficult to construct or approximate can be solved by following a numerical optimization methodology. First one constructs an *objective function* in terms of the design variables, along with imposing the *constraints* to avoid *unfeasible designs*. The objective function quantifies the proximity of a system to the desired functionality. Then, depending on the type of the problem, the objective function is minimized or maximized to find the optimal values of the design

variables. Here, we focus on a mechanism formed by the eight pin-jointed polygons and optimize for a constant target curve $D_t(\theta)$.

In this section, we formulate the design optimization problem, the final purpose of which is to arrive upon a clear definition of the design variables and the objective function that includes *constraint handling* as well. We start with identifying the relevant design variables and present the objective function for the unconstrained optimization. To handle unfeasible designs (such as a system of self-intersecting polygons), we then establish the necessary *constraints* and describe the method to handle them. Finally, we present the *augmented objective function* for constrained optimization.

3.4.1 Design Variables

Design variables are numerical parameters in terms of which the design is specified. During the optimization, design variables change and influence the objective function value. Determining the optimal values of the design variables is the principle aim in design optimization as their optimal values correspond to the optimal design.

Removing the redundant design variables – According to the notation introduced in §3.3.1, while writing the energy functional of the spring-coupled polygon system, we required the values of 11 variables i.e. x, y, ϕ, l_1, ω_1, l_2, ω_2, l_3, ω_3, l_4, ω_4 to completely specify the position and orientation of one single polygon. Thus, it may appear that the total number of design variables for the current problem is 11x8=88. However, a simplified representation of the mechanism, shown in Fig. 3.12(b) illustrates that only the positioning of twelve points in the 2D plane are sufficient to construct any arbitrary system of eight pin-jointed polygons. These twelve points are essentially the connecting pin-joints. By removing the redundant vertices, the alternate representation simplifies the task to only find out the optimal positioning of twelve points in the 2D plane in order to match the target curve $D_t(\theta)$. These points are labeled as $A, B...L$. Note that for the calculation of the Jacobian $\boldsymbol{J}$ and Hessian $\boldsymbol{H}$, we map the coordinates of the simplified notation back to the shape parameterization given by the 88 variables. Given the positioning of the 12 points, this is not so difficult, for example the rod labeled P_1 in Fig. 3.12(b) can be seen as a four-sided polygon with 'overlapping' two pairs of vertices, and so on.

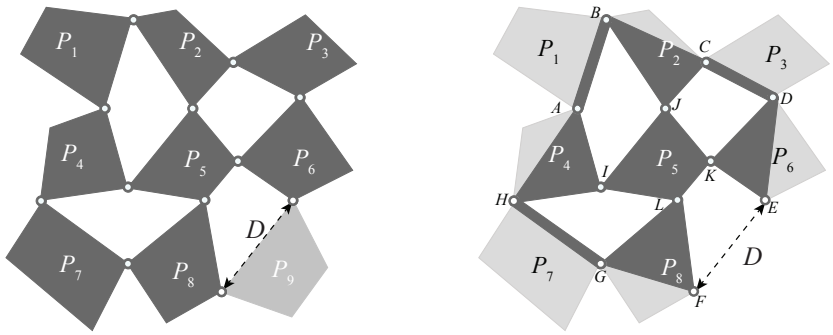

Figure 3.12: Redundant polygonal vertices in (a), which have no effect on the resulting $D(\theta)$ curve removed in (b). Such a formulation helps to reduce the design problem to essentially optimizing for the position of the twelve connecting pin-joints labeled $A, B.....K$ in order to match the target curve $D_t(\theta)$.

While formulating an optimization problem, from the computational points of view, it is immensely important to remove the redundant design variables and find the most precise parameterization of the design. A presence of large number of redundant variables can lead to a difficulty in convergence towards an optimal solution due to the search algorithm's tendency to get stuck in a region where the change in the value of the variables has no effect on the value of the objective function. The new representation produces a compact, lower-dimensional and numerically effective encoding of the problem which now only requires to optimize the value of 12x2=24 design variables.

Measurement of the angle $\boldsymbol{\theta}$ – At this stage, we are in a suitable position to describe the method chosen to measure θ. We remind that θ measures the amount of internal deformation of a mechanism (§3.1). Imagine a mechanism constructed from randomly positioned 12 points in the 2D plane. For simplicity, assume the mechanism to be without any self-intersections. From this *undeformed configuration* of the mechanism, we can back-construct the shape information of every polygon. For convenience, one can presume the polygons in their current orientation to be unrotated i.e. set the parameters $\phi_1, \phi_2 ... \phi_8$ to zero. θ is set to 0^o at this *neutral*

configuration. The hinging motion is then mimicked by relaxing the system over desired θ configurations, throughout which the central polygon P_5 is always kept from rotation and translation, as if 'nailed' into the 2D plane. Numerically, this is achieved by always explicitly setting (x_5, y_5, ϕ_5) in the position vector $\boldsymbol{p}$ to their initial values and fixing all their related derivatives in the $\boldsymbol{H}$ and $\boldsymbol{J}$ to zero, thereby preventing them from adjusting during the CG convergence procedure.

Now we are able to vary θ and actuate the mechanism. The most natural way to do so is to rotate polygon P_2 around the pin-joint connecting it with the polygon P_5, numerically which is achieved by explicitly specifying ϕ_2 and once again fixing all the derivatives related to it in $\boldsymbol{H}$ and $\boldsymbol{J}$ to zero. Forced to relax in this configuration, the remaining six polygons adjust their positions and orientations accordingly. Following this procedure, we determine $D(\theta)$ for θ ranging from -60° to 60°, with the total motion discretized into $N = 20$ steps; θ takes on values -60°, -54°. . . .0°, 0°. . . .54°, 60°. At each of these steps, D is recorded once the system relaxes, yielding a discretized version of the $D(\theta)$ curve[4]. Fig. 3.13 demonstrates the procedure in a flowchart form.

3.4.2 Objective Function and Constraint Handling

The Objective function is a measure to decide how good or how bad a candidate solution is depending on the distance of its $D(\theta)$ curve from the target curve $D_t(\theta)$. The objective function used here is a combination of two parts. The first part computes the position error as the mean of the square of the Euclidean distances between each D_t^i and the corresponding D_c^i where:
- $\{D_t^i\}$ is a set of points on $D_t(\theta)$ which should be met by the optimal mechanism. $i \in 1, 2...20$. D_t^i can be written in a Cartesian orthogonal coordinate system Oxy as:

$$D_t^i = \left[D_{xt}^i, D_{yt}^i\right]^T, \tag{3.17}$$

[4]We follow a slightly indirect protocol to deform a mechanism! We begin from neutral state, $\theta = 0°$ and on either sides, use the final relaxed state of the previous θ step as the initial condition for the next θ step. This is done to remain computationally economic. CG converges within lesser iterations if the desired final configuration and initial configuration are 'adjacent'.

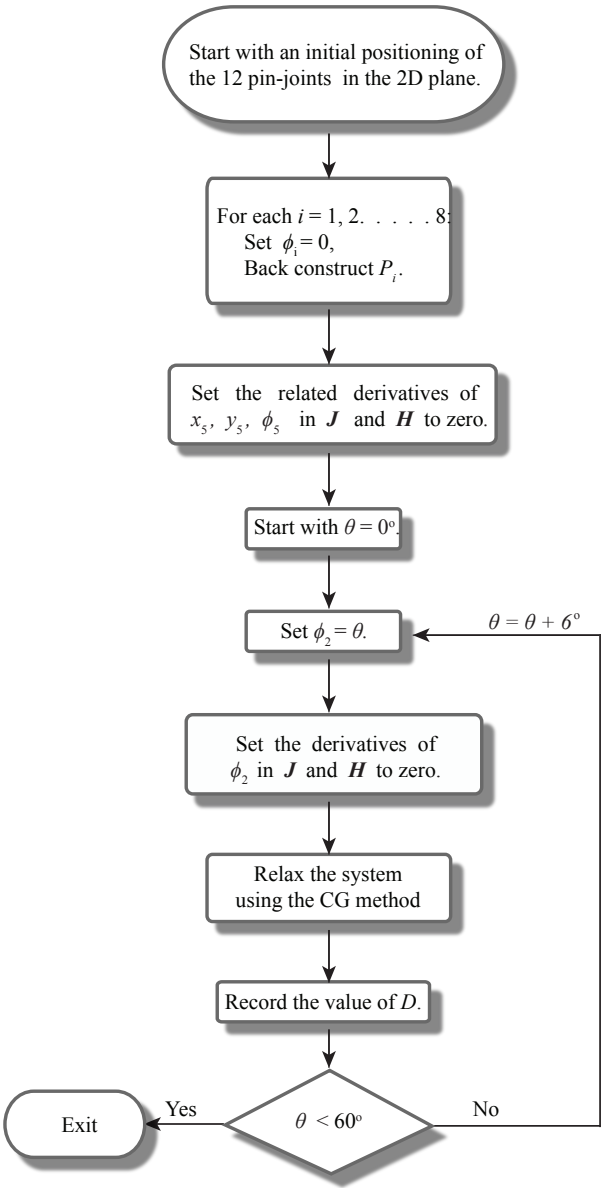

Figure 3.13: A flowchart depicting the numerical procedure to obtain a discretized version of the $D(\theta)$ curve of a mechanism.

where D^i_{xt} and D^i_{yt} are respectively the x and y components of D^i_t.
- $\{D^i_c\}$ is the set of points on the $D(\theta)$ curve of a candidate mechanism for a set of values of θ. Expressing D^i_c in the Cartesian coordinate system:

$$D^i_c = \left[D^i_{xc}, D^i_{yc}\right]^T. \tag{3.18}$$

Accordingly, the first part of the objective function, $\boldsymbol{g}$ can be expressed as:

$$\boldsymbol{g} = \frac{1}{N}\sum_{i=1}^{N}\left[(D^i_{xt} - D^i_{xc})^2 + (D^i_{yt} - D^i_{yc})^2\right], \tag{3.19}$$

where N is the number of points on the $D(\theta)$ curve to be synthesized, and is set to 20 in the present study. Clearly, lower the value of $\boldsymbol{g}$, the better is the solution quality.

Constraints to avoid unfeasible designs – One must expect optimal solutions to deform as a mechanism for the entire range of θ, however this can not be ensured, as we may and in fact will encounter systems that do not equilibrate to zero energies for all the θ configurations. Therefore, to avoid any confusion, we will not use the term mechanism while discussing the constraints below, and instead use a much more general term *system* by which we mean an equilibrated spring-coupled polygonal system, although for simplicity in the terminology, in the later sections, we will be a little less strict in this regard.

For our purposes, we require to impose constraints to avoid encountering those systems during the search that can not be realized in the real-world (we in fact have already hinted at one). Such systems lead to an unfeasible design. We identify the following three types of undesirable systems: *(i)* systems that do not equilibrate to a mechanism, *(ii)* systems that contain self-intersection within or among polygons, and *(iii)* systems with disproportionate polygonal size, i.e. unworkable edge length of polygons. An example for each of these systems is shown in Fig. 3.14 (a-c). In an unfeasible design, these cases can appear both separately or together. Below, we establish the constraints to avoid each of these cases and present the method adopted to quantify their violation:

Constraint $\boldsymbol{\Gamma_1}$ – The first constraint is imposed to avoid systems that do not equilibrate to a mechanism [Fig. 3.14(a)], the violation of which

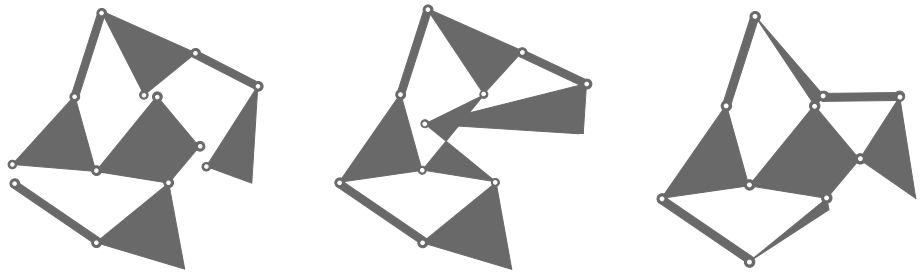

(a) (b) (c)

Figure 3.14: Examples of unfeasible designs. (a) non-equilibrating system, (b) self-intersecting system, and (c) system with disproportionate polygon size.

requires to be checked at every θ step. The measure of its violation on the i^{th} step is given by p_i. We constructed the following *ramp function* to quantify p_i:

$p_i =$	$\boldsymbol{E}_i$
$(\log_{10} \boldsymbol{E}_i)/10 + 1$	$\boldsymbol{E}_i \geq 10^{-10}$
0	$\boldsymbol{E}_i < 10^{-10}$

where for the i^{th} θ step, $\boldsymbol{E}_i$ is the final energy functional value the system relaxes to [Eq. (3.12)]. This relationship is consistent with the previous assumption that all the values of $\boldsymbol{E} < 10^{-10}$ are assumed to be numerically zero, thereby inherently implying that the system equilibrates to zero energy and abides by the current constraint i.e. $p_i = 0$. Systems that equilibrate to finite energy have $p_i > 0$. The total violation is denoted by $\boldsymbol{p}$ and is calculated by summing over all the θ steps:

$$\boldsymbol{p} = \sum_{i=1}^{20} p_i. \tag{3.20}$$

Constraint $\boldsymbol{\Gamma_2}$ – During optimization, the design variables are free to change values which may result in *self-intersecting* systems [Fig. 3.14(b)]. To detect and avoid these systems, we impose another constraint. Identifying

self-intersecting systems is not straightforward and we now show how we implemented it. Through an example of a perfect system, shown in Fig. 3.12(b), three distinct closed polygons shall first be identified: *(i)* outermost polygon *ABCDEFGH*, denoted by P_o, *(ii)* intermediate 'windmill-shaped' polygon *ABICDJEFKGHL*, P_w and *(iii)* innermost polygon *IJKL*, P_i . The necessary and sufficient conditions to guarantee a non self-intersecting system are: *(i)* P_i is 'contained within' P_o, and *(ii)* all three P_o, P_w and P_i are simple and do not self-intersect individually. A system not satisfying any of these two conditions will inevitably display self-intersection.

Similar to the previous constraint, we need to check for the violation of the present constraint for every θ step. Its value at the i^{th} θ step is denoted by q_i. A simple binary quantification for q_i is implemented, where it is assigned a value 1 if self-intersection occurs and 0 otherwise.

$q_i =$	Self Intersection
1	Yes
0	No

The total violation for the complete range of θ is given by $\boldsymbol{q}$:

$$\boldsymbol{q} = \sum_{i=1}^{20} q_i. \tag{3.21}$$

It is important to note that q_i can only be calculated if $p_i = 0$. For $p_i \neq 0$, q_i is simply assumed to be zero.

Constraint $\boldsymbol{\Gamma_3}$ – We have observed that binary penalization of self-intersection increases the chances of systems that have disproportionate polygonal size [Fig. 3.14(c)]. This happens due to the sharp constraint boundary. In order to avoid such systems, we impose the final constraint whose aim is to keep every edge length of every polygon within a desired range. It is quantified using a dynamic method, where for every edge we specify a minimum edge length: l_{min} and a maximum edge length: l_{max}. We set l_{min} at 0.5 and l_{max} at 2.5. These choices are based to keep the polygonal edge lengths within a reasonable limit. Note that we do not need to check for the violation of this constraint and at every θ step and thus we employ the subscript i for another purpose. The violation for the i^{th}

edge length is given by s_i. Because there are a total of 20 edges, i $\in$ {1, 2 . . . 20}. For an edge with edge length l, the following relationship is constructed to quantify r_i:

$r_i =$	Edge Length, l
$0.05(1 - 0.5l)$	$0 \leq l < 0.5$
0	$0.5 \leq l < 2.5$
$0.025(1 - 0.5l)$	$2.5 \leq l < 3.0$
0.05	$l \geq 3.0$

The total violation, $\boldsymbol{r}$ is summed for all the θ steps, and is given by:

$$\boldsymbol{r} = 20 \sum_{i=1}^{20} r_i. \tag{3.22}$$

The functions constructed to measure the violation of the above mentioned constraints are not unique, and in fact other suitable choices can also lead to satisfactory results. We justify our choices solely on the basis of making the scales of $\boldsymbol{p}$, $\boldsymbol{q}$ and $\boldsymbol{r}$ similar. The minimum value that $\boldsymbol{p}$, $\boldsymbol{q}$ and $\boldsymbol{r}$ can attain is zero. The maximum value of $\boldsymbol{p}$, $\boldsymbol{q}$ and $\boldsymbol{r}$ is 20. Hence, we ensure that the values are on a similar scale. This is important because a substantial difference in the magnitudes can lead to an undue imbalance on the search process where satisfying one constraint can be favored over others. A *feasible solution* should satisfy all the three constraints $\Gamma_1, \Gamma_2, \Gamma_3$ and thus these constraints together form the boundary of the *feasible region*. Solutions lying inside the feasible region, will have $\boldsymbol{p} = \boldsymbol{q} = \boldsymbol{r} = 0$.

Penalized objective function – Constraints Γ_1, Γ_2 and Γ_3 form the second part of the objective function. Since, we are solving a minimization problem, violation of these constraints i.e. $\boldsymbol{p}$, $\boldsymbol{q}$ and $\boldsymbol{r}$ are added with the original objective function, $\boldsymbol{g}$ as extra *penalty terms*. This ensures that a solution violating any of the assigned constraints will have higher objective function value than the one that does not. The augmented objective function, $\boldsymbol{f}$ is given by:

$$\boldsymbol{f} = \boldsymbol{g} + \boldsymbol{p} + \boldsymbol{q} + \boldsymbol{r}. \tag{3.23}$$

We now have a complete understanding of the objective function that takes care of the constraints as well. Next, we optimize for the values of design variables such that $\boldsymbol{f}$ is minimized to match the given target $D_t(\theta)$ curve.

3.5 Particle Swarm Optimization and Implementation Details

For complex design optimization problems, the global landscape of the objective function is rugged, multi-modal and patchy, where feasible regions are separated by unfeasible regions in the design variable space. The landscape becomes more complex as the dimensionality of the problem increases. Gradient-based methods terminate at local optimum and unless the objective function consists of only one optimum, will therefore converge to a local optimum. In such problems, we therefore need gradient-free search algorithms that possess a global search capability.

Optimization problems where one can numerically obtains the influence of the decision variables on the value of the objective function, even in the absence of some analytic algebraic model of the system are well suited to be solved through gradient-free population based optimization metaheuristic techniques, popularly known as evolutionary algorithms [55]. The search procedure of these algorithms uses mechanisms inspired by biological evolution, such as reproduction (cooperation), mutation, recombination and selection (competition). One begins with an initial pool of guess solutions. This pool of solutions is referred as *population* and the *population size* indicates the number of candidate solutions in the population. Based on the algorithmic rules, the population members explore the search space and evolve through *generations* by exchanging information between fellow members. With an appropriate implementation, one can expect the population members to converge towards the region where the mean value of the objective function is low (for a minimization problem). The standard terms for the objective function value are: *cost* for a minimization problem and *fitness* for a maximization problem. However, we would simply mention it by the *objective function value*. Convergence of the population towards an extremely low mean objective function value suggests that the algorithm approaches or approximates the global optimum. Specifically, from the perspective of a design optimization problem, this would mean that the algorithm has managed to discover an optimal design.

3.5.1 Particle Swarm Optimization (PSO)

PSO – For our purpose, we utilize an algorithm that simulates swarm behavior: Particle Swarm Optimization (PSO). PSO is a nature-inspired population based search algorithm that is originally accredited to Eberhart, Kennedy and Shi [60, 90, 91]. The algorithm mimics the social behavior of birds flocking and fishes schooling. It starts with an initial population of randomly distributed potential solutions, which are given the name *particles*. Each individual particle occupies a particular *position* and is also initialized with some random *velocity* in the hyper-dimensional search space. Based on the quality measure (objective function value), the algorithm aims to improve the solutions. The particles 'fly' through the search space by means of a set of mathematical expressions. In the standard form of the PSO, these mathematical expressions indicate the balanced movement of each particle towards the best position discovered by that particle individually and by the best position discovered by the swarm so far. Stochasticity is induced into these mathematical expressions to ensure a wide exploration of the search space. Below we explain the governing equations of PSO.

Position and velocity update equations – Let us assume a high dimensional search space. The position and velocity of a particle i is initialized by the vector x_i and v_i respectively [5]. $x_{i,j}$ and $v_{i,j}$ are the position and velocity of the particle in the j^{th} dimension. In our case x_i and v_i are 24 dimensional vectors i.e. j=24. During the search, each particle is attracted towards its best location achieved so far, $xbest_i$ and by the best location discovered by the swarm so far across the whole population, $xgbest$. The simplest update rule for velocity that one can construct is:

$$v_{i,j}^{k+1} = v_{i,j}^{k} + (xbest_{i,j}^{k} - x_{i,j}^{k}) + (xgbest_{j}^{k} - x_{i,j}^{k}), \tag{3.24}$$

where k denotes the generation number. The update rule for position is:

$$x_{i,j}^{k+1} = x_{i,j}^{k} + v_{i,j}^{k+1}. \tag{3.25}$$

The schematic movement of a particle based on Eq. 3.25 is shown in Fig. 3.15. The search process is however, entirely deterministic. To include stochasticity into the search process, the second and the third terms in Eq.

[5] We are using the usual notation of PSO, which should not be confused with the notation x_i used in the §3.3.2 to denote the x-coordinate of the centroid of a polygon P_i.

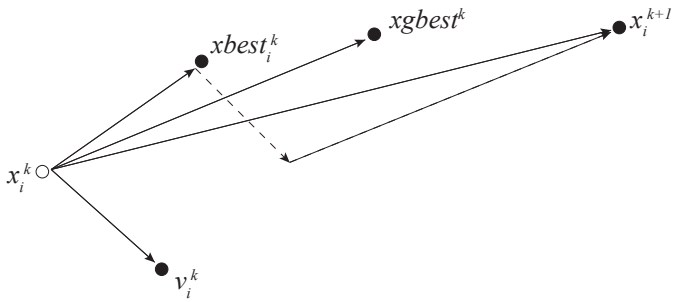

Figure 3.15: Schematic movement of a particle in PSO based on the Eq. 3.24 and 3.25. x_i^k (v_i^k) denotes the position (velocity) of particle i at the generation k. $xbest_i^k$ ($xgbest^k$) denotes the best position found by the i^{th} particle (entire swarm) till the generation k.

3.24 are multiplied with r_1 and r_2 - j dimensional vectors whose elements are random numbers distributed uniformly between 0 and 1. The equation becomes:

$$v_{i,j}^{k+1} = v_{i,j}^k + r_1(xbest_{i,j}^k - x_{i,j}^k) + r_2(xgbest_j^k - x_{i,j}^k). \tag{3.26}$$

Cognition and social parameters, c_1 and c_2 – Along with this, the second and the third terms are also multiplied with the parameters c_1 and c_2 respectively. c_1 and c_2 are two parameters representing the particles confidence in itself (*cognition*) and in the swarm (*social*) respectively. These two parameters are among the most important parameters in the algorithm in that they control the balance between *exploration* and *exploitation*. A relatively high value of c_1 will attract the particles towards their local best experiences while higher values of c_2 will attract them towards the swarm leader. The equation thus becomes:

$$v_{i,j}^{k+1} = v_{i,j}^k + c_1 r_1(xbest_{i,j}^k - x_{i,j}^k) + c_2 r_2(xgbest_j^k - x_{i,j}^k). \tag{3.27}$$

Inertial weight, w – Let us further dissect Eq. 3.27 to gain a better intuition of the algorithm. Without the second and the third parts, the particles will independently keep on flying at the current velocity in the

same initially assigned direction. PSO will not find an acceptable solution unless there is one on their flying trajectories, which is rare. Without the first part, movement of particles becomes memoryless. A particle which has the global best position will be flying at a zero velocity. All other particles will be attracted towards this particle until another particle takes over the global best position. Therefore, it can be imagined that without the first part, the search space shrinks through the generations and the method then resembles a local search algorithm. On the other hand, by adding the first part, the particles have a tendency to expand their search space, that is, they have the ability to explore the new areas. So, more global search ability is expected by including the first part. Shi added another parameter to the equation, an inertia weight w [91].

$$v_{i,j}^{k+1} = wv_{i,j}^{k} + c_1 r_1 (xbest_{i,j}^{k} - x_{i,j}^{k}) + c_2 r_2 (xgbest_{j}^{k} - x_{i,j}^{k}). \tag{3.28}$$

w can be a positive constant or even a positive linear or nonlinear function of generations [95, 96]. Eq. 3.28 represents mathematically the velocity update equation of the PSO in its standard form. In the literature, an abundance of different variants of PSO can be found, but for our purposes, we will adhere to the standard PSO described here, where the velocity update rule is given by Eq. 3.28 and the position update rule is given by Eq. 3.25.

PSO Notations – We will now define some notations. The objective function value of the i^{th} particle at the k^{th} generation is given by $\boldsymbol{f}(x_i^k)$. We introduce a simple rule to write down useful notations compactly: a combination of bracket(s) and the immediate subscript(s) is used to denote an operation eg. $< a >_b$ denotes obtaining the mean of a quantity a over the objects b and similarly through the use of square brackets, $[a]_b$ denotes obtaining the best value of a quantity a over the objects b. Using this notation: *(i)* individually the best position found by the i^{th} particle till the k^{th} generation is given by $[x_i^k]_k$, *(ii)* the objective function value corresponding to $[x_i^k]_k$ is given by $[\boldsymbol{f}(x_i^k)]_k$, *(iii)* globally the best position found by the entire swarm till the k^{th} generation is given by $[x_i^k]_{i,k}$, and *(iv)* the objective function value corresponding to $[x_i^k]_{i,k}$ is given by $[\boldsymbol{f}(x_i^k)]_{i,k}$.

Through a flowchart, we present the complete functioning of PSO in Fig. 3.16. PSO begins with initializing x_i and v_i for each particle i. After initialization, we set $[x_i^k]_k$ to x_i^k and $[\boldsymbol{f}(x_i^k)]_k$ to $\boldsymbol{f}(x_i^k)$ for each particle i. Thereafter, we find the global best position i.e., the position of the swarm

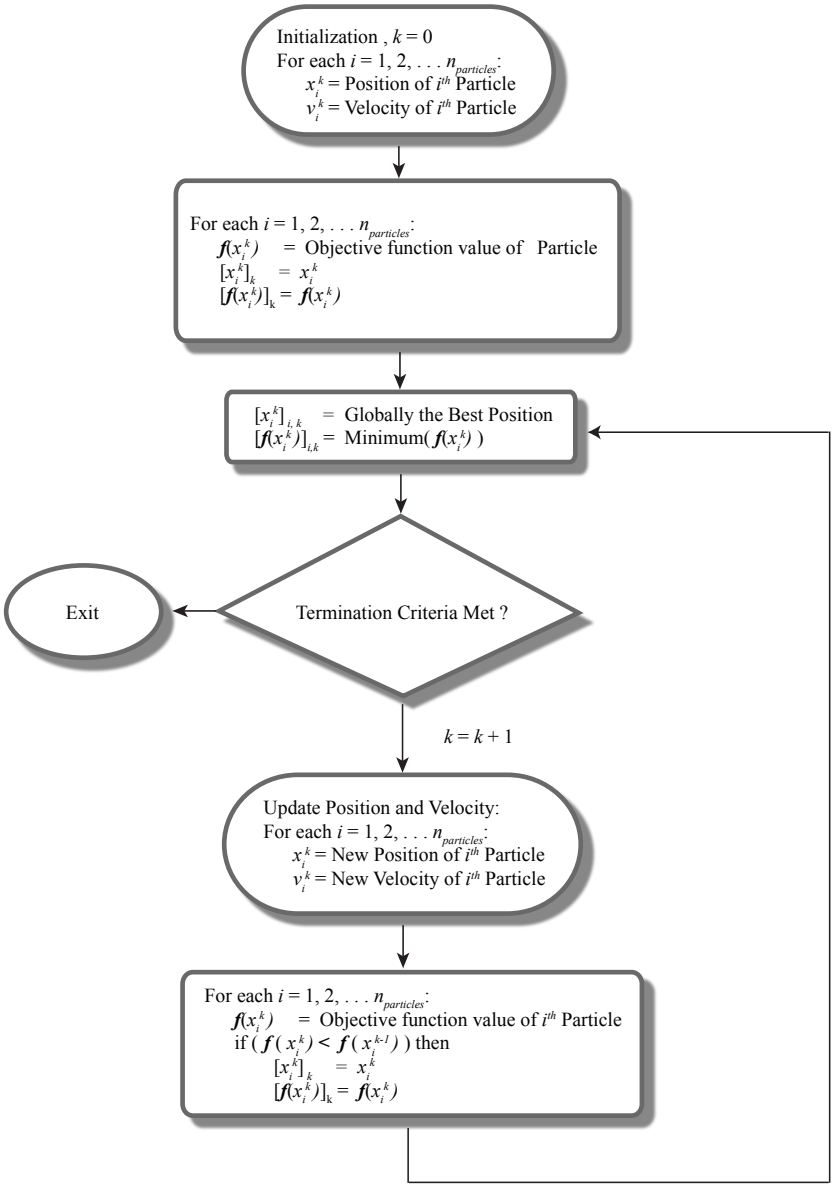

Figure 3.16: Particle swarm optimization depicted in a flowchart form.

leader $[x_i^k]_{i,k}$ and its objective function value $[\boldsymbol{f}(x_i^k)]_{i,k}$. After finding these values, x_i and v_i are updated according to the 3.25 and Eq. 3.28 respectively. With the new position and velocity, $[x_i^k]_k$, $[\boldsymbol{f}(x_i^k)]_k$, $[x_i^k]_{i,k}$ and $[\boldsymbol{f}(x_i^k)]_{i,k}$ are updated if required and the next round of position and velocity update is performed. This is repeated till some termination criteria is satisfied. We discuss our method for terminating PSO in §3.5.2.

3.5.2 Implementation of PSO

In this section, we cover the swarm initialization and other PSO implementation details that include: *(i)* position initialization of the particles, *(ii)* velocity initialization of the particles, *(iii)* the swarm size, *(iv)* the termination criteria, and *(v)* the target curve.

Position initialization – The search procedure begins by initializing the position of the particles in the search space. The particles should be spread as uniformly as possible. A poor initialization of the swarm, covering the search area inefficiently, may lead to an inability to explore the potential regions thereby missing many of the potentially good solutions. A number of methods have been suggested in the literature to initialize the position of the particles. The usual method is by drawing a uniformly distributed random number along each dimension in the problem space. In many other simple variations, the initial distribution of random numbers is changed from the uniform distribution to other probability distribution like exponential, lognormal and Gaussian distributions [97, 98].

To generate a particle, we first begin with a placement of 12 vertices in the 2D plane (marked by filled red markers in Fig. 3.17(a). As it can be seen that this setting leads to the most simplest mechanism that consists of rotating squares. The mechanism is shown in dark gray color and it is similar to the one previously shown in Fig. 3.2(a). The diagonal length of the square is 1.5. Later, we will provide the constant target function $D_t(\theta)$: $D = 1.0$. Thus, these 12 points are chosen to be placed at a distance such that the initial population is practical for the given target function.

A generic mechanism is now constructed by perturbing this *precursor mechanism* in each of the 24 dimensions by random magnitudes. This is achieved by adding a randomly generated number that's distributed uniformly between (-0.50, 0.50) in each of the 24 dimensions. Fig. 3.17(a) shows this schematically. The perturbed mechanism is shown in the color light

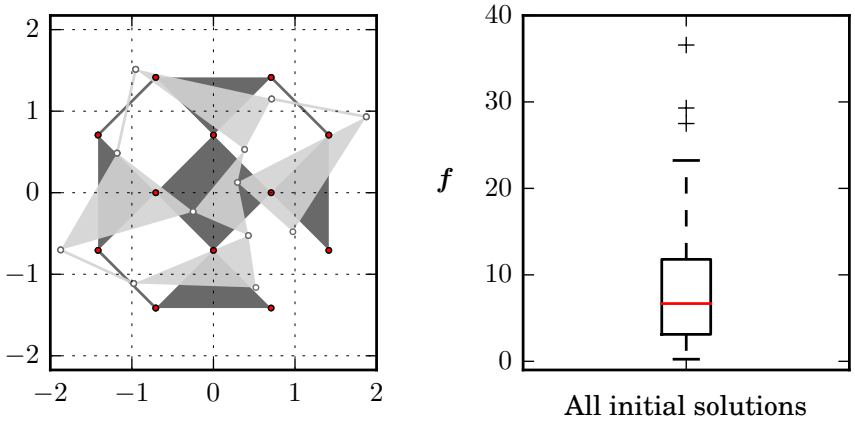

(a) (b)

Figure 3.17: (a) Schematic diagram demonstrating the generation of the initial population. We perturb the mechanism shown in the dark gray with random numbers to obtain the generic mechanism shown in light gray. (b) A box-plot summarizing the objective function value $\boldsymbol{f}$ of the initial population with the population size $n_{particles} = 50$ for target curve $D_t(\theta) = 1.0$.

gray. Random numbers are generated within this range so as to maintain as much diversity among the different mechanisms as possible. However, this may also lead to self-intersection and disproportionate polygonal size (violating constraints Γ_2 and Γ_3, see §3.4.2), to check which, all the particles are repeatedly initialized until they satisfy these two constraints. This ensures that the swarm does not dissipates its diversity in the unfeasible search space.

Velocity initialization – The second part of the initialization involves imparting random velocities to particles. We initialize the velocity in each dimension by a random number uniformly distributed between 0 and 1. Initializing with low velocity values works well as it ensures that the particles do not leave the search space.

Swarm size – Swarm size refers to the total number of particles in the swarm. Selecting a correct swarm size is important as it controls the

exhaustive exploration of search space, and is highly problem dependent. A smaller swarm is incapable to explore the search space effectively and a larger swarm leads to a problem in convergence along with being computationally expensive. To find an optimal swarm size, one can start from a relatively few particles and increase the number until one finds the swarm size that works best. We select a swarm of fixed size 50 i.e $n_{particles} = 50$. Through a box-plot shown in Fig. 3.17(b), we summarize the initial objective function values, $\boldsymbol{f}$ of the 50 particles for target curve $D_t(\theta) = 1.0$.

Termination criteria – A termination criteria marks the end of a PSO run. The commonly used criteria are to terminate when the algorithm has exceeded a maximum number of generations or when an acceptable solution has been found. For our purpose, we use the former one and set a maximum of generations, k_{max} to 100 and use it as the termination criteria. We found out that this works well by ensuring that the swarm converges to a final solution, thereby avoiding the chances of any significant premature termination.

Target curve – We optimize for a constant $D(\theta)$ response of the mechanism. Specifically, we provide the target function $D_t(\theta) = 1.0$. The range of θ is [-60°, 60°]. Thus, we desire a total rotational motion of 120° at the hinge connecting polygon P_2 and P_5 [Fig 1.12]. A total rotational motion of 120° serves as a reasonable choice allowing for sufficient internal motion in the mechanism. We believe other choices of D within a reasonable range should work although much higher or lower values of D would render the initial population ineffective.

Code development and deployment – We first developed a quick and dirty Python program to test our model on a general-purpose computer and used guess values of the hyperparameters $\{\omega, c_1, c_2\}$. We noticed a general decay in the mean objective function values of the swarm with generation. As we rationalize in the next sections, our purposes required to run the code for considerable number of times and hence demanded high-performance computing facility. For this reason, we developed our main version in the more efficient programming environment of C++, and deployed it over the Lisa computer cluster of SURFsara [99].

3.6 Parameter Selection for Optimum Search

As a common feature of nearly all metaheuristics, the parameter setting influences the search behavior and their right values are mainly problem dependent [100]. In this section, we first understand the influence of the parameters $\{\omega, c_1, c_2\}$ on the search quality of PSO with the main aim of finding the optimal values of these parameters that impart the maximum (global) search capability to the algorithm. We remind that ω is the inertial weight, c_1 is the cognition parameter and c_2 is the social parameter. We then take a look at the distribution type of the final solution and reveal that it also depends on the values of c_1 and c_2.

3.6.1 Hyperparameter Optimization

Eq. 3.28 gives the velocity update equation for the PSO. The parameter tuple $\{\omega, c_1, c_2\}$ are the central parameters. A balance between exploration and exploitation is crucial in all gradient-free algorithms, achieving which in the case of PSO relies on a correct parameter setting of $\{\omega, c_1, c_2\}$. These parameters characterize the movement of particles, and the success and failure of the search is heavily dependent on the values of these parameters. In our case, 'poor' search can be identified as the one where the swarm is unable to locate optimal or close to optimal solutions with sufficiently low values of the objective function $\boldsymbol{f}$. Either of these scenarios can result in a poor search: *(i)* particles lose their velocities rapidly and become stationary, *(ii)* particles converge to a locally optimal but poor solution and are unable to 'leap-out' of it, *(iii)* particles fly around in random fashion, and *(iv)* particles gain excessive velocities and 'fly-out' of the search space

Effect of c_1 and c_2 parameters – In order to locate the *sweet-spot* in the parameter space, we first understand the effect of the cognition parameter c_1 and the social parameter c_2 on the quality of the final solution while keeping the inertial weight ω fixed. We begin with a low value of ω and keep it fixed at 0.25. We choose the traditional method for performing hyperparameter optimization: *grid search*, which is simply an exhaustive searching through a specified subset of the parameters [101]. We cover a total range of [0.0, 3.50] in both c_1 and c_2 dimensions and discretize the (c_1, c_2) phase space linearly into a 15×15 grid so that c_1 and c_2 take on values 0.0, 0.25, 0.50 . . . . 3.50. To average out the effect of random

numbers, PSO is run 100 times (denoted by n_{PSO}) for every parameter setting.

Following the notational rule introduced in the §3.5, we define two more notations: *(i)* $< [\boldsymbol{f}(x_i^k)]_{i,k_{max}} >_{n_{PSO}}$ denotes the mean objective function value of the best solution discovered at the termination of a PSO search for a certain parameter setting. The mean is calculated over n_{PSO} runs. We explain the notation. By following the notational rule introduced earlier, $[\boldsymbol{f}(x_i^k)]_{i,k_{max}}$ denotes the objective function value of the best solution discovered across the entire swarm at the generation k_{max} i.e. at the termination of a search and $< [\boldsymbol{f}(x_i^k)]_{i,k_{max}} >_{n_{PSO}}$ denotes the mean value of it calculated across n_{PSO} runs. *(ii)* Similarly, $[[\boldsymbol{f}(x_i^k)]_{i,k_{max}}]_{n_{PSO}}$ denotes the best objective function value that could be discovered while carrying out n_{PSO} runs with a certain parameter setting, thereby representing the extreme statistics.

The most intuitive method to visualize and examine the influence of the cognition parameter c_1 and social parameter c_2 on the search capability of PSO is through a heatmap in the (c_1, c_2) phase space. Through a heatmap in Fig. 3.18(a), we show the variation of $< [\boldsymbol{f}(x_i^k)]_{i,k_{max}} >_{n_{PSO}}$, and in Fig. 3.18(b), we show the variation of $[[\boldsymbol{f}(x_i^k)]_{i,k_{max}}]_{n_{PSO}}$ as we parse through the c_1-c_2 grid. The values corresponding to the color in the grids can be estimated from the colorbar on the right.

Based on the figure, we draw several observations. *(i)* As expected, the parameter setting with zero social parameter value i.e. $c_1 \neq 0$ and $c_2 = 0$ leads to an immensely poor performance. Particles have no communication with each other and only individually explore the search space. *(ii)* Owing to significantly high values of $< [\boldsymbol{f}(x_i^k)]_{i,k_{max}} >_{n_{PSO}}$, c_1, c_2 parameter values that belong to the top right corner of the grid also lead to a poor performance. We will show in the next section that within this region, the particles either display non-convergent search behavior i.e. they fly randomly or they display divergent search behavior i.e. they fly out of the search space. *(iii)* For the rest of the (c_1, c_2) values, although we do not notice a huge difference in the general scales of $< [\boldsymbol{f}(x_i^k)]_{i,k_{max}} >_{n_{PSO}}$, the values of $[[\boldsymbol{f}(x_i^k)]_{i,k_{max}}]_{n_{PSO}}$ help to separate out the parameter settings that outperforms the rest i.e. high c_2 values and low c_1 values. Hence, the large blue region in Fig. 3.18(b) corresponds to a much improved PSO performance. Most of these (c_1, c_2) values satisfy the following two conditions:

$$c_1 + c_2 \leq 3.50; \quad c_2 \geq 1.50. \tag{3.29}$$

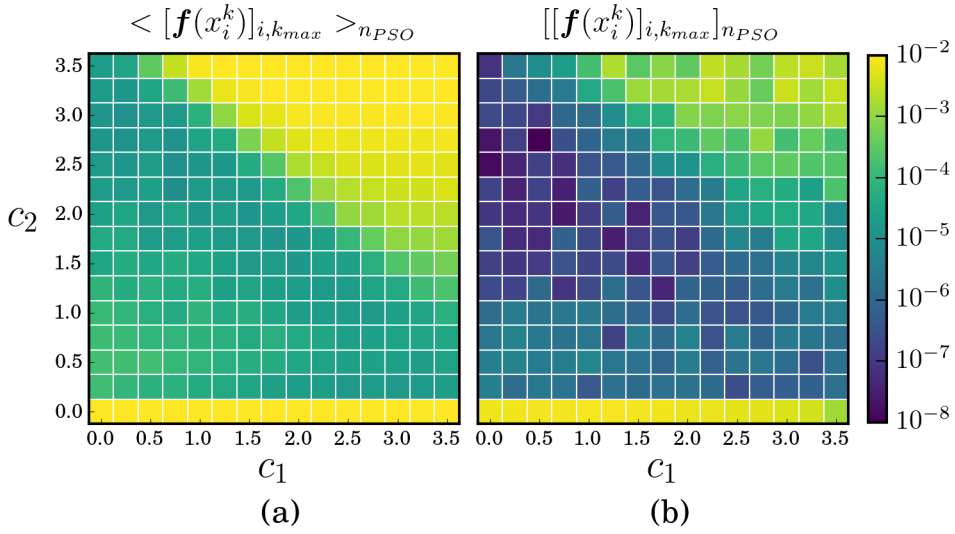

Figure 3.18: For $\omega = 0.25$, the values of $< [\boldsymbol{f}(x_i^k)]_{i,k_{max}} >_{n_{PSO}}$ in (a) and $[[\boldsymbol{f}(x_i^k)]_{i,k_{max}}]_{n_{PSO}}$ in (b) shown for different (c_1, c_2) parameter settings. Over separate n_{PSO} runs, $< [\boldsymbol{f}(x_i^k)]_{i,k_{max}} >_{n_{PSO}}$ denotes the mean value of the best objective function values and $[[\boldsymbol{f}(x_i^k)]_{i,k_{max}}]_{n_{PSO}}$ denotes the best value itself. The colorbar on the right specifies the numerical values corresponding to the colors in the matrix. Lower values of $[[\boldsymbol{f}(x_i^k)]_{i,k_{max}}]_{n_{PSO}}$ in (b) for low values of c_1 and high values of c_2 confirm their overall better performance.

Effect of the inertial weight ω – We now vary ω and examine its influence on $< [\boldsymbol{f}(x_i^k)]_{i,k_{max}} >_{n_{PSO}}$ and $[[\boldsymbol{f}(x_i^k)]_{i,k_{max}}]_{n_{PSO}}$. The variation of these two quantities with ω is shown in Fig. 3.19 for its three different values: (a,b) - $\omega = 0.40$, (c,d) - $\omega = 0.60$ and (e,f) - $\omega = 0.80$. Increasing ω results in: *(i)* Expansion of the poor-performing region, and *(ii)* vertical downward shift of the sweet-spot. This seems justified - an increase in ω results in higher velocity magnitudes of the particles, thereby increasing chances for non-convergent search behavior. On the other hand, an increase in ω also results in increased global search capability even for low values of c_2. The influence of ω seems systematic, however, we do not observe any significant improvement in the quality of solutions. For further analysis, we keep the value of ω fixed at 0.25.

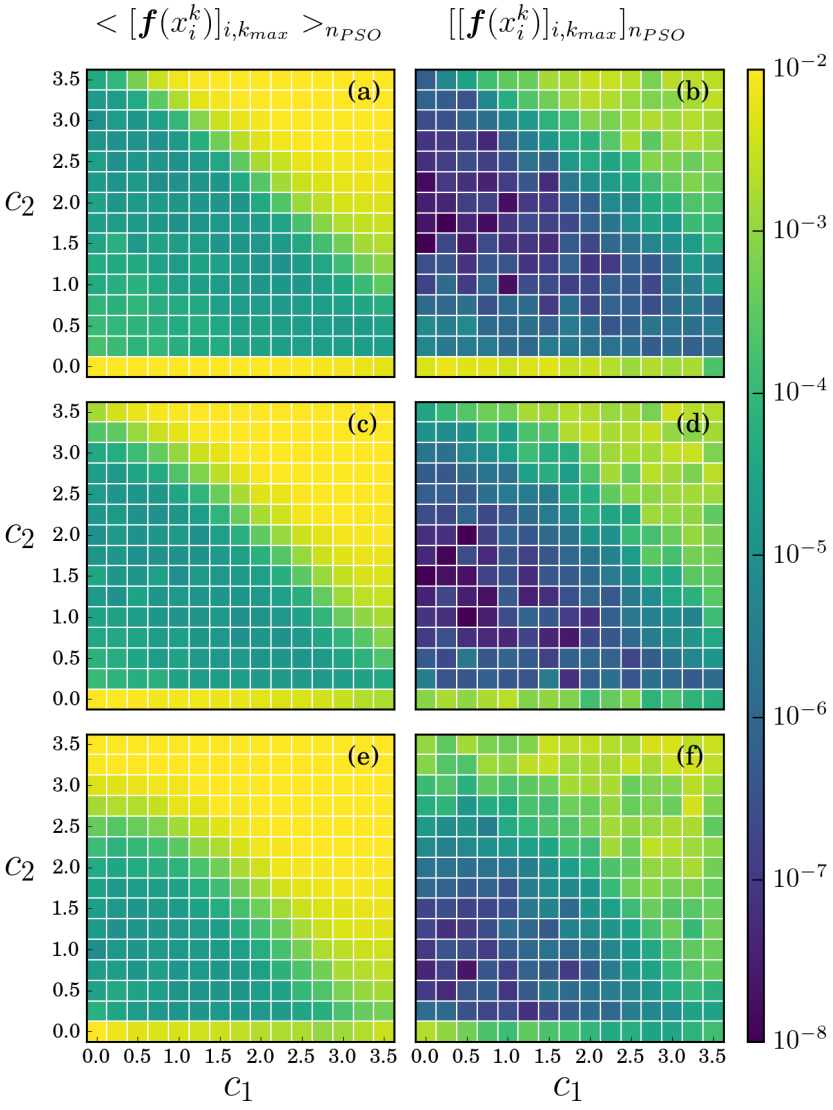

Figure 3.19: Variation of $< [\boldsymbol{f}(x_i^k)]_{i,k_{max}} >_{n_{PSO}}$ (first column) and $[[\boldsymbol{f}(x_i^k)]_{i,k_{max}}]_{n_{PSO}}$ (second column) in the (c_1, c_2) space for different values of ω. (a, b) - $\omega = 0.40$. (c, d) - $\omega = 0.60$. (e, f) - $\omega = 0.80$. Effect of ω is systematic but there is no notable effect on the performance of PSO.

3.6.2 Distribution of Final Solutions

We will now take a detailed look at the distributions of $[\boldsymbol{f}(x_i^k)]_{i,k_{max}}$ through which we will demonstrate that: *(i)* within the non-convergent regime, i.e. for higher values of both c_1 and c_2, the final solution $[\boldsymbol{f}(x_i^k)]_{i,k_{max}}$ can essentially be described by a gaussian distribution, and *(ii)* we will also show that a lognormal distribution fits the data well for the best performing parameter setting in the (c_1, c_2) space, given by Eq. 3.29.

In Fig. 3.20(a), cumulative distribution function (CDF) of $[\boldsymbol{f}(x_i^k)]_{i,k_{max}}$ is shown for several parameter settings with higher values of both c_1 and c_2 (labeled on a grid). A sharp jump in the CDF's is noticed for many of the settings due to no improvement from the initial population itself. Overall, these parameters result in a poor PSO performance. In Fig. 3.20(b), it is shown that rescaling each CDF by subtracting its mean and dividing by its standard deviation causes all the data to collapse reasonably well onto the CDF of standard gaussian distribution, $D(\chi)$ for a random variable χ:

$$D(\chi) = \frac{1}{2}\left[1 + erf\left(\frac{\chi}{\sqrt{2}}\right)\right], \tag{3.30}$$

where erf is the error function. $\boldsymbol{f}$ is rescaled as:

$$\boldsymbol{f}_c = \frac{[\boldsymbol{f}(x_i^k)]_{i,k_{max}} - \left\langle [\boldsymbol{f}(x_i^k)]_{i,k_{max}} \right\rangle}{SD\left([\boldsymbol{f}(x_i^k)]_{i,k_{max}}\right)}. \tag{3.31}$$

The CDF for a standard Gaussian distribution is shown in red in Fig. 3.20(b). The collapse suggests that for each of these parameter settings, the variable $[\boldsymbol{f}(x_i^k)]_{i,k_{max}}$ is normally distributed:

$$[\boldsymbol{f}(x_i^k)]_{i,k_{max}} \sim N(\mu, \sigma^2), \tag{3.32}$$

with general values of μ and σ. This is not surprising - at higher values of c_1 and c_2, PSO behaves similar to a random search. We show evidence of this in the next section.

The quality of fit can be measured through residual plots. The residual measures the deviation between the data points and the fit by calculating their difference. In Fig. 3.20(c), we plot the residual values for the Gaussian distribution fit. We remind that for one parameter setting, there are a total of 100 marker points each corresponding to one PSO simulation. We observe the lack of any general trend.

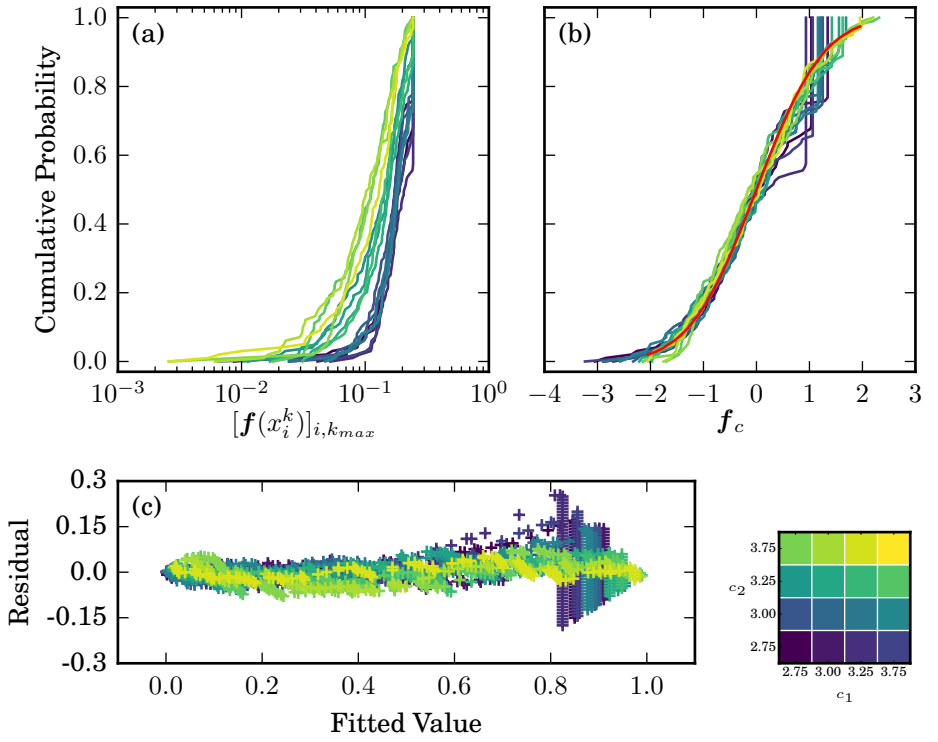

Figure 3.20: For high values of both c_1 and c_2 (see color-guide on the bottom-right): (a) cumulative distribution function (CDF) of $[\boldsymbol{f}(x_i^k)]_{i,k_{max}}$, (b) rescaled cumulative distribution function (CDF) of $[f(x_i^k)]_{i,k_{max}}$ [Eq. (3.31)] collapses the data reasonably well to a standard Gaussian distribution (shown in red). (c) Residual plot for the rescaled CDF's lacks any particular trend as such and thus shows that the CDF of the fitted standard Gaussian distribution matches the behavior very well.

We now probe the region in the (c_1, c_2) space that performed better than the rest on the metrics of $[[\boldsymbol{f}(x_i^k)]_{i,k_{max}}]_{n_{PSO}}$. Refer to Fig. 3.18(b) and Eq. 3.29. For a subset of these parameter values, we show the CDF's of $[\boldsymbol{f}(x_i^k)]_{i,k_{max}}$ in Fig. 3.21(a). Color-codes are provided on the bottom-right of the figure for c_1, c_2 values. In order to collapse all the data on to a single curve, a rescaling of the data is performed. We first log-transform $[\boldsymbol{f}(x_i^k)]_{i,k_{max}}$ by taking its natural log. The log-transformed data is then

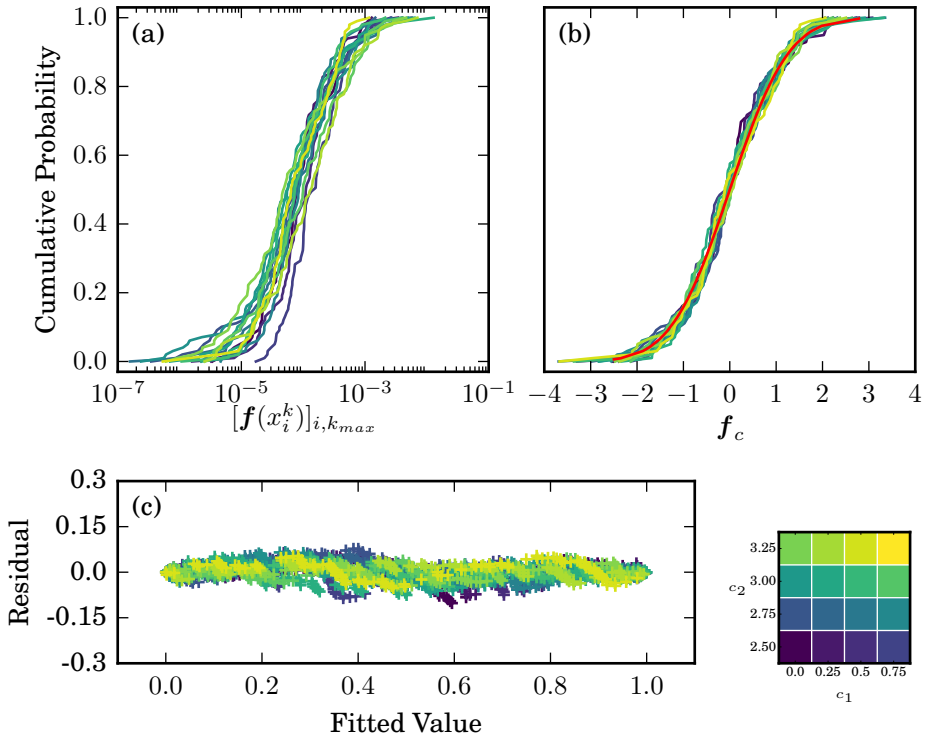

Figure 3.21: For low values of c_1 and high values of c_2 (see color-guide on the bottom-right): (a) cumulative distribution function (CDF) of $[\boldsymbol{f}(x_i^k)]_{i,k_{max}}$, (b) rescaled cumulative distribution function (CDF) of $[f(x_i^k)]_{i,k_{max}}$ [Eq. (1.34)] collapses the data reasonably well to a log-normal distribution. The fitted log-normal CDF is shown in the red color. (c) Residual plot for the rescaled CDF's lacks any systematic trend and shows that the fitted log-normal distribution matches the empirical distribution well.

divided by its standard deviation. This makes the standard deviation of distribution equal to 1. Let us denote this rescaled value of $\boldsymbol{f}$ by $\boldsymbol{f}_s$. We then subtract the mean of $\boldsymbol{f}_s$ from $\boldsymbol{f}_s$ itself and divide the result by the standard deviation of $\boldsymbol{f}_s$. Finally the rescaled values are denoted by $\boldsymbol{f}_c$. The

following equations summarizes up the rescaling of $[\boldsymbol{f}(x_i^k)]_{i,k_{max}}$:

$$\boldsymbol{f}_s = \frac{\ln([\boldsymbol{f}(x_i^k)]_{i,k_{max}})}{SD\left(\ln([\boldsymbol{f}(x_i^k)]_{i,k_{max}})\right)} \tag{3.33}$$

$$\boldsymbol{f}_c = \frac{\boldsymbol{f}_s - \langle \boldsymbol{f}_s \rangle}{SD\left(\boldsymbol{f}_s\right)} \tag{3.34}$$

For the same parameter subset, the rescaled CDF's are plotted in Fig. 3.21(b). Notice that the CDF's collapse reasonably well to the CDF of a log-normal distribution which is shown in the red color. The formula for the CDF of a log-normally distributed random variable χ is given by:

$$D(\chi) = \Phi\left(\frac{\ln(\chi)}{\sigma}\right), \quad \chi \geq 0; \sigma \geq 0 \tag{3.35}$$

where Φ is CDF of the normal distribution and σ is the standard deviation of the natural log transformation of the original data.

To measure the quality of the log-normal fit shown, we once again plot the residual values for the same parameter settings (c_1, c_2) and show them in Fig. 3.21(c). The residual values are contained within a narrow range and lack any systematic deviation. We can thus comment that the log-normal distribution serves as a sufficiently good fit.

3.7 Visualization of the Search Process

The visualization of the search process enhances our understanding and intuition into the workings of PSO. Specifically, through visualizing the movement of particles, we obtain understanding about the influence of the parameters c_1 and c_2 on the search process. But firstly, visualizing the search that takes place in a high-dimensional domain requires performing a dimensionality-reduction, wherein we map particle positions from the high-dimensional space onto a low-dimensional space (2D), while minimizing distortions of the data. To reduce the dimensionality, we adopt a technique known as *Sammon's Mapping* [102].

Sammon's mapping – We discuss here a technique that maps a dataset from a high-dimensional (say, m-dimensional) input space onto a low-dimensional (say, d-dimensional) output space (with $d < m$). The idea is

to arrange all the points in the output space such that the inter-distance relationship among data points is preserved, i.e. the distances between the data points in the output space resembles the distances in the input space as closely as possible. To do so, Sammon's mapping aims to minimize an error function that quantifies differences of distances between points in the input space and the output space. This error function is often referred as *Sammon's stress* or *Sammon's error*.

Consider a dataset of n data points. If the distance between two points x_i and x_j in the input space is denoted by δ_{ij} and the distance between the corresponding mapped x'_i and x'_j in the output space is denoted by d_{ij}, then SammonâĂŹs stress measure, S is defined as follows:

$$S = \frac{1}{\sum_{i=1}^{n-1}\sum_{j=i+1}^{n}\delta_{ij}} \sum_{i=1}^{n-1}\sum_{j=i+1}^{n} \frac{(\delta_{ij} - d_{ij})^2}{\delta_{ij}}. \tag{3.36}$$

The range of S is [0,1] with 0 indicating a lossless mapping. To minimize the stress measure S, any standard gradient based algorithm can be deployed. We used *gradient descent* algorithm.

We will now implement Sammon's mapping to visualize the initial population $\{x_i\}$, i = 1, 2, . . . 50. The transformed dataset is given by $\{x'_i\}$. $\{x'_i\}$ is first initialized in the 2D plane by performing principal component analysis (PCA) on $\{x_i\}$. We show the mapped points in Fig. 3.22(a). An arbitrary, random initialization is also sufficient although PCA leads to some performance improvement [103]. The initial value of Sammon's stress S is 0.255. As, S is minimized, the evolving positions of the particles is shown in the Fig. 3.22 (b-d) for iterations 4, 16 and 64 respectively of the gradient descent procedure. We show the decay of S in Fig. 3.22(e) and observe that S decays down to a residual of ≈ 0.066, below which the loss in the mapping cannot be minimized. Visually, the mapped positions do not alter much after enough iterations and Fig. 3.22(d) effectively shows the Sammon's mapping of the initial population and interestingly illustrates that the initial population $\{x_i\}$ is distributed uniformly. Using the similar procedure, we can map the position of the particles onto the 2D plane for every generation and use this technique to visualize the PSO search procedure.

We now demonstrate the influence of different (c_1, c_2) parameter settings on the PSO search process through the help of four distinct cases. We remind that ω is kept fixed at 0.25.. For each of these cases, we map the

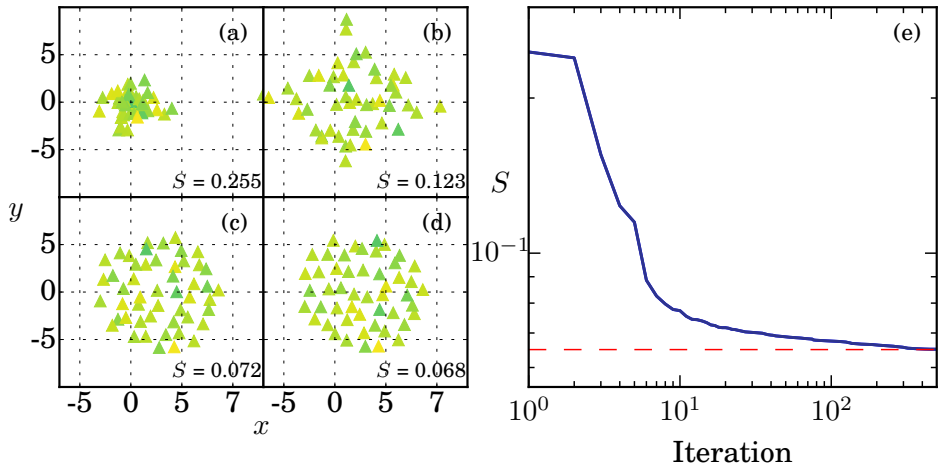

Figure 3.22: The initial population used to initialize PSO mapped onto a 2D space using Sammon's Mapping. (a-d) Snapshots of the mapped positions for iterations 0, 4, 16 and 64 of the gradient descent procedure. Color of the markers denotes the value of $\boldsymbol{f}$ and is based on the colorbar shown in Fig. 3.19. (e) Decay of S versus the gradient descent iterations. The residual value of S is recorded to be 0.065.

particle positions at generations 0, 4, 16 and 64 is shown in Fig. 3.23. In the figure, the color of the data points represents the objective function value $\boldsymbol{f}$, which can be decoded from the colorbar shown in Fig. 3.19. The four cases are discussed below:

(i) $c_1 = 0.25, c_2 = 0.25$ [Fig. 3.23 (a)]: We can observe that the swarm quickly loses diversity and shrinks continuously through generations. With this setting, the swarm lacks global exploration capability and converges at best to a poor local optimum. Thus, only a local exploration of the search space takes place with this parameter setting i.e. low values of both c_1 and c_2.

(ii) $c_1 = 0.0, c_2 = 3.0$ [Fig. 3.23 (b)]: Compared to the previous case, we observe a much broader exploration of the search space taking place before the particles ultimately converge towards a solution. The enhanced global search capability improves the quality of final solution with the pa-

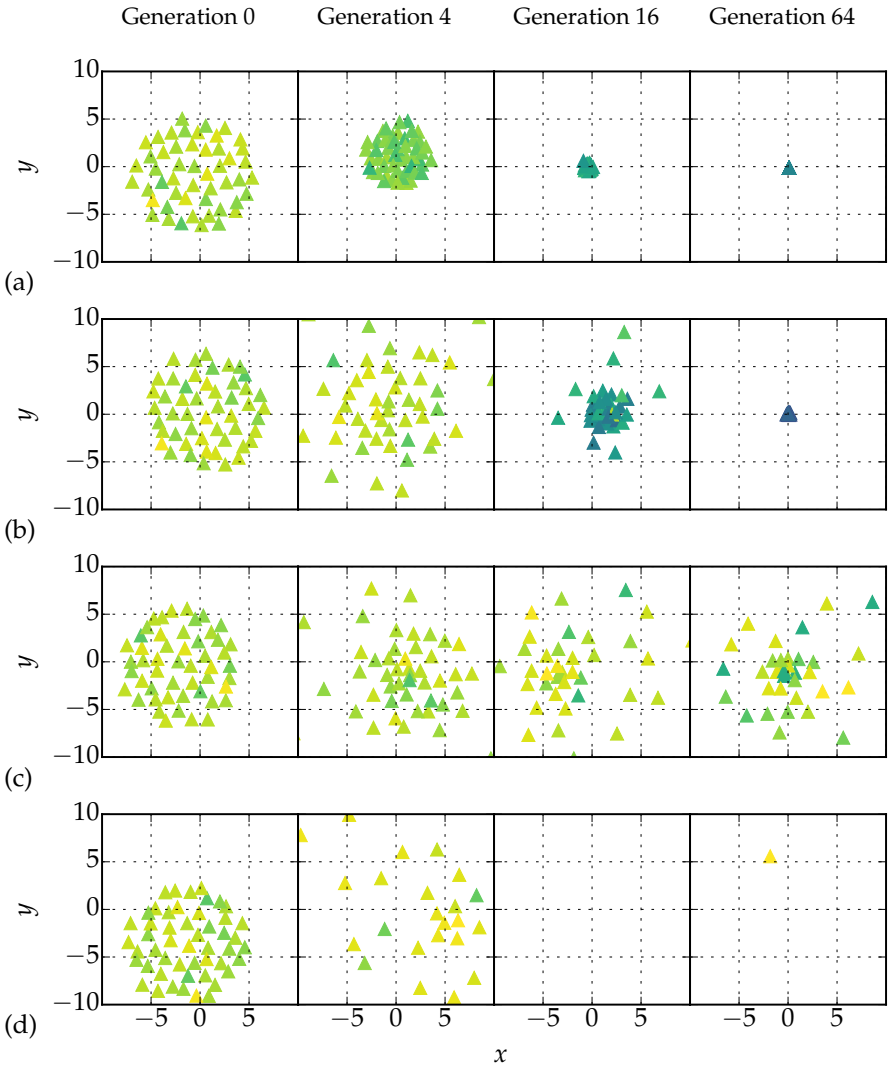

Figure 3.23: Sample PSO runs for different $\{0.25, c_1, c_2\}$ settings visualized through Sammon's mapping. (a) {0.25, 0.25, 0.25} - local search, (b) {0.25, 0.0, 3.0} - global search, (c) {0.25, 2.00, 2.00} - random search and (d) {0.25, 2.25, 2.25} - divergent search. The particle positions are shown for generations 0, 4, 16 and 64 of PSO. Color of the markers denotes the value of $\boldsymbol{f}$ and is based on the colorbar shown in Fig. 3.19.

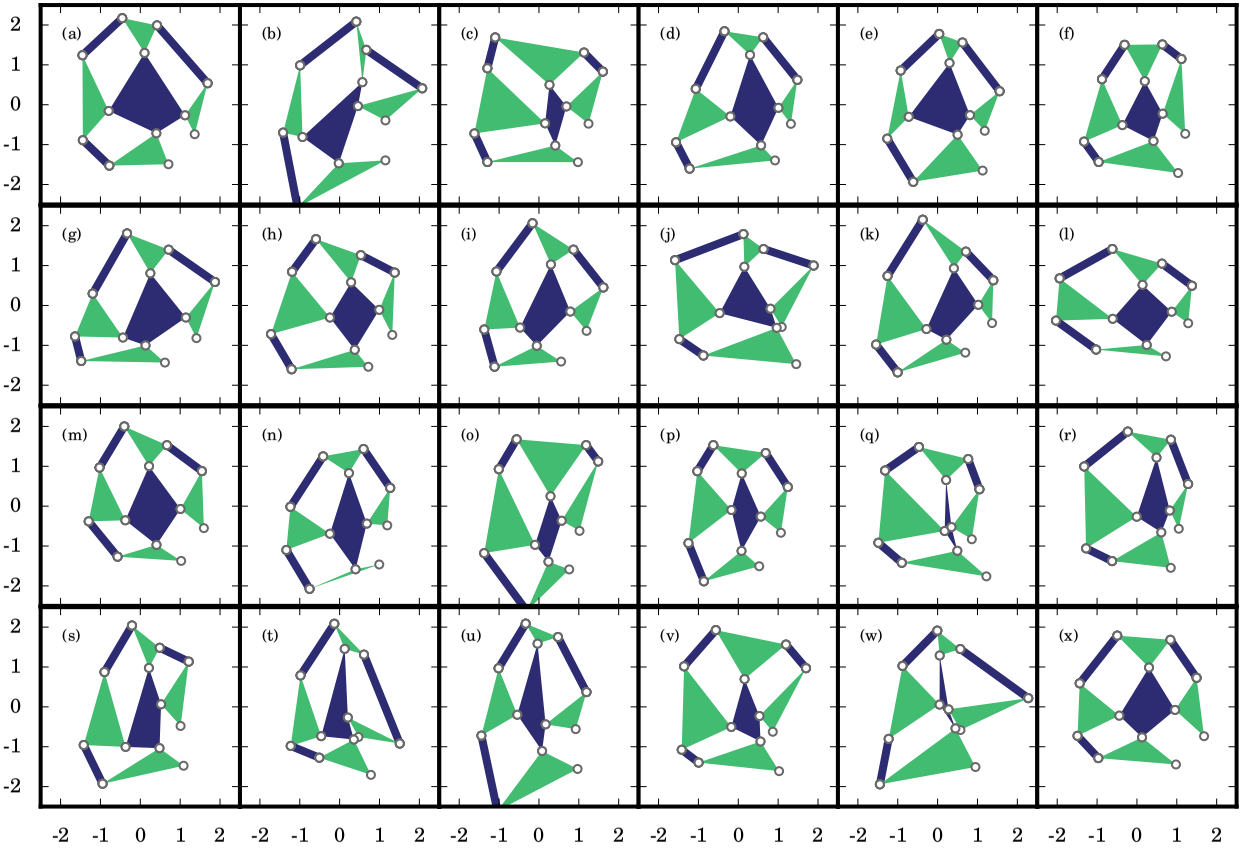

Figure 3.24: (a) - (x): A gallery of top solutions for the target curve $D_t(\theta) = 1.0$ out of an ensemble of 22,500 independent PSO runs. The final objective function value $[\boldsymbol{f}(x_i^k)]_{i,k_{max}}$ for these solutions ranges from 1.6×10^{-7} to 1.3×10^{-6}.

rameter settings where c_1 takes on low values and c_2 takes on high values.

(iii) $c_1 = 2.0, c_2 = 2.0$ [Fig. 3.23 (c)]: Intermediately high values of both c_1 and c_2 make PSO a random search procedure. We observe that the particles fly randomly through the search space without converging towards a solution.

(iv) $c_1 = 2.25, c_2 = 2.25$ [Fig. 3.23 (d)]: With a further increase in the values of c_1 and c_2, the swarm 'collapses' and the particles positions diverge, making the particles escape-out the search space.

The visualization the search process provide us with the evidence that with the optimal parameter setting [Eq. (3.29)], the swarm carries out a broad exploration of the search space before converging to a solution.

3.8 Results

We have demonstrated the entire machinery to carry out the computer-aided design of mechanisms that meet the target curve $D_t(\theta)$: $D_t = 1.0$ (§3.4 - §3.6). From an ensemble of 2.25×10^{-4} independent PSO runs, the data for which was previously summarized in Fig. 3.18, we extract the top 24 solutions based on the final objective function value $[\boldsymbol{f}(x_i^k)]_{i,k_{max}}$ and display them in Fig. 3.24. $[\boldsymbol{f}(x_i^k)]_{i,k_{max}}$ for these solutions ranges from 1.6×10^{-7} to 1.3×10^{-6}. We obtained these solutions for distinct $\{\omega = 0.25,$ $c_1,$ $c_2\}$ settings, however, all of them lye within the best-performing (c_1, c_2) subspace, previously defined by the Eq. 3.29. The richness of the objective function landscape in terms of number of distinct possible approximate solutions is reflected in the diversity of the mechanism design.

We pick the solution shown in Fig. 3.24(a) and show how it 'evolves' with generations, k in Fig. 3.25. The mechanisms shown in the figures (a)-(d) are the best solutions (out of the total 50 population members) found up to $k = 0$, 4, 16 and 64. The objective function values are labeled and denoted through $\boldsymbol{f}$. The corresponding $D(\theta)$ curves are shown in the figures (e)-(h). This particular solution was discovered with the parameter settings $\{\omega, c_1, c_2\} = \{0.25, 0.0, 3.0\}$. The improvement in the performance of the swarm over 100 generations is illustrated in Fig. 3.26 by the decay in the mean objective function value $< \boldsymbol{f}(x_i^k) >_i$ with generation k in (a) and the best objective function value $[\boldsymbol{f}(x_i^k)]_{i,k}$ discovered up to generation k in (b).

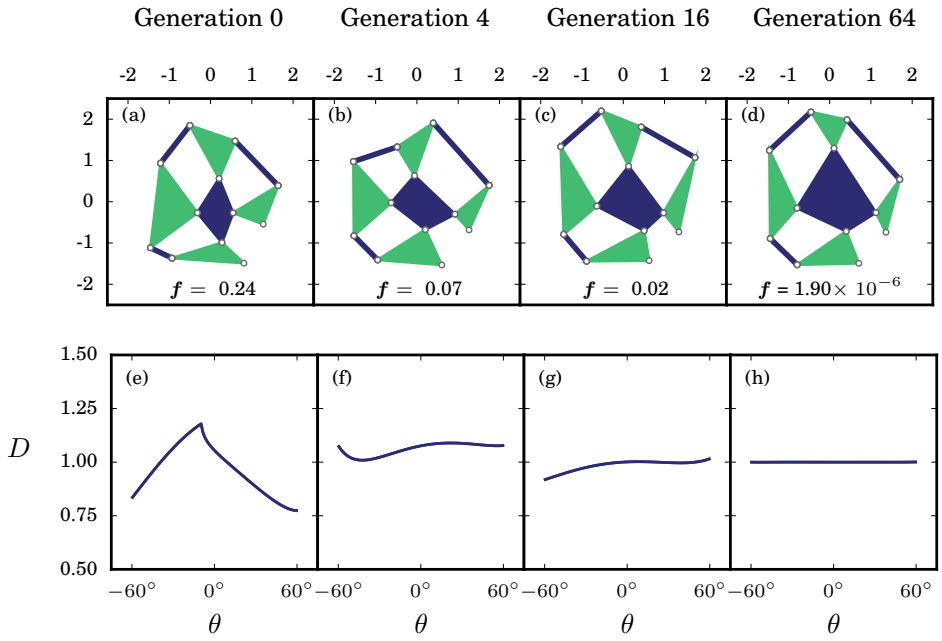

Figure 3.25: Evolution of the final solution shown in Fig. 3.24(a). For generation, $k = 0$, 4, 16 and 64, the successive figures (a)-(d) show the best solutions and (e)-(h) show their corresponding $D(\theta)$ curves. In (a)-(d), $\boldsymbol{f}$ denotes the objective function values.

3.8.1 Validation of the Local Minimum

Finding the global optimum is difficult to guaranteed in a high-dimensional space; nevertheless PSO allows to discover many approximate solutions with very low objective function values. A natural question is: where in the objective function landscape are these solutions 'sitting' or specifically, do the approximate solutions correspond to local minima in the objective function landscape? In general there is not strict guarantee that this is the case. This subsection is aimed at answering the above raised question in details through the help of statistics. In particular, we present evidences that a good PSO search that leads to a good quality final solution ends in a local minimum while this is not true for a poor search.

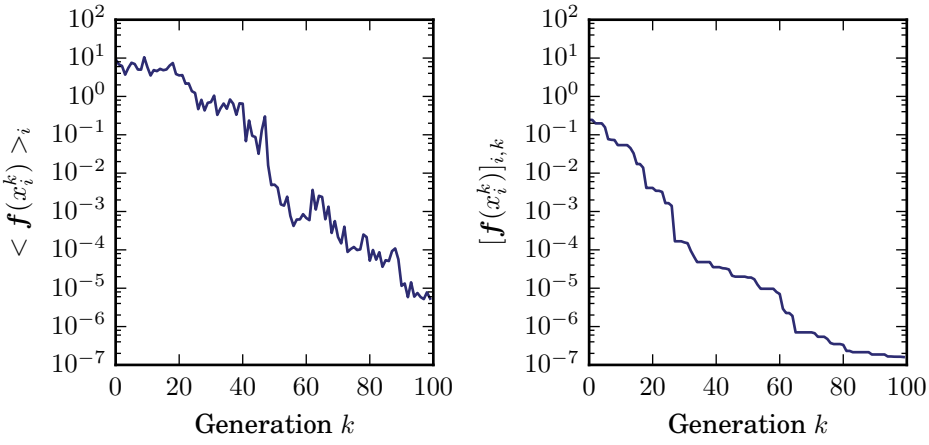

Figure 3.26: The decrease in (a) the mean objective function value $< \boldsymbol{f}(x_i^k) >_i$ with generation k and (b) the best objective function value $[\boldsymbol{f}(x_i^k)]_{i,k}$ discovered up to the generation k as a function of k for the example shown Fig. 3.25.

For a good PSO search – To illustrate our approach, we choose the final solution: $[x_i^k]_{i,k_{max}}$ shown in Fig. 3.24(a) and would like to test if this is a local minimum. Since in this subsection we are mainly interested about the final solutions only, we denote $[x_i^k]_{i,k_{max}}$ with $\boldsymbol{x}$ to avoid unnecessary complexity in the notations although we will return to the original notation if necessary. The numerical procedure for testing if $\boldsymbol{x}$ corresponds to a local minimum is stated on the next page in a procedural form:

For simplicity in notations, we denote $\boldsymbol{f}(x)$ with $\boldsymbol{f}$ and $\boldsymbol{f}(\boldsymbol{x} + \epsilon\hat{d})$ with $\boldsymbol{f}_p(\epsilon)$. Following the procedure described above, we show the variation in $\boldsymbol{f}_p(\epsilon)$ for five different choices of $\hat{d}$ in Fig. 3.27(a). ϵ covers the range [0, 10^{-2}] with the smallest stepsize [6] of 1×10^{-4}. Firstly, we observe a near quadratic increase in $\boldsymbol{f}_p$ with ϵ only around the immediate vicinity of $\epsilon = 0.0$ (see inset). Considering the really small scale of $\boldsymbol{f}_p$ compared with ϵ, this seems justified. To be able to see a clear parabolic increase, we need to zoom in further into ϵ, the choice of which is limited by numerical precision.

[6] Our estimate for the smallest value of stepsize such that the numerical noise is avoided. We discuss this in more detail towards the end of this subsection.

Procedure – Test if a final solution $\boldsymbol{x}$ corresponds to a minimum in the objective function landscape.

Inputs :

1: Final solution $\boldsymbol{x}$.
2: Stepsize range ϵ.
3: Total number of perturbed directions n_{pert}.
4: Unique perturbed direction $\hat{d}$ (and -$\hat{d}$) for each n_{pert}, where $\hat{d}$ is a 24 dimensional unit vector consisting of random numbers sampled from a uniform distribution.

Result : $\boldsymbol{x}$ corresponds to a local minimum if $\boldsymbol{f}(\boldsymbol{x} + \epsilon\hat{d})$ increases (approximately quadratically) with ϵ for all the n_{pert} directions.

Secondly, we observe that for larger values of ϵ, $\boldsymbol{f}_p$ increase linearly, the reason for which is the large difference in the scales of $\boldsymbol{f}_p$ and ϵ. The results are however are consistent with $\boldsymbol{x}$ being a local minimum.

Five random directions $\hat{d}$ cannot be sufficient to establish that $\boldsymbol{x}$ is indeed a local minimum. A stronger test is: we keep ϵ fixed, and calculate the values of $\boldsymbol{f}_p$ for 1000 random choices of $\hat{d}$ i.e $n_{pert} = 1000$. This we do for six separate values of ϵ: 1.0 x 10^{-3}, 2.0 x 10^{-3}, 4.0 x 10^{-3}, 6.0 x 10^{-3}, 8.0 x 10^{-3} and 10^{-2}. The distribution of $\boldsymbol{f}_p(\epsilon)$ is summarized through cumulative distribution functions (CDF's) in Fig. 3.27(b). There, the vertical dashed line represents $\boldsymbol{f}$, the objective function value of the original solution $\boldsymbol{x}$, and our data shows that all $\boldsymbol{f}_p$ values lie to the right of this line. The horizontal shift between these curves shows that the typical values of $\boldsymbol{f}_p(\epsilon)$ increases with ϵ. Our data presents strong evidence that the solution shown in Fig. 3.24(a) corresponds to a local minimum.

For a poor PSO search – Similarly, we can examine the variation of $\boldsymbol{f}_p(\epsilon)$ in the vicinity of final solution $\boldsymbol{x}$ resulting from a 'poor' PSO search. Based on the final objective function value, we identify one such search from our main ensemble of solutions. The parameter settings corresponding to this search are $\{\omega, c_1, c_2\} = \{0.25, 0.50, 0.50\}$. By performing the previously aforementioned procedure, we show in Fig. 3.28(a) the plot $\boldsymbol{f}_p$ as a function of ϵ. We observe that: *(i)* some of the perturbations $\hat{d}$ lead to a decrease in $\boldsymbol{f}_p$, we call such perturbations as *negative perturbations*, and *(ii)* we no longer have the *local parabolas* observed for the previous case and instead

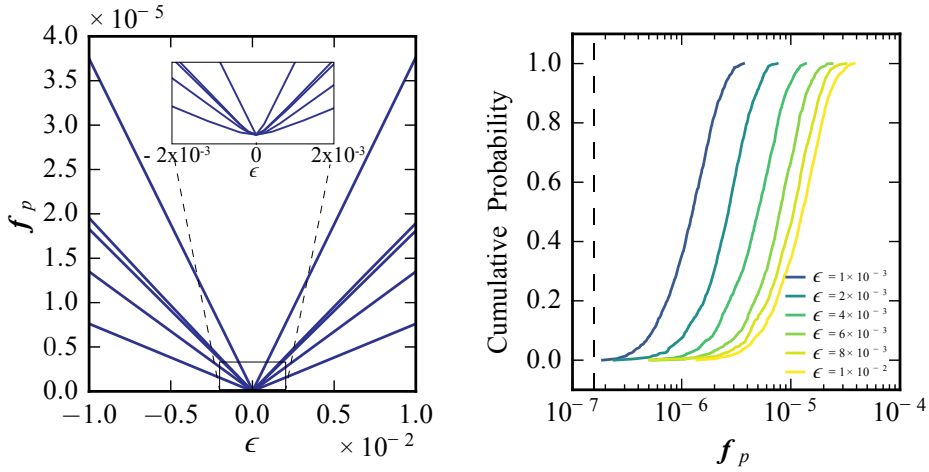

(a) **(b)**

Figure 3.27: (a) For five different choices of $\hat{d}$, $\boldsymbol{f}_p$ vs ϵ for a 'good' solution (Fig. 3.24(a), $\boldsymbol{f} = 1.6 \times 10^{-7}$). Inset figure shows a near quadratic increase in $\boldsymbol{f}_p$ for very low ϵ values. (b) CDF's of $\boldsymbol{f}_p(\epsilon)$ for six different values of ϵ, for each of which $n_{pert} = 1000$. The objective function value $\boldsymbol{f}$ of the unperturbed solution in (a) corresponds to the value of $\boldsymbol{f}_p$ for $\epsilon = 0.0$ and is marked by the dashed black line in (b) w.r.t. which all the values of $\boldsymbol{f}_p$ are higher, thereby proving strong evidence that the solution is a local minimum in the objective function terrain.

find that the variation in $\boldsymbol{f}$ with ϵ depends on the direction in which $\boldsymbol{x}$ is perturbed, implying that $\boldsymbol{x}$ cannot be a local minimum.We further confirm this argument by providing the CDF's of $\boldsymbol{f}_p(\epsilon)$ for the same six values of ϵ as before, with n_{pert} set to 1000 for every value of ϵ. In Fig. 3.28(b), the inset reveals the presence of negative perturbations for all values of ϵ.

Resolutions of PSO – In the previous discussion we remarked that the smallest choice of ϵ might be sensitive to the finite precision with which $\boldsymbol{x}$ is determined and as a guess chose it to be 1×10^{-4}. This worked fine as we did not notice any noise for the data shown in Fig. 3.27. By going much further below in ϵ, here, we explore this topic in detail: the effect of small values of ϵ on the perturbed solutions. By varying ϵ and calculating the

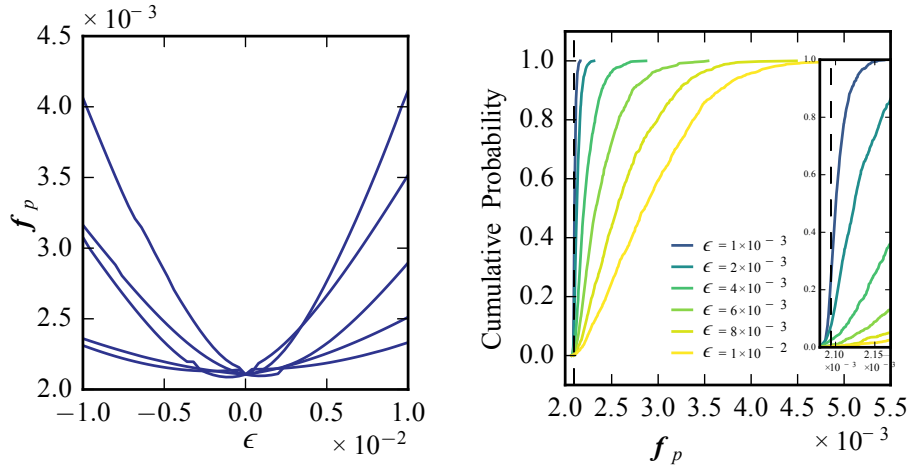

(a) **(b)**

Figure 3.28: (a) For five different choices of $\hat{d}$, $\boldsymbol{f}_p$ vs ϵ for a 'bad' solution $\boldsymbol{x}$. The objective function value of $\boldsymbol{x}$ is $\boldsymbol{f} = 2.09 \times 10^{-3}$. In the vicinity of $\boldsymbol{x}$, $\boldsymbol{f}_p < \boldsymbol{f}$, which implies that $\boldsymbol{x}$ cannot correspond to a local minimum. This, we confirm statistically. (b) CDF's of $\boldsymbol{f}_p(\epsilon)$ for six different values of ϵ, for each of which $n_{pert} = 1000$. The objective function value $\boldsymbol{f}$ of the unperturbed solution in (a) corresponds to the value of $\boldsymbol{f}_p$ for $\epsilon = 0.0$ and is marked by the dashed black line in (b) w.r.t. which some of the values of $\boldsymbol{f}_p$ are actually lower, thus confirming that $\boldsymbol{x}$ is not a local minimum.

statistics of $\boldsymbol{f}_p$, we can calculate the quality of solution $\boldsymbol{x}$ as well as getting an idea about the numerical precision which the local minima are obtained.

We stick with the solution shown in Fig. 3.24(a) and demonstrate the effect of small values of ϵ on the objective function value of the perturbed solutions. To quantify the statistics, for a fixed ϵ, we performed 1000 perturbations with different choices of $\hat{d}$ i.e $n_{pert} = 1000$. Fig. 3.29(a) shows the CDF's of $\boldsymbol{f}_p(\epsilon)$. The colorbar on the right indicates ϵ. The objective function value of the unperturbed solution $\boldsymbol{f}$ is marked by a red colored dashed vertical line. We observe a systematic shift in the CDF's towards the left as ϵ decreases. For these values of ϵ, we can observe the increasing presence of negative perturbations as ϵ becomes smaller. The fact that these values are still extremely close to $\boldsymbol{f}$ indicates that we run into the numerical

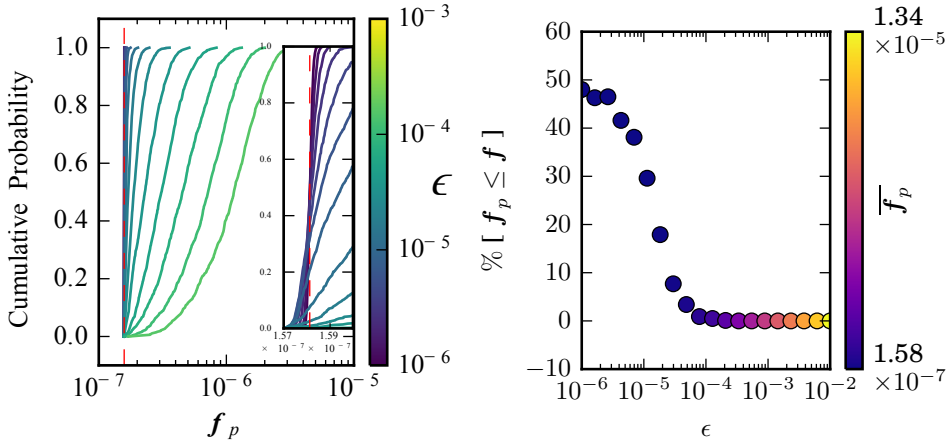

Figure 3.29: (a) CDF's of $\boldsymbol{f}_p(\epsilon)$ for small values of ϵ (see colorbar). Original solution $\boldsymbol{x}$ is shown in Fig. 3.24(a). The inset reveals the presence of negative perturbations within a very narrow range, that decrease with ϵ. (b) Percentage of negative perturbations displays an asymptotic decrease with ϵ, thereby providing with a meaningful bound on correct choice of ϵ. The color of the data points represents the mean value of 1000 perturbations, $\overline{\boldsymbol{f}_p(\epsilon)}$.

precision problems. To avoid repetition, we do not show CDF's for values of $\epsilon \geq 1 \times 10^{-3}$. They were previously shown in Fig. 3.27(b).

To be precise, for each value of ϵ, we can measure the percentage of negative perturbations. This time we cover a complete range from 10^{-6} to 10^{-2} in ϵ. The results are shown in Fig. 3.29(b), where the colorbar on the right indicates the mean of n_{pert} perturbations, $\overline{\boldsymbol{f}_p(\epsilon)}$. We observe that the percentage of negative perturbations decreases asymptotically with ϵ and reduces to zero as ϵ approaches $\sim$ 1x10^{-3}. Hence, this suggests that numerical precision with which PSO determines this local minima is of the order of 10^{-3}. This graph simultaneously provides us with a good estimate for a safe choice of the step-size ϵ to check if some solution $\boldsymbol{x}$ (within numerical accuracy) is a local minima. To perturb solutions in the coming analysis, we will keep the smallest value of ϵ to 10^{-3} while the largest value will never exceed 10^{-2}.

Can PSO escape a local minimum ? – Now that we have a numerical procedure to check whether $\boldsymbol{x}$ plausibly corresponds to a local minimum, we can ask the following question: How capable is PSO to jump out of local (near-local) minima ? We pick the sample search shown previously in Fig. 3.25 and extract out the best solutions $[x_i^k]_{i,k}$ found till the k^{th} generation for $k = 0, 1, 2.....100$. We then perturb these solutions and by measuring the percentage of negative perturbations, we can make an educated estimate of the local objective function landscape. We keep $\epsilon = 10^{-3}$ and $n_{pert} = 1000$. Fig. 3.30(a) shows the percentage of negative perturbations as a function of k and Fig. 3.30(b) shows the mean value of $\boldsymbol{f}([x_i^k]_{i,k} + \epsilon d)$, $\overline{\boldsymbol{f}_p}$ in red and $\boldsymbol{f}([x_i^k]_{i,k})$ (labeled as $\boldsymbol{f}$ in blue), both as a function of generation k. From Fig. 3.30(a), we observe that the percentage of negative perturbations fluctuates around 50% up until $k \sim 25$, after which this percentage starts to decrease. It is as if PSO is 'sliding down' on a surface in hyperdimensional space in search of a minimum. The curves in Fig. 3.30(b) further support this picture: values of $\boldsymbol{f}([x_i^k]_{i,k})$ and $\boldsymbol{f}([x_i^k]_{i,k} + \epsilon d)$ are extremely close to one another till $k \sim 25$. We then notice a sudden drop in the percentage of negative perturbations: PSO finds itself in a neighborhood where $\boldsymbol{x}$ corresponds to a minimum in $\sim 80\%$. Because we observe sharp fluctuations in the curve shown in Fig. 3.30(a), where it recovers even after dropping to very low values (k > 42), PSO intermittently escapes such regions in the search space that correspond to minima in many of the dimensions. This capability diminishes at larger generation count. Eventually, in this case PSO finds local minimum and $\boldsymbol{f}$ and $\boldsymbol{f}_p$ converge to their respective final values.

3.8.2 Validating Across Large Statistics

We have so far demonstrated the procedure for conducting a local minimum test for one good and one bad solution type each. In this section we explore the relation between the final objective function value and the fraction of negative perturbations across larger statistics. For this purpose, we carried out more PSO simulations. The implementations details of the PSO remain the same as previous. We fix ω at 0.25 and for the (c_1, c_2) parameters, we narrowed down to the good-performing set given by Eq. 3.29. This was done to ascertain that we discover a large number of solutions that are good. For each of the 36 different (c_1, c_2) pairs, 3000 PSO simulations were carried out, which provided 1.08×10^5 new data points.

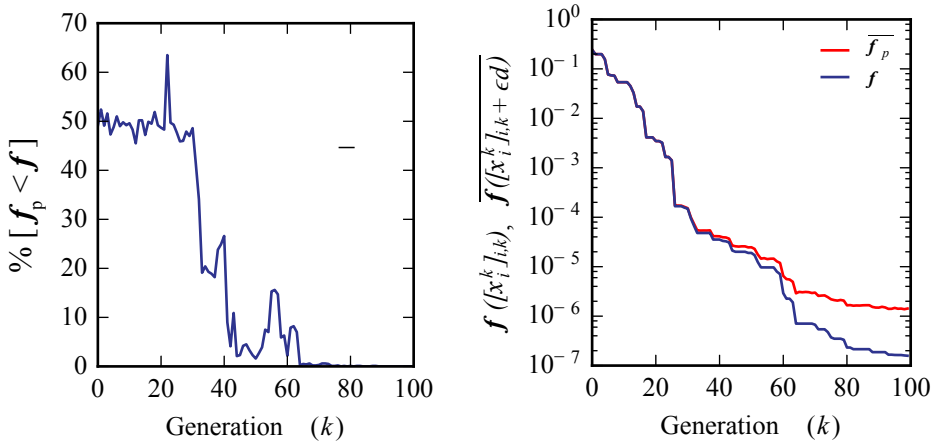

(a) (b)

Figure 3.30: (a) For the search shown in Fig. 3.25, percentage of negative perturbations as a function generation k. The value of ϵ is 1x10^{-3}. (b) Mean objective function value of 1000 perturbed solutions: $\overline{\boldsymbol{f}([x_i^k]_{i,k} + \epsilon d)}$ and the objective function value of the original unperturbed solution: $\boldsymbol{f}([x_i^k]_{i,k})$ both as a function of k.

We now discuss the issue of linkages close to becoming parallelogram linkages. We briefly discussed this in §3.2 and mainly mentioned that the 3x3 network forms a perfect mechanism when all the four internal four-bar linkages are simultaneously parallelograms. We seek to answer several new interesting questions: how does the quality of solutions correlate with the proximity of the linkages to a parallelogram? Does PSO has some bias towards discovering these solutions? We address these question in the following discussion.

We first define an order parameter to quantify the proximity of a generic four-bar linkage to a parallelogram. Consider a generic four-bar linkage Λ_i with bar lengths a_1, a_2, a_3 and a_4 in the cyclic order [Fig. 3.6]. We define a variable s_i to measure the proximity of Λ to parallelogram linkages:

$$s_i = \frac{(a_1 - a_3)^2 + (a_2 - a_4)^2}{\sqrt{a_1^2 + a_2^2 + a_3^2 + a_4^2}} \tag{3.37}$$

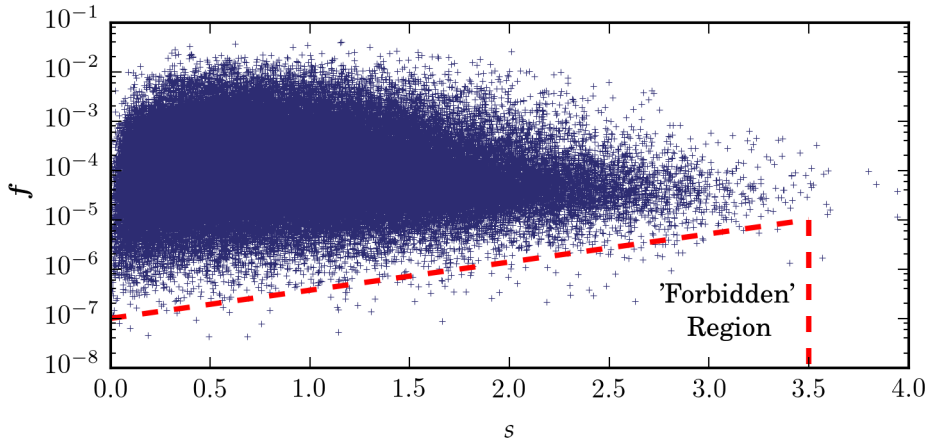

Figure 3.31: A scatter plot of objective function value $\boldsymbol{f}$ vs the order-parameter $\boldsymbol{s}$. 'Forbidden region' corresponds to the $\boldsymbol{f}$-$\boldsymbol{s}$ space where very few solutions are found.

The denominator in the above expression normalizes linkages consisting of varying bar lengths to a common scale. Clearly, the lower the value of s_i, the closer a linkage is to a parallelogram linkage. The order parameter $\boldsymbol{s}$ that measures the proximity of all the four linkages in a 3x3 system is defined as:

$$\boldsymbol{s} = \sum_{i=1}^{4} s_i \tag{3.38}$$

In Fig. 3.31, we show a scatter plot of the objective function value $\boldsymbol{f}$ and order-parameter $\boldsymbol{s}$ for our ensemble of 1.08×10^5 solutions. We observe a wide distribution for both of these variables. Importantly, we note that PSO displays a decline in its ability to discover solutions with high values of $\boldsymbol{s}$. We speculate that this may either be due to poor exploration of the higher $\boldsymbol{s}$ space or it may be possible that *search space with lower* $\boldsymbol{s}$ *values consists of larger density of deep local minima* wherein the algorithm displays a natural tendency to pursue search. This leads to the formation of a 'forbidden' region for higher $\boldsymbol{s}$ values, where PSO did not discover many solutions. It is interesting to notice that the height of the forbidden region on the *log y-axis* appears to increase almost linearly with $\boldsymbol{s}$ suggesting an exponential relation.

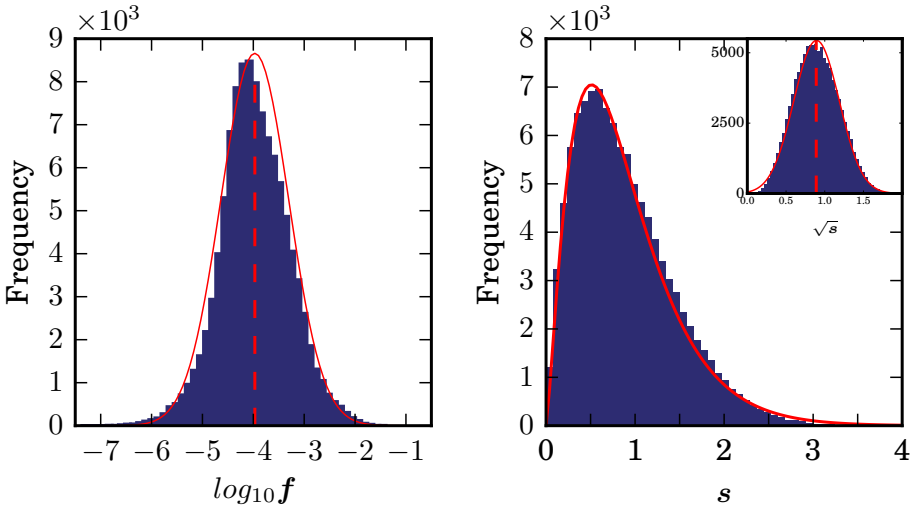

Figure 3.32: For the data shown in Fig. 3.31: (a) Histogram plot of $log_{10}\boldsymbol{f}$. The curve in red shows the PDF of a normal distribution with $\mu \sim$ -3.97 (marked by dashed vertical line) and $\sigma \sim 0.66$. This implies that $\boldsymbol{f}$ is log-normally distributed. (b) Histogram plot of $\boldsymbol{s}$. The curve in red shows the PDF of a gamma distribution implying that $\boldsymbol{s}$ is gamma distributed. Inset shows that $\sqrt{s}$ is normally distributed with $\mu \sim 0.89$ (marked by dashed vertical line) and $\sigma \sim 0.29$.

Distributions of $\boldsymbol{f}$ ($\log_{10}$ transformed) and $\boldsymbol{s}$ are shown separately through histogram plots in Fig. 3.32(a,b) respectively. For both of these plots we chose 50 bins of equal width to represent the data with $\boldsymbol{f}$ ranging from 1×10^{-8} to 1×10^{-1}, and $\boldsymbol{s}$ ranging from 3.31×10^{-3} to 3.94. The histogram shape of $log_{10}(\boldsymbol{f})$ appears to be bell-shaped like a normal distribution indicating that $\boldsymbol{f}$ is log-normally distributed; a normal distribution, shown in red, is able to fit the data well (except near the peak). The approximate fit parameters for the normally distributed $log_{10}(\boldsymbol{f})$ are: mean, $\mu \sim$ -3.97 and standard deviation, $\sigma \sim 0.66$. The log-normal distribution type of $\boldsymbol{f}$ is consistent with §3.6.2 [Fig. 3.21]. A gamma distribution fits the histogram of $\boldsymbol{s}$, shown in red. Through the fit we found out that the shape and scale parameters (usually denoted by k and θ [??]) are 2.36 and 0.37

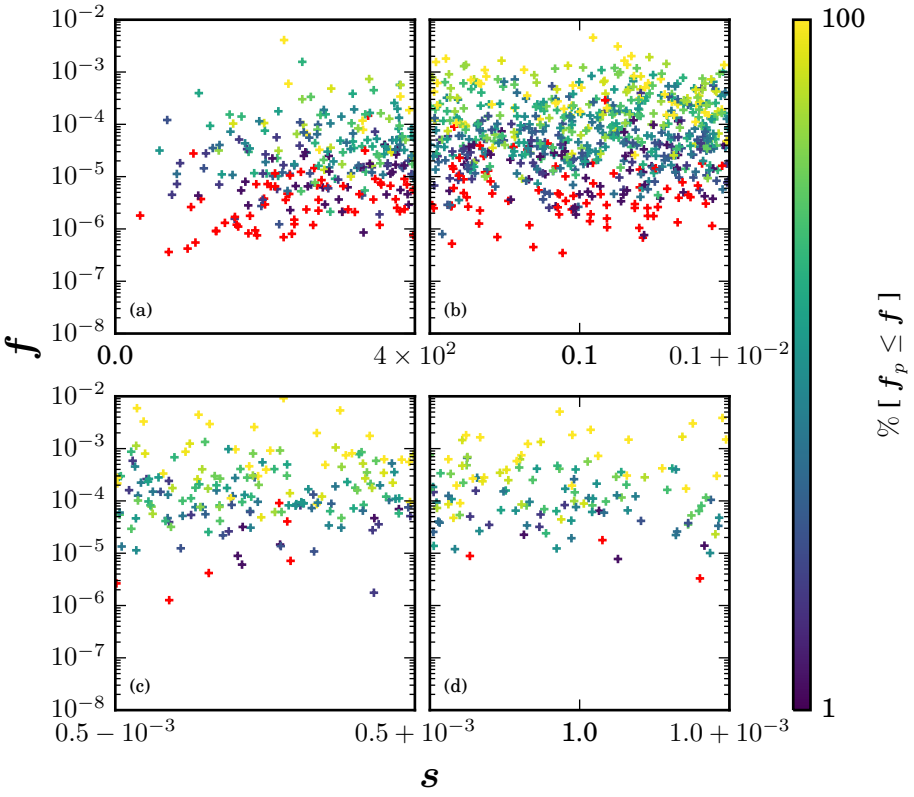

Figure 3.33: Quality of final solutions measured through the percentage of negative perturbations (see colorbar) for (a) $\boldsymbol{s} \leq 0.04$, (b) $0.1\text{-}10^{-2} \leq \boldsymbol{s} \leq 0.1\text{+}10^{-2}$, (c) $0.5\text{-}10^{-3} \leq \boldsymbol{s} \leq 0.5\text{+}10^{-3}$, and (d) $1\text{-}10^{-3} \leq \boldsymbol{s} \leq 1\text{+}10^{-3}$. Red color is used to separately mark only those data points for which none out of the 500 perturbations were found to be negative, implying that such points are strong candidates for a true local minimum. The appearing shared *x-axis* tick label belong to the left figures.

respectively. We carried out a square-root transformation of $\boldsymbol{s}$ and found that the shape of histogram is well approximated by a normal distribution [Fig 1.32(b), inset], shown in red) with $\mu \sim 0.89$ and $\sigma \sim 0.29$.

We now investigate whether there is a correlation between the values of $\boldsymbol{f}$ and the fraction of negative perturbations across the different intervals

of the order parameter $\boldsymbol{s}$. We first select four intervals in $\boldsymbol{s}$: *(i)* $0.0 \geq \boldsymbol{s} \leq 0.04$, *(ii)* $0.1\text{-}10^{-2} \leq \boldsymbol{s} \leq 0.1{+}10^{-2}$, *(iii)* $0.5\text{-}10^{-3} \leq \boldsymbol{s} \leq 0.5{+}10^{-3}$, and *(iv)* $1\text{-}10^{-3} \leq \boldsymbol{s} \leq 1{+}10^{-3}$, and extract the solutions falling within that range. For each solution, we then repeat the previously explained procedure, i.e. perturbing the solutions by a fixed step-size ϵ in the n_{pert} directions. We choose $\epsilon = 10^{-3}$ and $n_{pert} = 500$. Due to a large number of points to check, this is done to half the computational time. We remind that previously we set n_{pert} to 1000. Primarily, we are interested to find out the percentage of negative perturbations, if none, we infer that particular solution as a local minimum

We show the results in Fig 3.33. There, the colorbar denotes the percentage of negative perturbations. In the scatter plot, color red is used to separately mark only those data points for which none out of the 500 perturbations were found negative. These points are prime candidates for true local minima.We draw several conclusions: *(i)* substantial fraction of local minima correspond to values of $\boldsymbol{f}$ of order 10^{-5} or less. This is consistent across the figures (a)-(d). The number of these points decrease with an increase in $\boldsymbol{s}$, and *(ii)* We observe an appreciable and systematic increase in the percentage of negative perturbations for solutions with increasing values of $\boldsymbol{f}$. In general solutions with lower $\boldsymbol{f}$ values have lower percentage of negative perturbations. For increasing values of $\boldsymbol{f}$, most solutions are not strict local minimum. Considering that our implementation of PSO only used a population size of 50, it is not surprising that such solutions are found when exploring a high dimensional search space.

Variability in $\boldsymbol{f_p}$ – For the data points shown in Fig. 3.33(a-d) grouped on the basis of $\boldsymbol{s}$, we measure the variability in $\boldsymbol{f}_p$ by calculating the values of coefficients of variation (CV), which measures how large is the standard deviation with respect to the mean. This we do because of large scales of difference across the values of $\boldsymbol{f}$ and therefore the mean values of $\boldsymbol{f}_p$. Essentially, we expect that the solutions representing minimum or near-minimum should have higher values of $CV(\boldsymbol{f}_p)$ than the solutions that do not. We report the results in Fig. 3.34. There, the data sets in (a)-(d) are the same as previously categorized based on the value of $\boldsymbol{s}$ in Fig. 3.33. The color-code of the data points is also same. We observe significant differences in the values of $CV(\boldsymbol{f}_p)$. Typically, across $\boldsymbol{s}$, the values are lower for data points that are not local minima than the ones that are more likely to be.

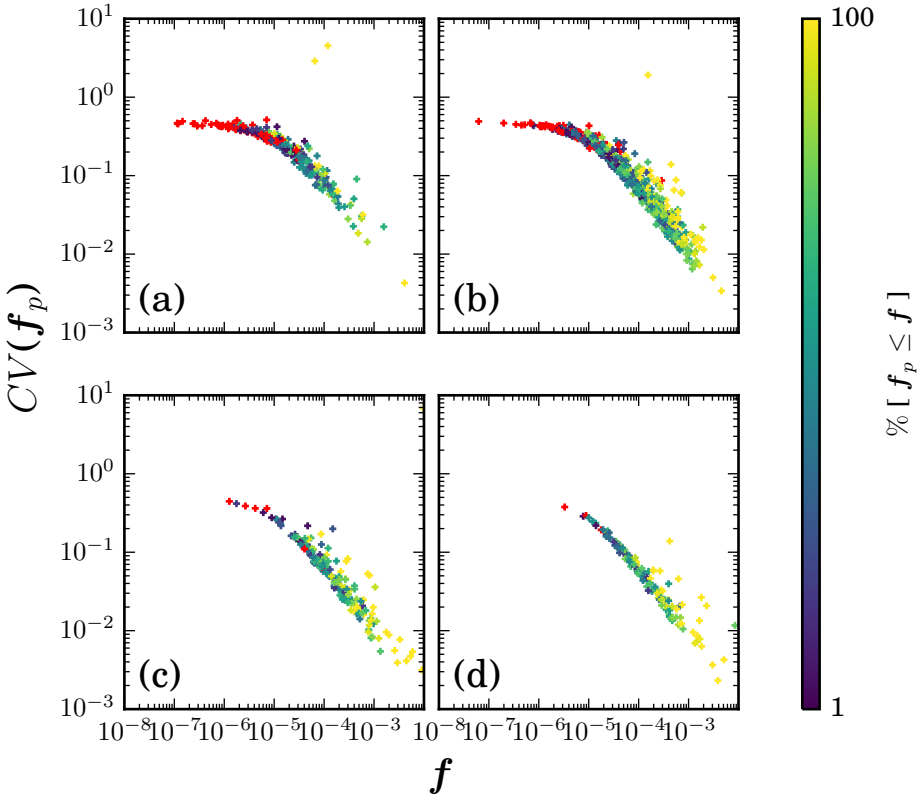

Figure 3.34: For the same data in Fig. 3.33(a-d) grouped on the basis of $\boldsymbol{s}$, $CV(\boldsymbol{f}_p)$ vs $\boldsymbol{f}$. We observe that across all the four intervals of $\boldsymbol{s}$, the values of $CV(\boldsymbol{f}_p)$ are lower for the data points that are not local minimum than the ones that are more likely to be.

Additionally, we notice that $CV(\boldsymbol{f}_p)$ for these two groups of data points follow different power law relations.

3.9 A Proof of Concept with 3D Printing

In this section, we present 3D printed flexible unit cells and tilings based on the computer-designed mechanisms. 3D printing begins with the creation of a 3D CAD design of the mechanisms in CAD software. While doing this,

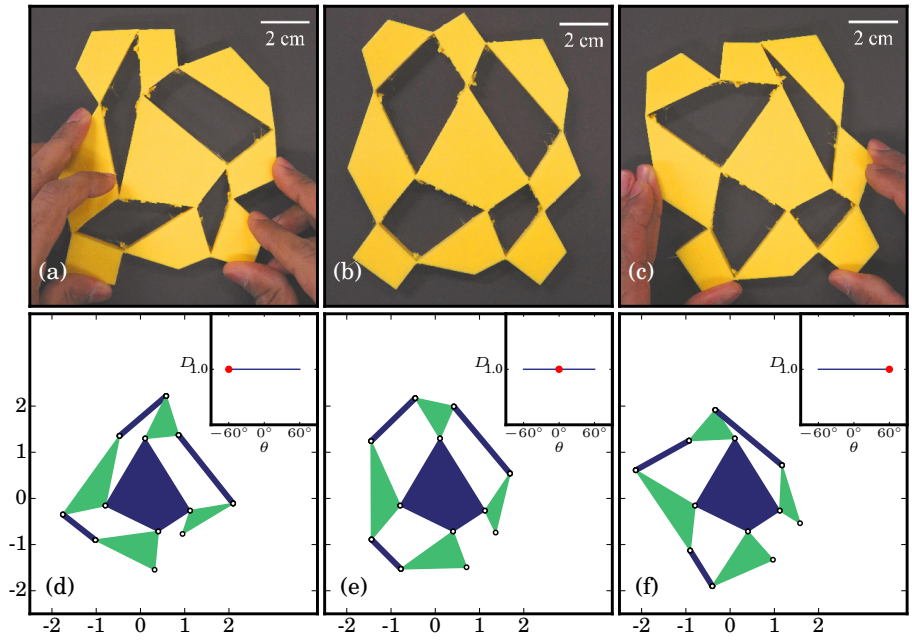

Figure 3.35: A 3D printed flexible unit cell in the states of (a) $\theta = -60°$, (b) $\theta = 0°$ and (c) $\theta = 60°$ of the base mechanism, which is shown in these states in (d-f) respectively. Inset shows the theoretical $D(\theta)$ curve. We observe good agreements between experiments and simulations, thus successfully modeling the soft deformation mode.

we pay special attention to the connecting-hinge thickness and keep it to a small value, determined by the resolution of the printer. These designs are then fed to a printer, which builds up a three-dimensional object by successively adding the printing material layer by layer. We use an elastic material for 3D printing, known by its commercial name *Filaflex* and print it with our *Felix Pro 1* printer.

3.9.1 Unit Cells

The design of a 3x3 flexible unit cell is simple to create. We start from a *precursor* mechanism generated by PSO in the neutral state ($\theta = 0°$) and complete the 3x3 network by 'fitting-in' the 'missing' polygon P_9 [Fig.

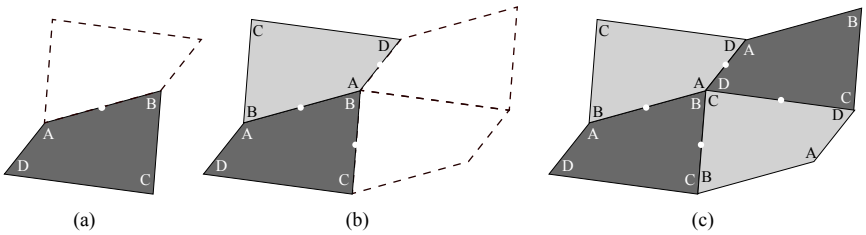

Figure 3.36: Quadrilaterals (simple) tessellate the plane.

3.12], joining the polygons P_6 and P_8. The corresponding edge length of P_9 being 1.0. The polygonal shape of the rigid elements at the *boundary* of the unit cell is not specified by the design, and we augment the shape of each element to a quadrilateral. This is done such that the quadrilaterals at the boundary do not collide throughout the internal hinging motion within the range of interest. In order to mimic the low energy deformation mode, we keep the designed minimum thickness of the connections joining two quadrilaterals together to be ≈ 0.45 mm. The resolution of our printer is ≈ 0.40 mm. Note that the final 3D printed samples have connections with thickness slightly greater than ≈ 0.45 mm.

An example of a 3D printed unit cell is shown in Fig. 3.35(b). There the scale of the sample is labeled. The out-of-plane thickness of the sample is ≈ 10 mm. The precursor mechanism is shown in the figure (e). The value of $\boldsymbol{f}$ is 4.5×10^{-7}. Fig. 3.35(a),(c) show the sample deformed in the $\theta = -60^\circ$ and $\theta = 60^\circ$ states, which are shown in the figure (d),(f) for the base mechanism. We observe a good agreement between the deformation patterns of 3D printed sample and the underlying mechanism.

3.9.2 Metatilings

We demonstrate a strategy to tile any arbitrary flexible unit cell into a regular tessellation, while preserving the internal soft mode. Firs, we note that any simple quadrilateral tesselates the plane [Fig. 3.36]. To obtain quadrilaterals, we augment the bar linkages P_1, P_3, P_7 and P_9 of the unit cell into triangles [Fig. 3.37(a,b)], whose free vertices form a virtual quadrilateral boundary. We then create a regular tesselation of this *augmented unit cell* by tiling it.The extreme deformed states of the tesselation i.e. $\theta = -60^\circ$ and $\theta = 60^\circ$ are shown in Fig. 3.37(c,d) respectively. Clearly, the tesselation retains

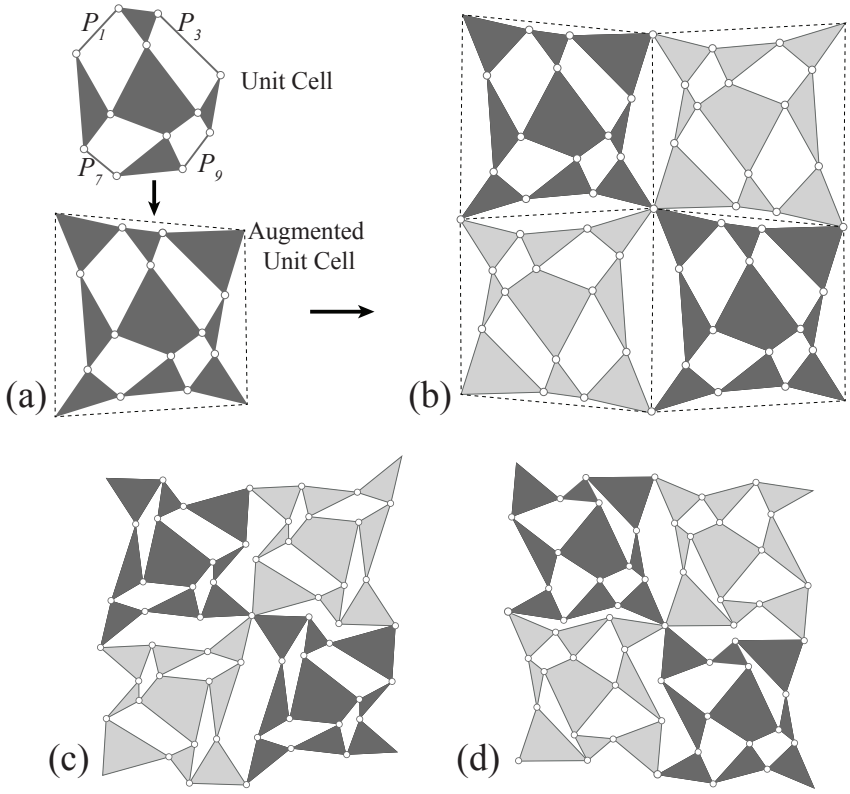

Figure 3.37: A general procedure to tile an arbitrary flexible 3x3 unit cell into a periodic tesselation, that we call a *Metatiling*. Note that the unit cell shown in this example is the same as in Fig. 3.35(b). We augment a 3x3 unit cell by transforming the bar linkages (labeled P_1, P_3, P_7 and P_9) into triangular elements. The virtual edges connecting the free corners of the augmented unit cell are shown in dashed lines. These edges form a quadrilateral tile. (b) A periodic tesselation consisting of the 3x3 augmented unit cell and copies rotated by 180° in-plane (shown in a lighter shade). The deformed states of the metatiling corresponding to: (c) $\theta = -60°$ and (d) $\theta = 60°$ configurations of the unit cell.

the deformation modes of its unit cell. We call such flexible tesselations *metatilings*.

By following this procedure, we design the metatiling of the unit cell

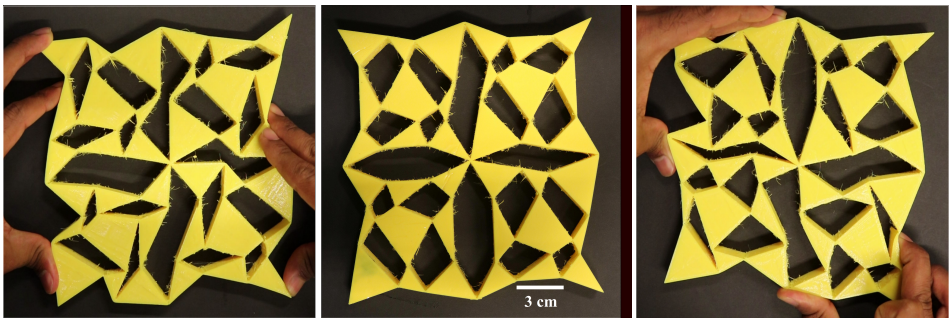

(a) **(b)** **(c)**

Figure 3.38: 3D printed metatiling of the unit cell shown in Fig. 3.35. The metatiling in its neutral state is in (b). In (a, c), we show the extreme deformed states of it, respectively, in which, the internal unit cell is at the $\theta = -60°$ and $\theta = 60°$ configurations. We can observe that the deformations in the real sample closely conform the ideal scenario [Fig. 3.37(c,d)].

shown in Fig. 3.35 and 3D print it. The tiling in the neutral state is shown in Fig. 3.38(b). The length scale of the sample is labeled. The designed thickness the sample (plane-normal) is 10 mm. The extreme deformed states are shown in Fig. 3.40(a,c). We observe a decent agreement with the deformed states expected for ideal hinges [Fig. 3.37(c,d)]

3.10 Discussion and Conclusion

In this chapter, we demonstrated an optimization-based methodology to design small generic yet flexible systems that exhibit low-energy deformations. The main strategy is to optimize the design of the underlying mechanism such that a curve that characterizes the internal motion, the $D(\theta)$ curve [§3.1] matches the desired target response $D_t(\theta)$. We began with formulating the optimization problem with the aim of obtaining a mathematical definition for the objective function in terms of the design variables that includes the penalized constraint handling as well [§3.4], and employed PSO to optimize for $D_t(\theta)$ [§3.5].

We focused on the optimal parameter setting of PSO in §3.6 and showed the effect of the parameters (ω, c_1, c_2) on the search behavior and distribution of the final solutions. In particular, we found out that for the current

problem, at $\omega = 0.25$, high values of c_2 and low values of c_1 are conditional [Eq. 3.29, §3.6.1], with the best-performing (c_1, c_2) set displaying a vertical downward shift with an increase in ω. We then demonstrated that the best-performing (c_1, c_2) set results in a log-normal distribution of the final solutions, whereas the worst-performing set results in a normal distribution [§3.6.2].

In §3.7, we utilized Sammon's mapping in order to effectively reduce the dimensionality of the search space from 24 dimensions and map the candidate solutions onto a 2D plane. The visualization of PSO done in this manner assisted us in verifying the main arguments of §3.6.1: suboptimal (c_1, c_2) settings can lead to premature convergence, divergence or no convergence at all, whereas correct settings impart a much higher global search capability to PSO.

In the main results section [§3.8], we showed the optimized designs and found a huge diversity in terms of the distinct possible solutions that satisfy our target criteria and are still generic, although we observe that the quality of solutions suffers as the genericness of the solutions increases (§3.8.2). We characterized PSO and showed that a 'good' PSO search results in the swarm particles getting trapped inside a deep local minimum while this is not the case with a 'bad' search (§3.8.1).

Finally in §3.9, we bring these computer designed structures to real life through 3D printing with flexible material and slender connections. We are able to closely model the ideal low-energy deformation mode. Additionally, we showed how to tile these flexible unit cells into a regular tessellation while retaining the original soft-mode.

Acknowledgments

The large batch of PSO simulations were performed availing the high-performance computing facilities offered by SURFsara, Amsterdam. We are especially thankful for their excellent technical support to facilitate efficient computing and data transfer. The work presented in this chapter is part of an industrial partnership programme (IPP) *'Computational Sciences for Energy Research (CSER)'* started in 2012, and funded by the Shell Global Solutions International B.V., the Netherlands Organization for Scientific Research (NWO) and the Foundation for Fundamental Research on Matter (FOM).

Chapter 4

Rational Design of Multi-stable 2D Mechanical Metamaterials

Abstract – Moving beyond the constant target $D_t(\theta)$ curves, in this chapter, we investigate the design of precursor eight-polygon mechanisms [Fig. 3.4] optimizing for non-constant $D_t(\theta)$ curves with the ultimate aim of designing 2D multi-stable mechanical metamaterials. We begin with systematically categorizing the new $D_t(\theta)$ curves into four families of increasing complexity which include both linear and trigonometric functions (of θ). We then statistically measure the performance of PSO on each one of them and establish that within the non-linear $D_t(\theta)$ curve families, the solution quality drops with an increase in the magnitude of variation of D with θ, whereas it remains unaffected for the linear curves; and among these families, the solution quality suffers substantially with an increase in the number of extrema in the $D(\theta)$ curve. We fabricate these computer-designed bi-stable and tri-stable unit cells using 3D printing and confirm the shape-shifting behavior experimentally. Finally, we tile copies of these unit cells and observe multi-stable behavior as well.

4.1 Introduction

Shape-transforming ability of a structural material catches the natural attention of the onlooker. Importantly, such materials offer many promising applications as practical deployable structures, which can be externally activated when required to morph from one shape to another. Shape-transformable materials is an active area of research. A faction of mechanical metamaterials researchers have observed and reported several different instances of shape-transformable reconfigurable devices [16, 34, 36, 104, 105]. In this chapter, we further expand the horizons of this subject area into a fresh direction.

We mentioned in the previous chapter (§3.1) that the trajectory of the characteristic curve $D(\theta)$ of the eight-polygon mechanism [Fig. 3.4] can be manipulated such that the resulting 3x3 unit cells (consisting of rigid units connected together with soft-deformable hinges) are multi-stable. In the current chapter, we explore this very case, where chiefly we utilize PSO to optimize the mechanism design for non-constant target $D_t(\theta)$ curves of our interest. We set out with the following two primary aims. *(i)* Correlate the search capability of PSO to find good-quality approximate solutions (mechanism designs) for the non-constant $D_t(\theta)$ functions versus their complexity, and *(ii)* utilize these computer-designed mechanisms to fabricate 2D shape-shifting structures. While doing so, we simultaneously put to test a key feature which reflects the robustness of an automated inverse strategy for material design. This is the ability to output optimal structural design for multiple target criteria with minimum alternations in basic construction of the model.

The outline of this chapter is as follows. In the immediate discussion below, we define our new target curves of varying levels of general complexity. Depending upon the number of extrema in the curves, we broadly categorize them into four families. We then briefly mention about the details involving the implementation of PSO and the method for generating large solution ensemble for a particular target curve. In §4.2, we quantify the performance of PSO across these curves and compare the average solution quality. One would presume an increase in the difficulty for PSO to find good quality solutions as the complexity of the target curves increases. We statistically confirm that this is indeed the case. Mechanisms with complex nonlinear $D(\theta)$ response require large internal deformations, which is typically hard to

accomplish without violating the imposed constraints on the system. In §4.3, we show the actual computer-designed mechanisms. Finally, in §4.4, we build bi-stable and tri-stable unit cells and some tilings comprising of them on top of the designed mechanisms, and fabricate them via 3D printing, thus practically establishing novel examples of shape-transformable mechanical metamaterials.

Target curves, $D_t(\theta)$ – We begin our analysis by first systematically categorizing the new target $D_t(\theta)$ functions. Broadly, we divide the curves into four *families*: $\mathcal{F}_1$, $\mathcal{F}_2$, $\mathcal{F}_3$, and $\mathcal{F}_4$. The $\mathcal{F}_1$ curves are linear with varying slopes, while $\mathcal{F}_2$, $\mathcal{F}_3$ and $\mathcal{F}_4$ curves are trigonometric, with an increased complexity from $\mathcal{F}_2$ to $\mathcal{F}_4$. For all the families, we fix $D_t(0°) = 1$ and consider twenty different values of an adjustable parameter α, thereby having twenty curves for each family.

The general mathematical form for the $\mathcal{F}_1$ curves is: $D = 1 + \alpha\theta$, where the parameter α controls the slope. θ is measured in radians and we cover a total range from -$\pi/3$ to $\pi/3$. α takes on the values $\pm$ 0.05, 0.10. . . . .0.50. In the similar fashion, we constructed the $D_t(\theta)$ curves for the rest of the three families, whose general trigonometric forms in terms of α and θ are given as: $\mathcal{F}_2$: $D = 1 + \alpha\sin(2\theta + \pi/2)$; $\mathcal{F}_3$: $D = 1 + \alpha\sin(3\theta + \pi/2)$ and $\mathcal{F}_4$: $D = 1 + \alpha\sin(4\theta)$. The $\mathcal{F}_1$ - $\mathcal{F}_4$ curves are shown in Fig. 4.1, where the curves with positive values of α are shown in solid and the curves with negative values of α are shown in dashed. The colorbar on the right indicates the magnitude of α. By optimizing for these set of target curves, we aim to learn about the performance of PSO at least within a certain domain of complex $D_t(\theta)$ curves. With the correct dimension of the missing polygon which closes down the 3x3 network, $\mathcal{F}_1$, $\{\mathcal{F}_2, \mathcal{F}_3\}$ and $\mathcal{F}_4$ curves can lead to the creation of deformable mechanical metamaterials consisting of soft connectors that are monostable, bi-stable and tri-stable respectively. As we will discuss, when we show the actual 3D printed samples, achieving multi-stability for these systems is dependent on the hinge elasticity, which we tune by controlling their geometry.

PSO simulations – We prescribed the above-mentioned target $D_t(\theta)$ curves to our design framework and ran the PSO algorithm. The complete implementation details of PSO, which includes the definition of design variables and objective function $\boldsymbol{f}$, size of the swarm and its initialization,

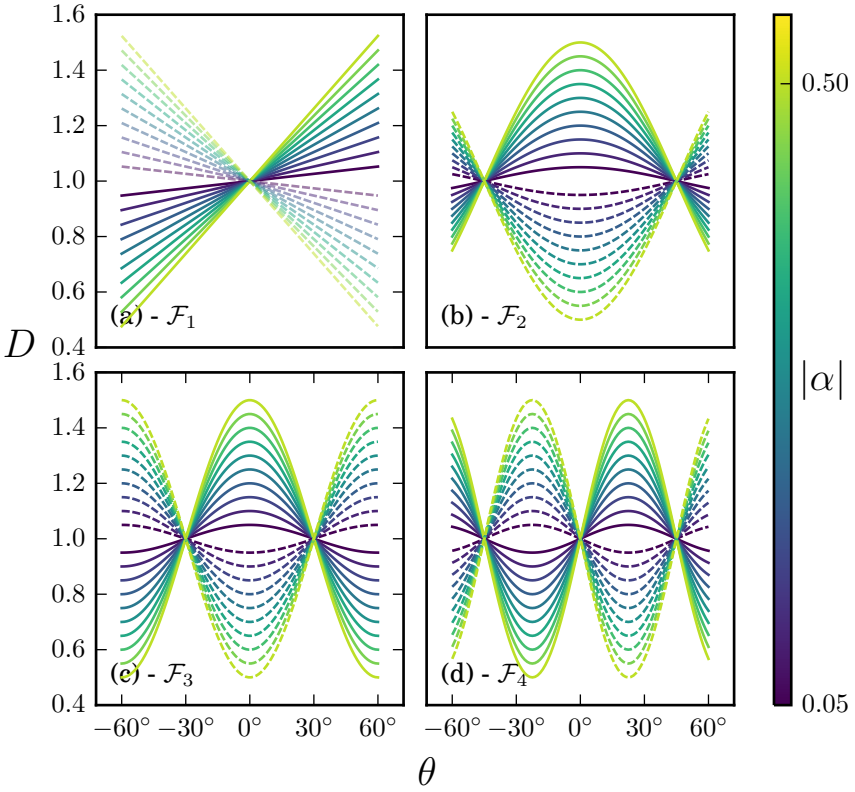

Figure 4.1: Families of the new target curves $D_t(\theta)$ denoted by the symbols: (a) $\mathcal{F}_1$, (b) $\mathcal{F}_2$, (c) $\mathcal{F}_3$ and (d) $\mathcal{F}_4$. The general mathematical formula of the curves are as follows. $\mathcal{F}_1$: $D = 1 + \alpha\theta$; $\mathcal{F}_2$: $D = 1 + \alpha\sin(2\theta + \pi/2)$; $\mathcal{F}_3$: $D = 1 + \alpha\sin(3\theta + \pi/2)$ and $\mathcal{F}_4$: $D = 1 + \alpha\sin(4\theta)$. α takes on twenty different values i.e. $\pm$ 0.05, 0.10. . . . .0.50. $D(\theta)$ curves for the positive values of α are shown in the solid curves and for negative values of α are shown in the dashed curves, and are color-coded according to the magnitude of α (see colorbar).

and the termination criteria are the same as described in the previous chapter in §3.5. It should be noted that: *(i)* we rule out the effects of the distribution of the initial population by using the exact same initial population as the one used in the previous chapter for constant $D_t(\theta)$ curve, and *(ii)* we ran

PSO with $\omega = 0.25$ and the best-performing (c_1, c_2) parameter settings, which were given by Eq. (3.29) in the previous chapter. We do this to ensure that we generate a large number of good quality solutions. One might wonder whether these parameter settings are still optimal for the new $D_t(\theta)$ curves. By performing hyperparameter optimization in the similar manner as described previously in §3.6.1, we verified that this generally is true, although depending upon the type of the $D_t(\theta)$ curve, the scales of $\boldsymbol{f}$ may vary. In order to avoid repetition, we refrain from showing the heatmaps. For each of the 36 different (c_1, c_2) parameter pairs, data was gathered for 500 independent PSO simulations. Accordingly, for any given $D_t(\theta)$ curve, we have 1.8×10^4 potential solutions to statistically quantify the performance of PSO.

4.2 Characterizing the Performance of PSO

We would now quantify the performance of PSO for the above-defined $D_t(\theta)$ curves [Fig. 4.1]. For each family $\mathcal{F}_1$-$\mathcal{F}_4$ and separately for positive and negative α values, we characterize the performance via *(i)* a scatter plot of the best solution objective function value $\boldsymbol{f}$ versus the order parameter $\boldsymbol{s}$ for two extreme magnitudes of α i.e. $|\alpha| = 0.05$ and $|\alpha| = 0.50$, and *(ii)* probability density functions (PDFs) of $\boldsymbol{f}$ for all the α values. Of course, the definition for $\boldsymbol{s}$ is also the same as defined in the previous chapter [Eq. (3.38)]. In this manner, by comparing the typical scales of $\boldsymbol{f}$, we can correlate the performance of PSO with the complexity of the target curves. We summarize our results in Fig. 4.2-4.5 for the four respective families $\mathcal{F}_1$-$\mathcal{F}_4$. There, within each figure, we show the $\boldsymbol{f}$ vs $\boldsymbol{s}$ scatter plots for $\alpha =$ 0.05 and $\alpha = 0.50$ in figure (a),(b) respectively, the PDFs for all the positive α values in figure (c), the $\boldsymbol{f}$ vs $\boldsymbol{s}$ scatter plots for $\alpha =$ -0.05 and $\alpha =$ -0.50 in figure (d),(e) respectively, and the PDFs for all the negative α values in figure (f). The colors of the PDFs represent α values and are based on the colorbar shown in Fig. 4.1.

$\boldsymbol{f}$ vs $\boldsymbol{s}$ scatter plots – We first summarize the following three visually noticeable trends comparing the scatter plots intra-family wise. *(i)* For $\mathcal{F}_1$ curves, taking only the scales of $\boldsymbol{f}$ into consideration, we do not see any appreciable differences in the scatter plots for $|\alpha| = 0.50$ compared with $|\alpha|$ $= 0.05$. *(ii)* For rest of the three families, we observe a significant collective

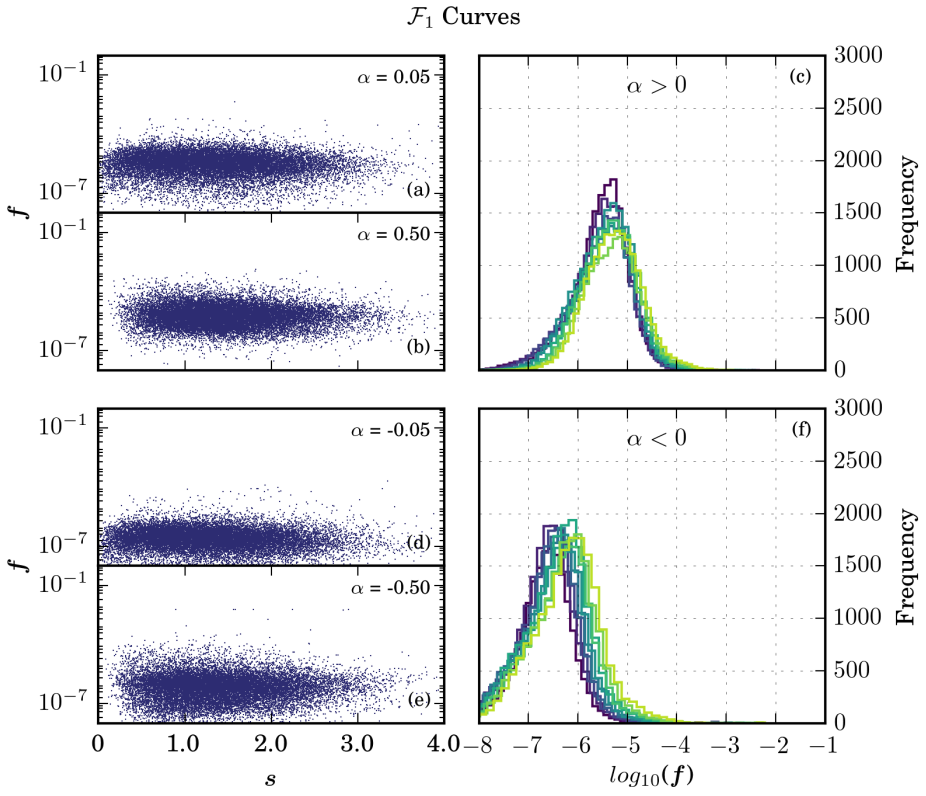

Figure 4.2: Statistics summarizing how the PSO performed over $\mathcal{F}_1$ target curves [Fig. 4.1(a)]. For each of the member $D_t(\theta)$ curve, we performed 1.8×10^4 independent PSO runs. (a) objective function $\boldsymbol{f}$ vs order-parameter $\boldsymbol{s}$ scatter plot for $\alpha = 0.05$, (b) $\boldsymbol{f}$ vs $\boldsymbol{s}$ scatter plot for $\alpha = 0.50$, and (c) probability density functions (PDFs) of $\boldsymbol{f}$ for $\alpha = 0.05, 0.10, \ldots\ldots 0.50$. The PDFs for different α values are colored differently and are based on the colorbar shown in Fig. 4.1. (d, e) Corresponding $\boldsymbol{f}$ vs $\boldsymbol{s}$ scatter plots for α = -0.05 and α = -0.50, and (f) PDFs of $\boldsymbol{f}$ for negative α values. We preserve same definitions for both $\boldsymbol{f}$ and $\boldsymbol{s}$ as in the previous chapter.

upwards vertical shift in the 'cloud' of points . This is not surprising: we expect that it becomes harder for PSO to discover good quality solutions as the magnitude of variation in D (with θ) increases. As mentioned before, one

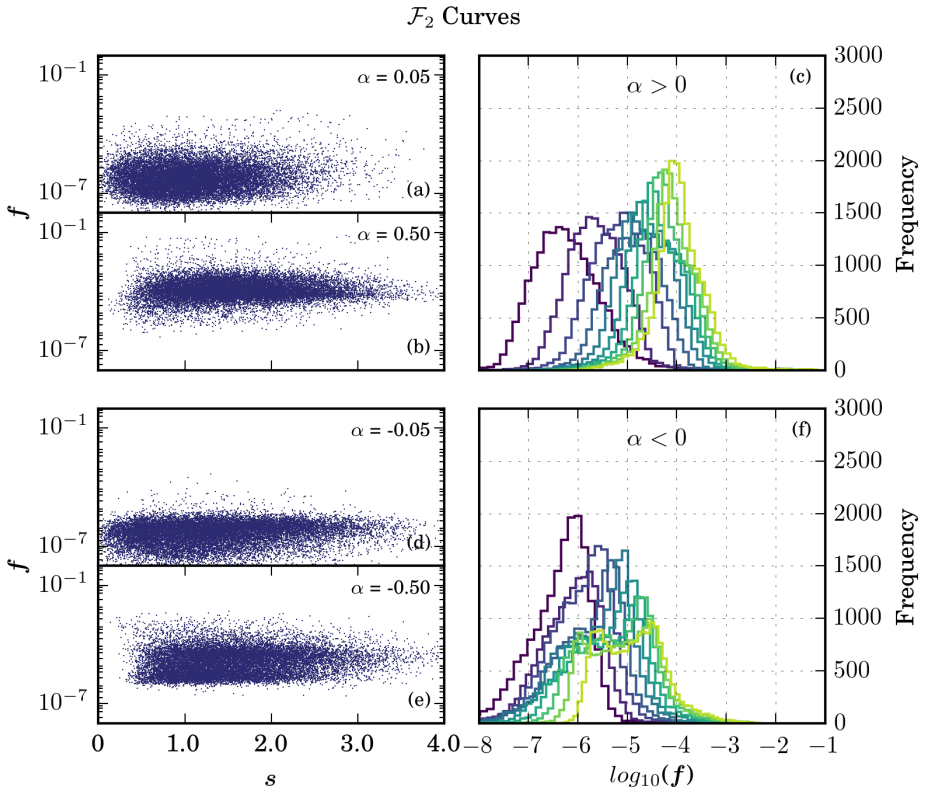

Figure 4.3: Statistics summarizing how the PSO performed over $\mathcal{F}_2$ target curves [Fig. 4.1(b)]. (a) objective function $\boldsymbol{f}$ vs order-parameter $\boldsymbol{s}$ scatter plot for $\alpha = 0.05$, (b) $\boldsymbol{f}$ vs $\boldsymbol{s}$ scatter plot for $\alpha = 0.50$, and (c) probability density functions (PDFs) of $\boldsymbol{f}$ for $\alpha = 0.05, 0.10, \ldots\ldots 0.50$. The PDFs for different α values are colored differently and are based on the colorbar shown in Fig. 4.1. (d, e) Corresponding $\boldsymbol{f}$ vs $\boldsymbol{s}$ scatter plots for α = -0.05 and α = -0.50, and (f) PDFs of $\boldsymbol{f}$ for negative α values.

likely reason could be that the mechanisms corresponding to these solutions require to have complex internal deformations, which is typically hard to accomplish without violating the imposed constraints on the system (§3.4.2). *(iii)* Within the families, for $|\alpha|$ =0.50, we observe a rather scant number of solutions having low $\boldsymbol{s}$ values when compared with$|\alpha|$ =0.05. Clearly,

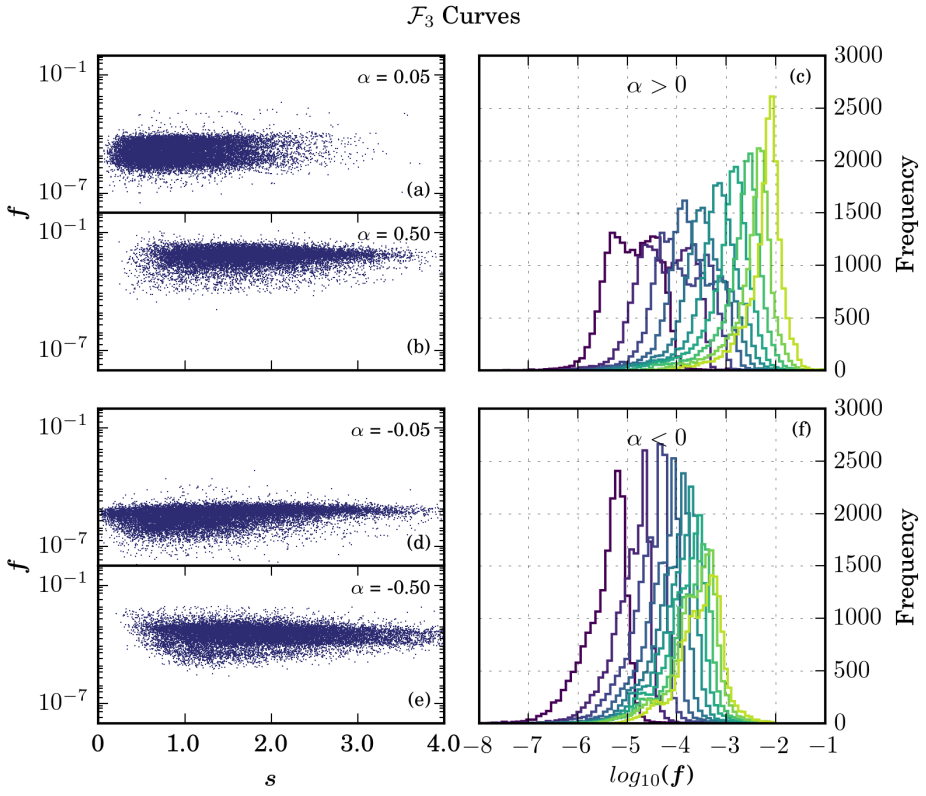

Figure 4.4: Statistics summarizing how the PSO performed over $\mathcal{F}_3$ target curves [Fig. 4.1(c)]. (a) objective function $\boldsymbol{f}$ vs order-parameter $\boldsymbol{s}$ scatter plot for $\alpha = 0.05$, (b) $\boldsymbol{f}$ vs $\boldsymbol{s}$ scatter plot for $\alpha = 0.50$, and (c) probability density functions (PDFs) of $\boldsymbol{f}$ for $\alpha = 0.05, 0.10, \ldots\ldots 0.50$. The PDFs for different α values are colored differently and are based on the colorbar shown in Fig. 4.1. (d, e) Corresponding $\boldsymbol{f}$ vs $\boldsymbol{s}$ scatter plots for α = -0.05 and α = -0.50, and (f) PDFs of $\boldsymbol{f}$ for negative α values.

discovering mechanisms that are capable of accomplishing complex internal deformation forces PSO to find solutions where linkages deviate significantly from the parallelogram linkages. Comparing the scatter plots among the families for extreme curves i.e. $|\alpha|$ =0.50 reveals that the points shift upwards, suggesting an increase in the general scales of $\boldsymbol{f}$. The performance

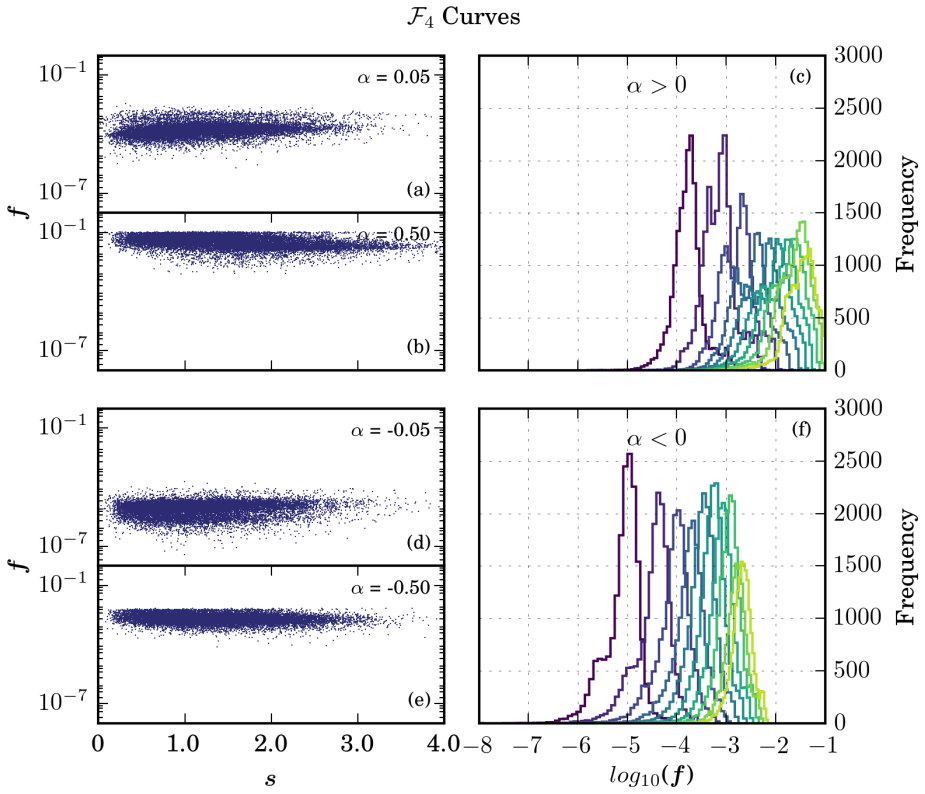

Figure 4.5: Statistics summarizing how the PSO performed over $\mathcal{F}_4$ target curves [Fig. 4.1(d)]. (a) objective function $\boldsymbol{f}$ vs order-parameter $\boldsymbol{s}$ scatter plot for $\alpha = 0.05$, (b) $\boldsymbol{f}$ vs $\boldsymbol{s}$ scatter plot for $\alpha = 0.50$, and (c) probability density functions (PDFs) of $\boldsymbol{f}$ for $\alpha = 0.05, 0.10, \ldots\ldots 0.50$. The PDFs for different α values are colored differently and are based on the colorbar shown in Fig. 4.1. (d, e) Corresponding $\boldsymbol{f}$ vs $\boldsymbol{s}$ scatter plots for α = -0.05 and α = -0.50, and (f) PDFs of $\boldsymbol{f}$ for negative α values.

of PSO suffers remarkably. We expected this as the general complexity increases from $\mathcal{F}_1$-$\mathcal{F}_4$.

Probability density functions of $\boldsymbol{f}$ − We now take a look at the distributions of $\boldsymbol{f}$. Fig. 4.2(c) shows the PDFs of $\boldsymbol{f}$ for positive α values $\mathcal{F}_1$

curves. We chose 50 bins of equal width to group the data. The functions for different α values are colored differently and are based on the colorbar shown in Fig. 4.1. Barring a slight shift towards the right as α is increased, the PDFs appear to be suitably similar. The shape of these PDFs appears to be bell-shaped suggesting that $\boldsymbol{f}$ is log-normally distributed. Fig. 4.2(f) shows the PDFs of $\boldsymbol{f}$ for negative values of α. Compared to the positive α values, the PDFs are only slightly right-shifted. Still, overall we obtain very similar results for both positive and negative α values. Mainly, our results show that PSO performs extremely well over all the linear $D_t(\theta)$ curves, irrespective of their slopes. We hypothesize that this could be due to the *uniform dispersion* of potential solutions in the search space - generally the 3x3 systems are rigid (§3.1), thereby leading to quite a high possibility that these linear target curves are well approximated.

Fig. 4.3(c,f) shows the PDFs of $\boldsymbol{f}$ for $\mathcal{F}_2$ curves. We obtain a variety of shapes of the PDFs. For low and positive values of α, we observe a right-skewness in the distribution with an off-centered peak towards the left and a tail stretching away from it. The skewness in the distributions decreases and peakedness increases as the magnitude of α increases. For negative values of α, however, we obtain a slight left-skewed distribution for lower magnitudes of α and a mixed bimodal distribution for higher magnitudes. The heterogeneity in the shapes of the PDFs can also be observed for the families $\mathcal{F}_3$ and $\mathcal{F}_4$ curves. These PDFs remarkably differ from one another and clearly lack any general trend, apart from: *(i)* the expected shift towards higher scales of $\boldsymbol{f}$ for increasing magnitudes of α, and *(ii)* the appearance of bimodal mixed distribution for several successive values of α. For example, in $\mathcal{F}_3$ curves, we observe mixed distribution for low and positive, and high and negative values of α. In the case of $\mathcal{F}_4$ curves, although minute, we obtained mixed distribution for all the values of α. A possible explanation for the existence of mixed distributions is as follows: a highly constrained optimization problem has well-separated regions of feasible search space i.e. where no constraint is violated and unfeasible search space. The degree of their separation is problem dependent, which in our case is the type of the target curve to be met. We conjecture that for some of these target curves, it may so be the case that the objective function landscape is *patchy* in the sense that some regions of feasible search space are favored over others. The inherent capability of PSO and a possible uneven dispersal of solutions might further accentuate the preference for search regions. The collective

result can be the final mixed distributions that we see.

4.3 Optimized Mechanisms

We will now show examples of optimized mechanisms for the four families. We show these examples only for the extreme values of α i.e. $|\alpha| = 0.50$. This we do so keeping sight of the final purpose, which is to be able to fabricate bi-stable and tri-stable samples. When multi-stable samples like these are deformed, the hinges stretch and twist. The stretching energy releases itself when the samples reach the stable states, where only the torsional energy is present. In total, the stretching energy serves as an energy barrier that stops the sample from 'flipping back' to the initial state. By aiming for the extreme examples, where $D(\theta)$ curves have a large variation, we hope to be able to set large enough energy barrier that compensates for the torsional energy present in the hinges.

For families $\mathcal{F}_1$-$\mathcal{F}_4$, $\alpha = 0.50$, we sort out six example mechanisms on the basis of least value of the objective function $\boldsymbol{f}$ and show them in Fig. 4.6. In terms of geometry of the mechanisms, we obtain highly diverse designs. We notice that except for the $\mathcal{F}_1$ curve, the mechanisms for the rest of the curves display a common feature, which is the presence of one (or even two) *narrow convex linkages*. These linkages appear in the shape of *kites* with two pairs of almost-equilength adjacent bars. The presence of these linkages provides an easy path to achieve large internal deformations for the mechanism: the linkage further 'closes down' and completely folds within itself for one extreme value of θ while 'opens up' like a normal linkage towards the other extreme. We demonstrate it on the example shown in Fig. 4.6(g) by showing its extreme deformed states in Fig. 4.8, where the figures (a), (b) and (c) show the mechanism in the deformed states of $\theta = -60°$, $0°$ and $60°$ respectively. The value of $\boldsymbol{f}$ is 4.75×10^{-7}. From the search point of view, we propose one possible explanation for the frequent findings of mechanisms consisting of such linkages by PSO: static penalization method introduced in the previous chapter to penalize systems displaying self-intersection among neighboring polygons (§3.4.2) may lead to the formation of steep boundaries between feasible and unfeasible search regions, that are hard to overcome, thereby forcing PSO to find solutions that are 'near' the *constraint boundary*. For $\mathcal{F}_2$ and $\mathcal{F}_3$, we find several mechanisms on difference scales of workable values of $\boldsymbol{f}$, that do not have

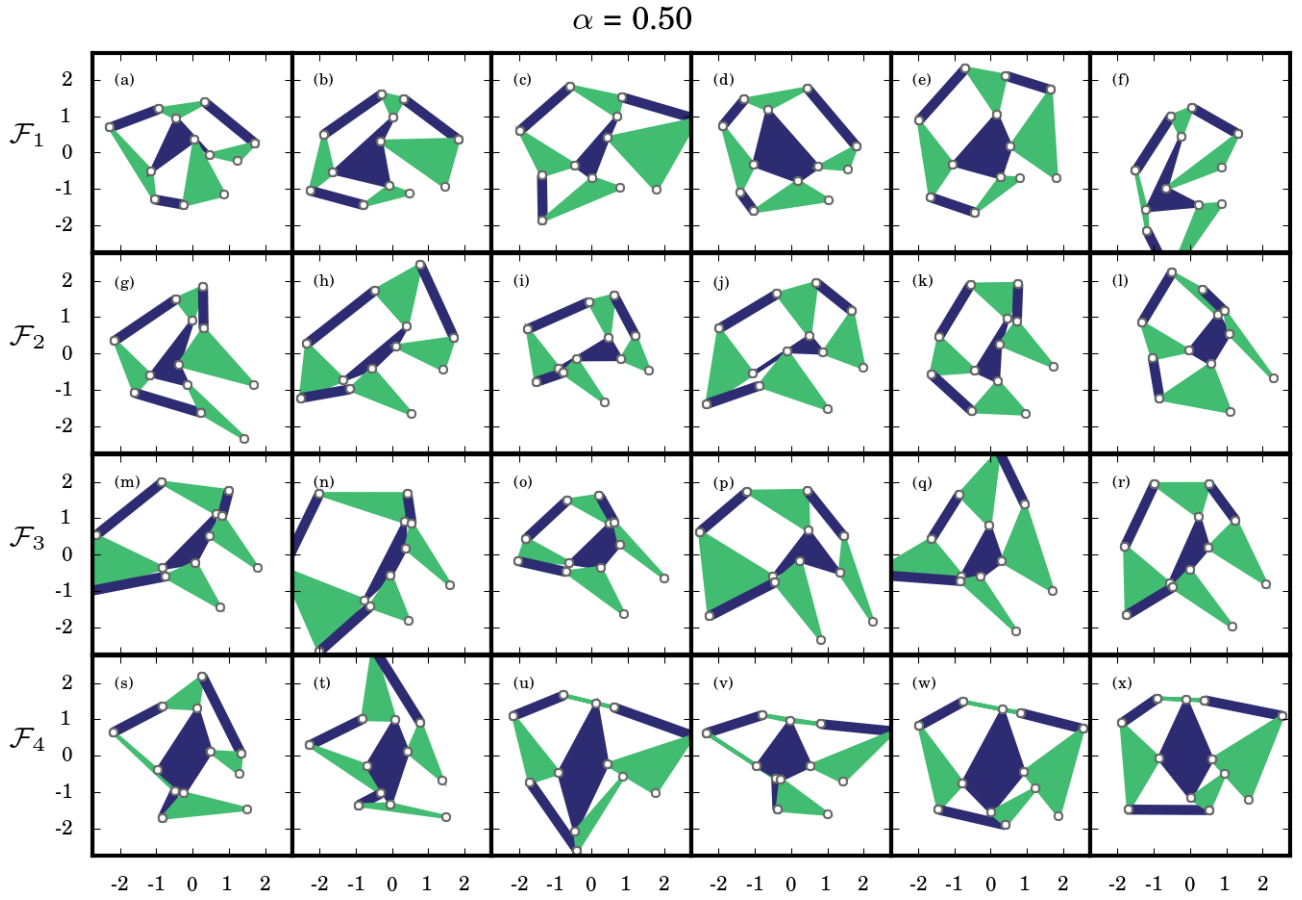

Figure 4.6: A gallery of low $\boldsymbol{f}$ solutions for the $D_t(\theta)$ curves $\mathcal{F}_1$-$\mathcal{F}_4$, $\alpha = 0.50$. Each row corresponds to a different family (labeled). $\boldsymbol{f}$ is of the order of: 10^{-8} or less for $\mathcal{F}_1$, 10^{-7} or less for $\mathcal{F}_2$, 10^{-5} for $\mathcal{F}_3$ and 10^{-3} or less for $\mathcal{F}_4$ curve.

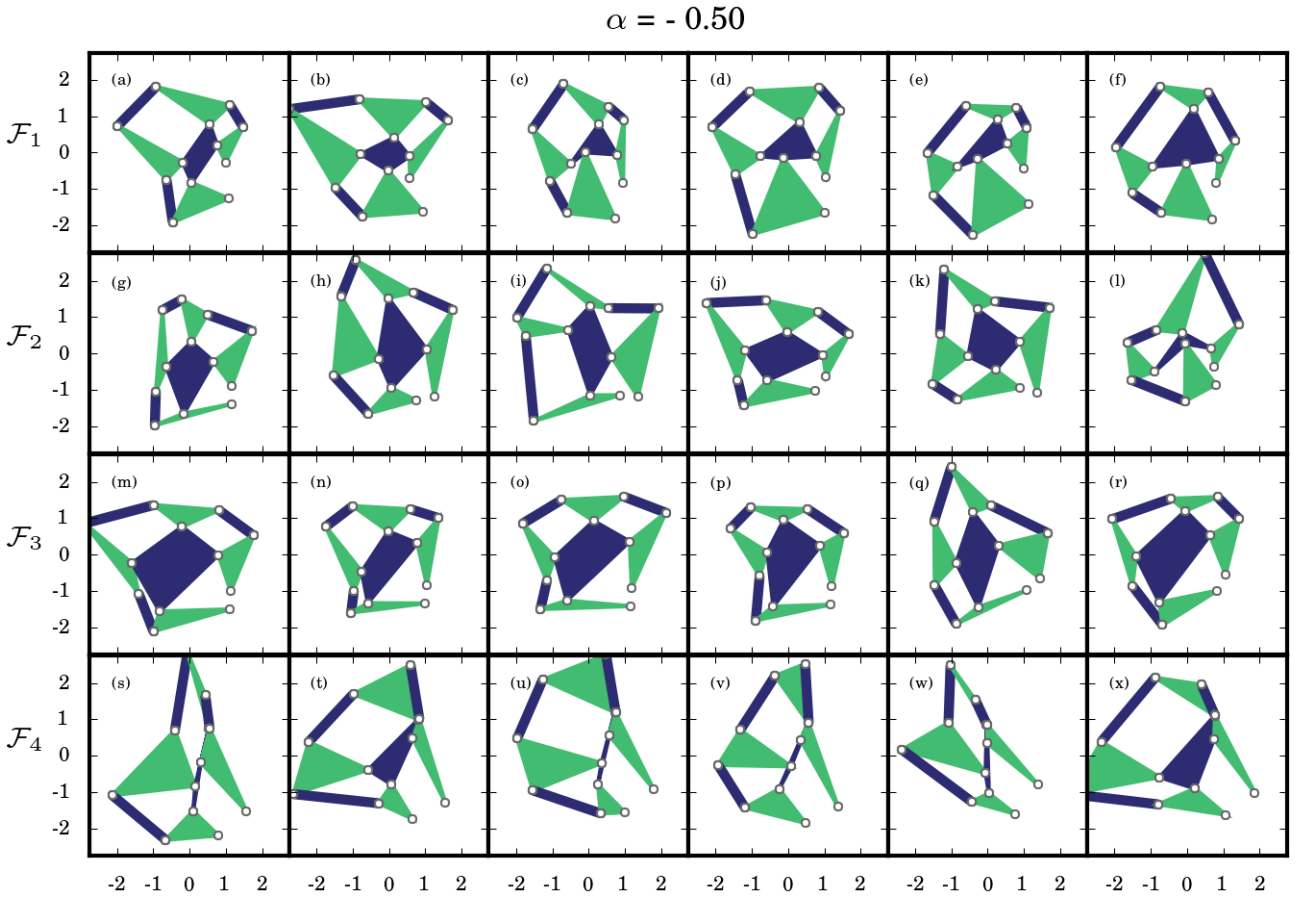

Figure 4.7: A gallery of low $\boldsymbol{f}$ solutions for the $D_t(\theta)$ curves $\mathcal{F}_1$-$\mathcal{F}_4$, α = -0.50. Each row corresponds to a different family (labeled). $\boldsymbol{f}$ is of the order of: 10^{-8} or less for $\mathcal{F}_1$, 10^{-6} for $\mathcal{F}_2$, 10^{-5} for $\mathcal{F}_3$ and 10^{-3} for $\mathcal{F}_4$ curve.

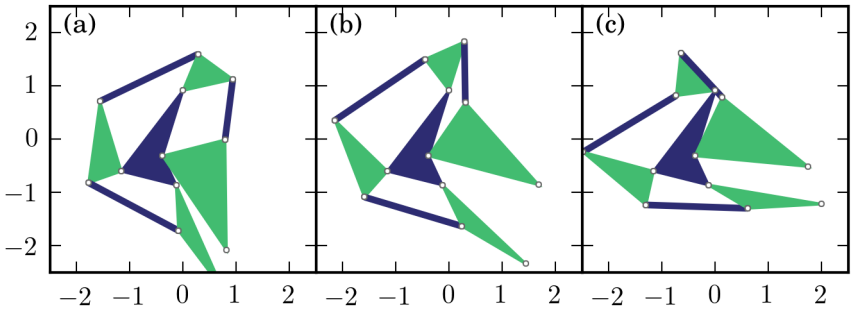

Figure 4.8: An example mechanism consisting of a narrow convex linkage (top-right linkage in (b)) shown in the deformed states of (a) θ = -60°, (b) θ = 0°, and (c) θ = 60°. This particular mechanism is a solution for $\mathcal{F}_2$, α = 0.50 and is the same as shown in Fig. 4.6(g). The corresponding objective function value, $\boldsymbol{f}$ is 4.75×10^{-7}. These types of mechanisms consisting of narrow linkages are frequently discovered for non-linear target curves i.e. $\mathcal{F}_2$-$\mathcal{F}_4$, $\alpha = 0.50$.

these narrow linkages. For $\mathcal{F}_4$ target curve however, we found out that the presence of these linkages is far more prevalent.

Similarly, we show the mechanisms corresponding to the top six solutions for the target curves $\mathcal{F}_1$-$\mathcal{F}_4$, α = -0.50 in Fig. 4.7. We again obtain a variety of solutions different greatly from one another in terms of their geometry. Of particular interest are the examples corresponding to the $\mathcal{F}_2$ and $\mathcal{F}_3$ target curves. We notice the absence of previously observed narrow convex linkages for $\alpha = 0.50$. In this case, PSO discovers several good solutions remaining far from the constraint boundary. This could be a direct outcome of the different objective function landscape. For $\mathcal{F}_4$ target curve, however, we still encounter the narrow convex linkages. Such systems will inevitably pose problems during fabrication via 3D printing because of the limited resolution of the printer. Moreover, for the sake of generating simpler mechanisms for the $\mathcal{F}_4$ target curves, we decide to circumvent this problem. We impose an additional constraint on the geometry of the mechanisms, which we discuss below.

Constraint Adjustment for Extreme Curves – We address the issue of mechanisms consisting of extremely slender linkages found consistently

for the $\mathcal{F}_4$ target curves, $\alpha = |0.50|$ by imposing an additional constraint Γ_4, which aims to keep the distance between the opposite pair of inner vertices of each of the internal four-bar linkages within a reasonable range of [0.50, 2.50]. We use the same method to quantify its violation, as we used for quantifying the constraint Γ_3 in the previous chapter (§3.4.2). We combine the total violation of both Γ_3 and Γ_4 into a single penalty term and denote it with $\boldsymbol{r}'$. For simplicity, we retain the old symbol $\boldsymbol{f}$ to denote the modified objective function and extend Eq. (3.23) as:

$$\boldsymbol{f} = \boldsymbol{g} + \boldsymbol{p} + \boldsymbol{q} + \boldsymbol{r}', \tag{4.1}$$

where the definitions for $\boldsymbol{g}, \boldsymbol{p}$ and $\boldsymbol{q}$ are the same as in the previous chapter.

With this new definition of $\boldsymbol{f}$, we carried out a series of additional PSO simulations. We first check how the addition of this constraint affects the performance of PSO. Fig. 4.9 shows in: (a) the $\boldsymbol{f}$ vs $\boldsymbol{s}$ scatter plot for $\alpha = 0.05$, (b) the $\boldsymbol{f}$ vs $\boldsymbol{s}$ scatter plot for $\alpha = 0.50$, and (c) the PDFs of $\boldsymbol{f}$ for $\alpha = \{0.05, 0.10 \ldots 0.50\}$. The corresponding plots for negative α values are shown in Fig. 4.9(d-f). Despite the modification in $\boldsymbol{f}$, we do not observe any significant differences in the scales of $\boldsymbol{f}$ when compared with Fig. 4.5. In fact, the results are quite similar. We conclude that the performance of PSO remains essentially unaffected.

We show the top-performing mechanisms for the $\mathcal{F}_4$ curve, $\alpha = \pm 0.50$ in Fig. 4.10. We notice the absence of slender linkages in the mechanisms - the application of the new constraint serves the purpose. Instead, we now notice new common trends within the geometry of the mechanisms: *(i)* polygon P_2 [Fig. 4.10(a)] of the mechanisms almost approaches to the shape of a bar, *(ii)* the 'free' vertex of the polygon P_8 lies extremely close to the edge of the polygon P_6 for $\alpha = 0.50$ and vice versa for $\alpha = -0.50$. We will show in the next section when we fabricate real samples that the proximity of the bars does not hinders the hinging motion of the mechanisms. Overall, we conclude that the best-performing mechanisms share some similarities in terms of the geometry and thus represent a lack of diversity.

Mechanisms in their deformed states – We now show the mechanisms in their deformed configurations. Instead of solely selecting the mechanisms on the basis of lowest values of $\boldsymbol{f}$, for easy demonstration, we also prefer simpler geometry, which we decided by visual inspection of the solution ensemble. The deformed states of these examples are shown in Fig. 4.11

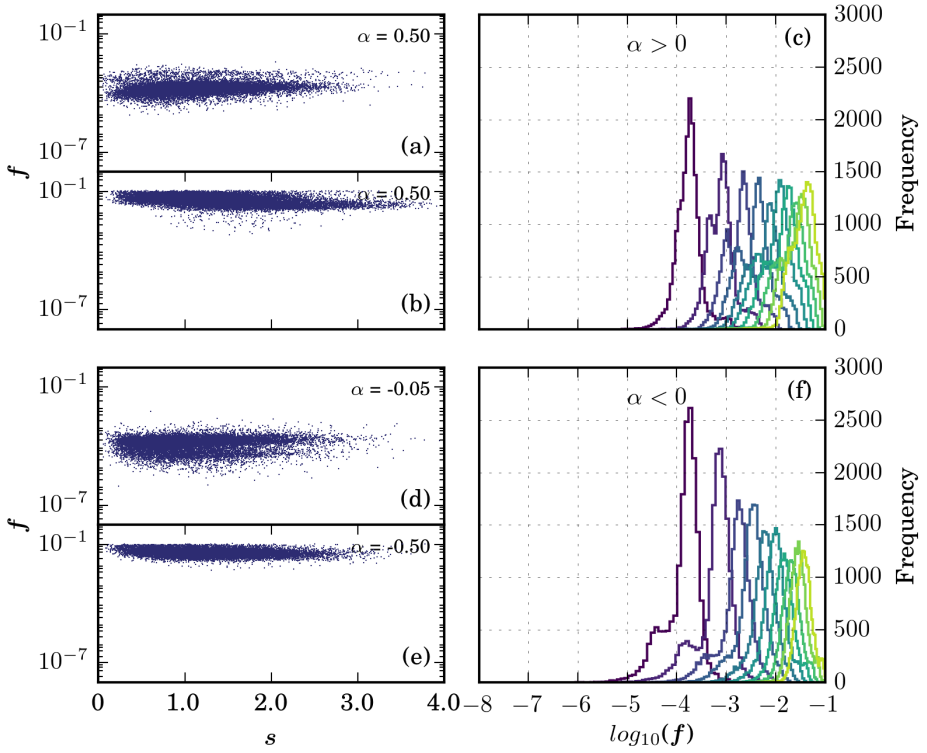

Figure 4.9: Statistics summarizing how the PSO performed over $\mathcal{F}_4$ target curves [Fig. 4.1(d)], with the modified definition of $\boldsymbol{f}$ [Eq. (4.1)]. (a) objective function $\boldsymbol{f}$ vs order-parameter $\boldsymbol{s}$ scatter plot for $\alpha = 0.05$, (b) $\boldsymbol{f}$ vs $\boldsymbol{s}$ scatter plot for $\alpha = 0.50$, and (c) probability density functions (PDFs) of $\boldsymbol{f}$ for $\alpha = 0.05, 0.10, \ldots\ldots 0.50$. The PDFs for different α values are colored differently and are based on the colorbar shown in Fig. 4.1. (d, e) Corresponding $\boldsymbol{f}$ vs $\boldsymbol{s}$ scatter plots, and (f) PDFs of $\boldsymbol{f}$ for negative α values.

and Fig. 4.12 for $\alpha = 0.50$ and $\alpha = -0.50$ respectively. There, within each figure, the central panel shows the mechanism in the neutral state $\theta = 0°$, and the left and the right panels show the mechanism in the deformed states of $\theta = -30°, -60°$ and $\theta = 30°, 60°$ respectively.

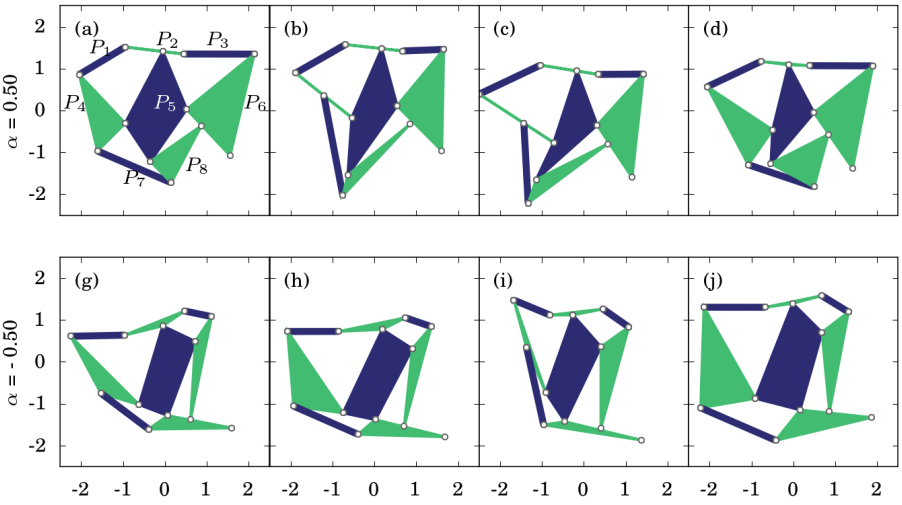

Figure 4.10: The best-performing mechanisms for the $\mathcal{F}_4$ target curves, $\alpha = \pm 0.50$ with the modified definition of $\boldsymbol{f}$ given by Eq. 4.1 that includes the constraint to avoid narrow linkages observed in Fig. 4.6, 4.7. The mechanisms for $\alpha = 0.50$ are shown in (a)-(d) and in (g)-(j) for α = -0.50. The scales of $\boldsymbol{f}$ are 10^{-4} for $\alpha = 0.50$ and 10^{-3} or for α = -0.50. We can notice that the inclusion of constraint Γ_4 avoids the presence of narrow linkages previously observed.

4.4 A Proof of Concept with 3D Printing

In this section, we explore experimental realizations of the computer-designed bi-stable and tri-stable unit cells, as well as some metatilings based on these unit cells. We bring these designs to life by 3D printing. We begin by preparing 3D CAD models in a CAD software followed by 3D printing them.

For our 3D printed samples, both bending and stretching of the elastic hinges costs a finite amount of energy. It is the competition between these two energies that determines whether or not a sample is able to remain in the expected stable state(s). Thus, an issue that requires attention is the role of the hinges. For example, thicker hinges might be able to provide enough restoring torque to compensate for the stretching energy leading the samples to 'flip-back' to their original stable state, i.e. the one we print

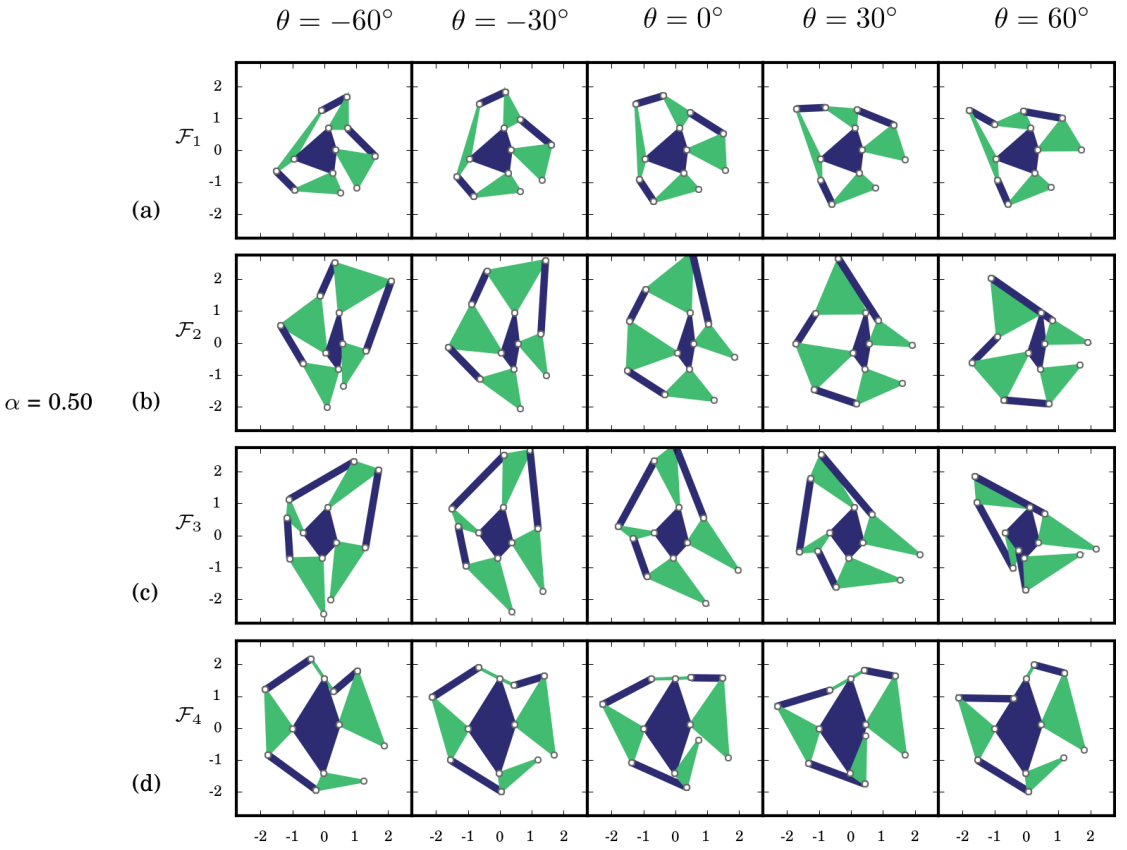

Figure 4.11: Deformed states for example mechanisms of (a) $\mathcal{F}_1$, (b) $\mathcal{F}_2$, (c) $\mathcal{F}_3$ and (d) $\mathcal{F}_4$ target curve, α = 0.50. Within each figure, the central panel shows the mechanism in the neutral configuration ($\theta = 0°$) and in the deformed configurations at $\theta = -30°, -60°$ and $\theta = 30°, 60°$ in the left and right panels respectively.

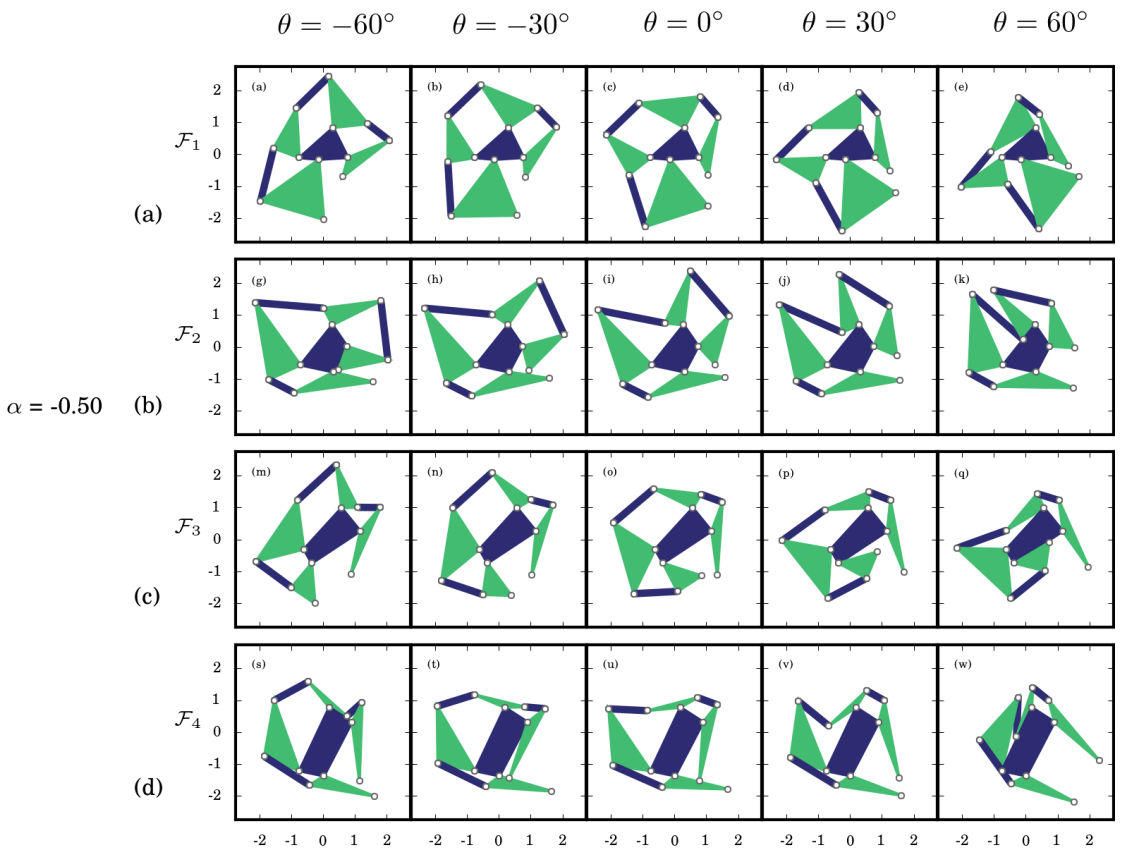

Figure 4.12: Deformed states for example mechanisms of (a) $\mathcal{F}_1$, (b) $\mathcal{F}_2$, (c) $\mathcal{F}_3$ and (d) $\mathcal{F}_4$ target curve, α = -0.50. Within each figure, the central panel shows the mechanism in the neutral configuration ($\theta = 0°$) and in the deformed configurations at $\theta = -30°, -60°$ and $\theta = 30°, 60°$ in the left and right panels respectively.

the samples in. On the other hand, thinner hinges might not store enough stretching energy in the first place, however, if they do, the *switch-feel* might be too weak leading to accidentally switching between the states. Moreover, deformations of the quads are no longer absent. Hence, only experimenting with the hinge thickness can tell whether designed properties emerge in the realistic samples.

4.4.1 Unit Cells

How to first design a bi-stable unit cell? We start with a solution generated by PSO for the target $D_t(\theta)$ curve: $\mathcal{F}_2$, α = -0.50. We then want to choose the two stable states, the system should switch to and fro. To ensure the *switchability*, we choose these states to be as far away from one another as possible, i.e. at $\theta = -60°$ and $\theta = 60°$ or $D = 1.25$ [see Fig. 4.1 (b)]. Out of these two stables states, we 3D print the sample at $\theta = -60°$ configuration. For this purpose, with the mechanism in $\theta = -60°$ configuration, we fit-in the absent night polygon such that the polygonal edge length that connects the polygons P_6 and P_8 is equal to $D(60°)$ i.e. 1.25. See Fig. 4.10(a) for the polygonal numbering. We also take advantage of the inconsequential boundary of the unit cell and augment every rigid boundary unit to a quadrilateral. This is done in such a manner that the quadrilaterals on the boundary do not *barge in* before the expected stable state is reached.

An example of a such a 3D printed sample is shown in Fig. 4.13(a). We used a flexible elastic filament for 3D printing, known by its commercial name *Filaflex*. The scale of the sample is labeled. The height of the sample (out-of-plane) is 10 mm. The thickness of the connecting hinges is ≈ 0.55 mm. Fig. 4.13(c) shows the base mechanism. The objective function value $\boldsymbol{f}$ for this solution is 3.2×10^{-5}. When deformed internally, the other stable state that the sample switches to is shown in Fig. 4.13(b). We observe reasonably good agreement with the expected deformed state, $\theta = -60°$ shown in Fig. 4.13(d). We should point out that hinge thickness plays a key role here. We found out that a samples with higher hinge thickness either did not produce pronounced switch-ability or did not no exhibit bi-stability at all.

Similar to the approach stated above, we fabricate a tri-stable unit cell. We begin with a sample solution for $\mathcal{F}_4$ curve, $\alpha = 0.50$ [Fig. 4.14(e)] and accordingly design the unit cell such that the three stable states are at: θ = -45°, $\theta = 0°$ and $\theta = 45°$ i.e. where $D = 1.0$. We 3D print the sample

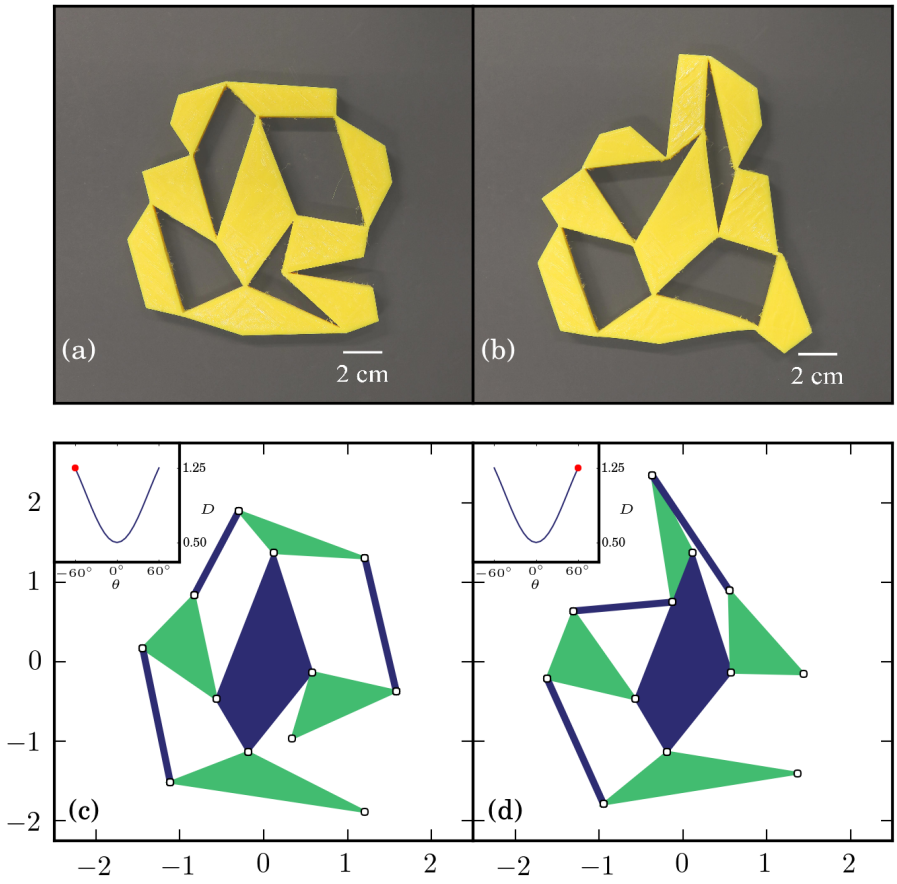

Figure 4.13: A 3D printed 3x3 bi-stable unit cell in the two stable states (a), (b) corresponding to (c) $\theta = -60°$ and (d) $\theta = 60°$ configurations of the constituent mechanism. We 3D print the sample in (a), which exhibits reversible switch-ability to and from (b). Inset in (c),(d) show the $D(\theta)$ curve. The mechanism is a solution for $\mathcal{F}_2$, α = -0.50. The objective function value $\boldsymbol{f}$ is $3.2{\times}10^{-5}$. Comparing (b) and (d), we observe reasonably good agreements between experiments and simulations.

in $\theta = 0°$ configuration and expect switch-ability to the other two stable states existing on the opposite sides of θ. In our first attempt, we designed the connecting hinges with a minimum thickness of $\approx$ 0.50 mm, and as

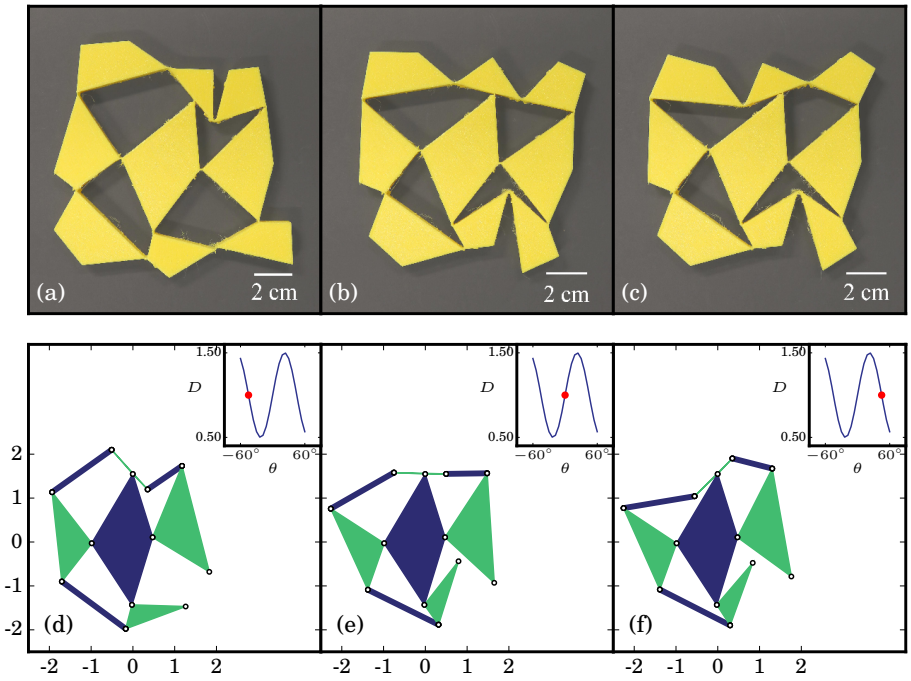

Figure 4.14: A 3D printed 3x3 tri-stable unit cell in the three stable states (a)-(c) corresponding to (d) $\theta = -45°$, (e) $\theta = 0°$ and (f) $\theta = 45°$ configurations of the constituent mechanism. We 3D print the sample in (b), which exhibits reversible switch-ability to and from (a) and (c). Inset in (d)-(f) show the $D(\theta)$ curve. The mechanism is a solution for $\mathcal{F}_4$, $\alpha = 0.50$. The objective function value $\boldsymbol{f}$ is $6.7{\times}10^{-3}$. Comparing (a),(c) with (d)(f), we observe good agreements between experiments and simulations.

such did not designed its length. We found out that by doing this, the unit cell did not switch to the neighboring stable states. The justification is straightforward: hinges with minimal length do not provide with enough stretching elastic energy barrier such that the unit cell can hold itself.

One possible way to overcome this would be via trying thinner hinges, the choice of which, however, is limited by the printer resolution, which is $\approx$ 0.40 mm in our case. In order to mitigate this issue and achieve tristability, we attempted another method. This time, we designed the connector hinges

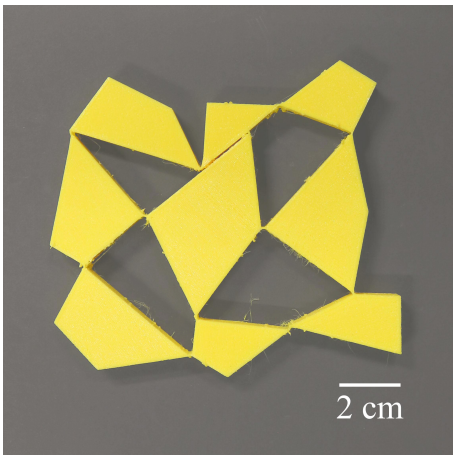

Figure 4.15: For the 3D printed sample shown in Fig. 4.14(b), we observed an extra stable stable which was not predicted

with small finite length of ≈ 2 mm. Fig. 4.14(b) shows the sample. The height of the sample (out-of-plane) is 10 mm. Designing the hinges in such a manner leads to tristability! The two stable states corresponding to $\theta =$ -45°, and $\theta = 45°$ states of the base mechanism are shown in Fig. 4.14(a,c) respectively. We can match from figure Fig. 4.14(d,f) that we indeed retrieve the expected stable states. Note that the value of $\boldsymbol{f}$ for this solutions is 6.7×10^{-3}. For this sample, we noticed an extra unpredicted stable state shown in Fig. 4.15.

4.4.2 Metatilings

We will now discuss some tilings consisting of these unit cells. Ideally, we would desire a system where the unit cells can individually alter their stable states. However, assembling the units cells into tilings and 3D printing them with flexible material does not immediately guarantees the expected shape-transformable behavior. This is because of the new elastic frustration introduced by the neighboring unit cell. Frustration alters the energy landscape, affecting the existing minima and adding the new ones, thus hindering the desired functionality [39].

Before printing a mono-material tiling, we first attempted a simpler method to obtain shape-transformable systems coupling pin-jointed rigid linkages with linear springs. Fig. 4.16 shows schematically, a tiling comprising of two copies of the bi-stable unit cell shown in Fig. 4.13(c), where the rigid units are connected together through pin-joints. The free corners are

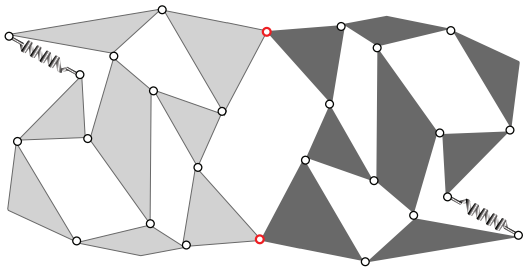

Figure 4.16: A schematic diagram showing a system of two bi-stable unit cells [Fig. 4.13(c)] connected together (at joints marked in red). The linkages are rigid and are connected together through pin-joints. The open-corners are connected through linear springs.

connected with linear springs of rest length such that the unit cells switch to the other stable state [Fig. 4.13(d)]. Our method of repeating copies in the plane is same as discussed in the previous chapter [§3.9.2, Fig. 3.37]. The two unit cells share the pin-joint connections marked in red. We 3D printed this design [Fig. 4.17(a)], and observed that the unit cells switch states but not independent of each other - one actuates another [Fig. 4.17(b)].

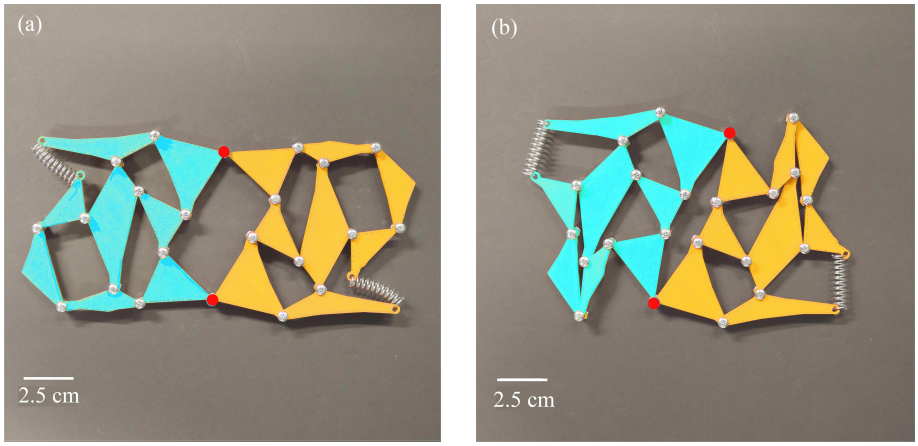

(a) **(b)**

Figure 4.17: A bi-stable system. (a) Real sample of the design shown in Fig. 4.16. The rigid linkages are connected through pin-joints (diameter $\approx$ 3 mm). The open vertices of the unit cells are connected with linear springs of rest length $\approx$ 2.5 cm. In this case, we observed that the unit cells switch states but not independently.

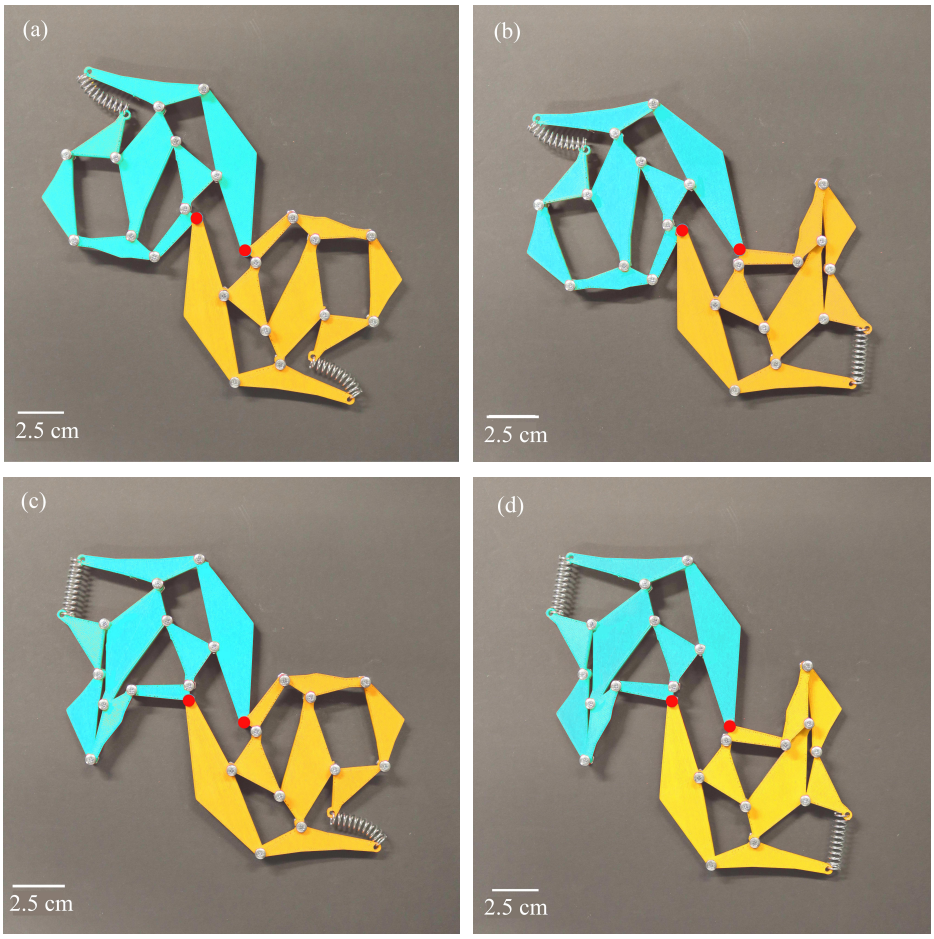

Figure 4.18: A quad-stable system. (a) We altered the geometry of the rigid linkages in Fig. 4.17(a) that connect the two unit cells together in such a way that the displacement of the connecting nodes (in red) is minimal as the cells deform, thus hoping to avoid actuating the cells simultaneously. We found out that this works. The systems in its other combinations of stable states is shown in (b-d).

The geometry of the boundary linkages that connect the unit cells together plays a critical role. We altered their geometry such that the displacement

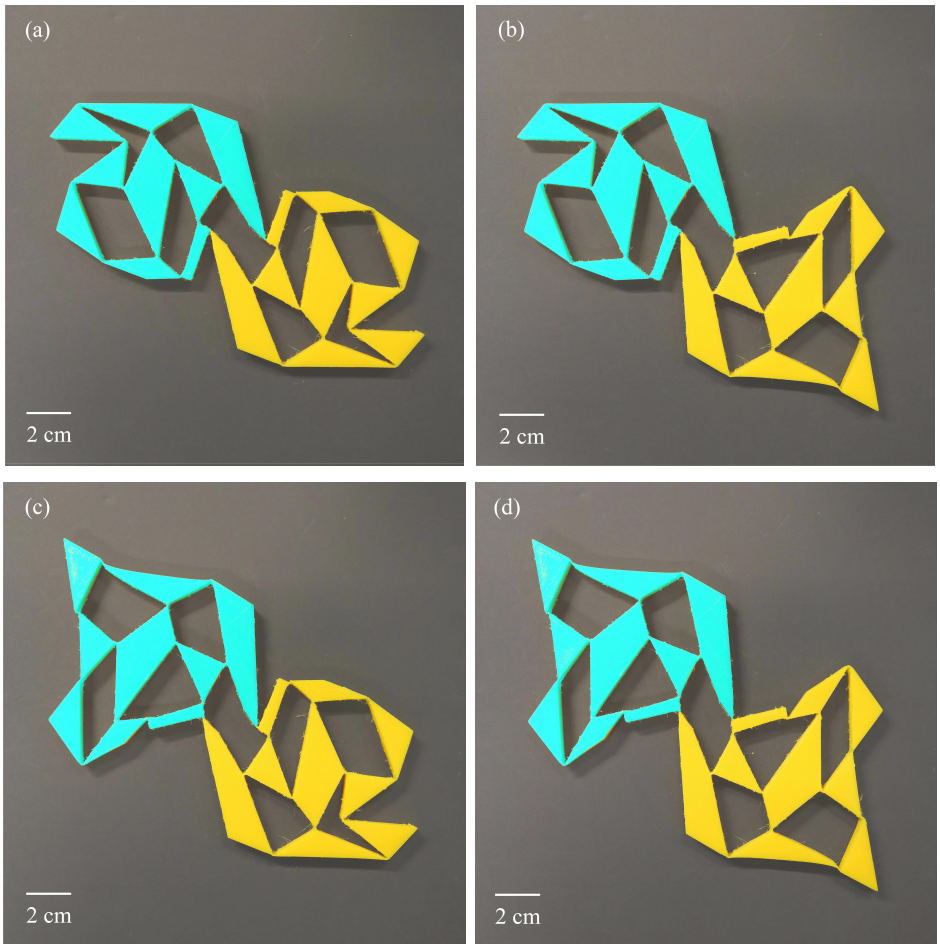

Figure 4.19: A quad-stable system. (a) 3D printed version of the system shown in Fig. 4.18(a). We printed this sample with flexible elastic material called *filaflex*. The scale of the sample is labeled. The thickness of the sample if $\approx$ 10mm. The sample in its other combinations of stable states is shown in (b-d).

of the connecting node is minimal - thus trying to avoid the actuation of the neighboring cell. Fig. 4.18(a) shows the sample. This allows the cells to change states individually; thus rendering us a system that is quad-stable

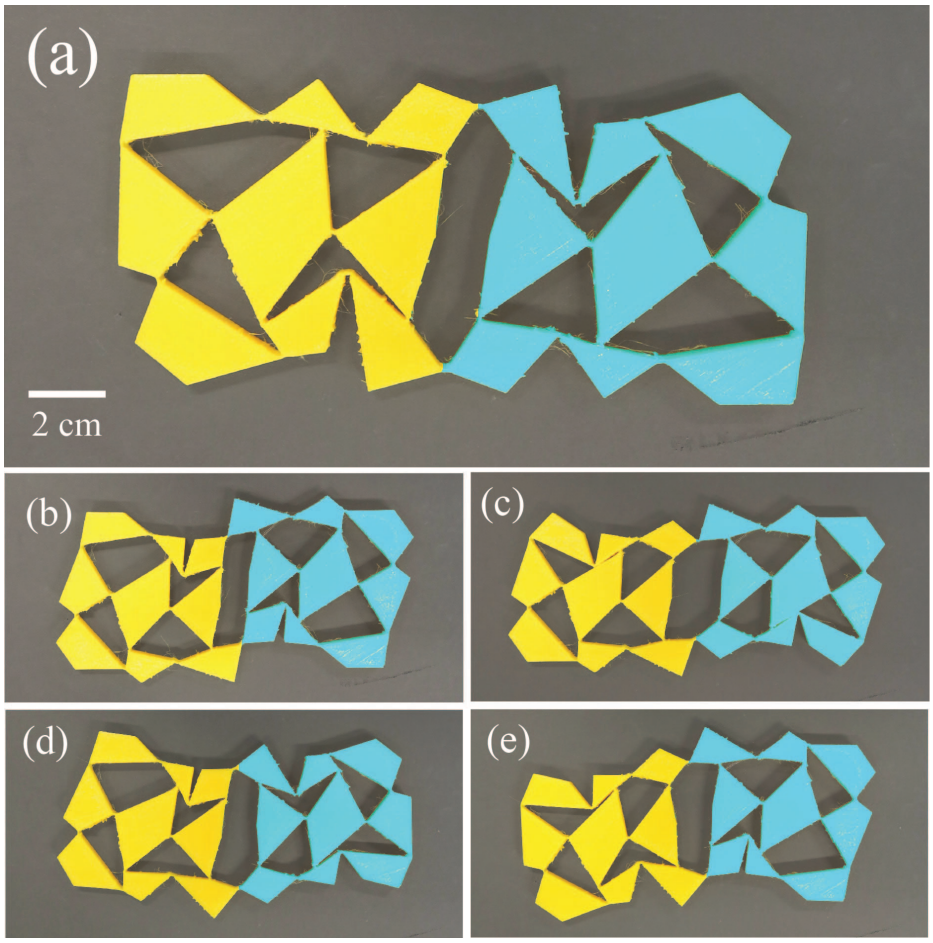

Figure 4.20: A penta-stable system. (a) Two repeated copies of the unit cell shown in Fig. 4.14(b). The scale of the sample is labeled and the thickness of the samples is $\approx$ 10 mm. In (b-e), we show the four other stable states the system exhibits. Notice that unit cells correspond to (b) the stable state shown in Fig. 4.14(c), (c) stable state shown in Fig. 4.15, and (d,e) combination of stable states shown in Fig. 4.14(a,c).

in a manner [Fig. 4.18(b-d)]. We 3D printed the design in Fig. 4.18(a) by flexible elastic material [Fig. 4.19(a)], and observed similar switchable behavior [Fig. 4.19(b-d)], although the additional elastic frustration limits

retrieving the exact expected states.

As a final example, we also tiled two copies of the unit-cell shown in Fig. 4.14(b) and observed penta-stable behavior. Fig. 4.20(a) shows the sample. The stable states that the sample switches to are shown in Fig. 4.20(b-d).

4.5 Discussion and Conclusion

In this chapter, we extended our methodology to design new classes of multi-stable 2D mechanical metamaterials consisting of hinging polygons, with up to penta-stability reported in the current work. We show that although elastic frustrations are generally known to limit functionalities, they can be carefully channeled to make a system switch states, thus opening new avenues for shape-transformable mechanical materials. In §4.2, we began with optimizing the mechanism design for four different families of varying complexity of linear and non-linear $D_t(\theta)$ curves ($\mathcal{F}_1$-$\mathcal{F}_4$). Characterizing PSO, we established that within the non-linear $D_t(\theta)$ curve families, the solution quality drops with an increase in the magnitude of variation of D with θ, whereas it remains unaffected for the linear curves; and among these families, the solution quality suffers substantially with an increase in the number of extrema in the $D(\theta)$ curves. We showed the actual optimized mechanisms in §4.3, and also showed that for extreme curves within the family $\mathcal{F}_4$, we encounter designs that limit their fabricability. There, we also discuss the additional imposed constraint to avoid such designs. Finally, in §4.4, we bring the computer-designed structures to life by 3D printing and demonstrate practical realizations of bi-, tri-, quad- and penta-stable systems.

Acknowledgments

The large batch of PSO simulations were performed availing the high-performance computing facilities offered by SURFsara, Amsterdam. We are especially thankful for their excellent technical support to facilitate efficient computing and data transfer. The work presented in this chapter is part of an industrial partnership programme (IPP) *'Computational Sciences for Energy Research (CSER)'* started in 2012, and funded by the Shell Global Solutions International B.V., the Netherlands Organization for Scientific

Research (NWO) and the Foundation for Fundamental Research on Matter (FOM).

Summary

Making their initial appearances in the field of optics, acoustics and electromagnetism, metamaterials [1–3] are carefully engineered macro-, micro- and nanoscale materials, whose physics is governed by their architecture - often consisting of periodically arranged specially designed unit cells. The central concept of design-determined material properties has led to the discovery of several non-trivial materials with unique functionalities such as negative refraction index. Mechanical metamaterials [4–19] - a more recent branch of metamaterials - further extend this principal idea to design soft deformable materials with extreme mechanical responses as well as advanced functionalities such as programmability in mechanical response [20], tunable control of response parameters [13], shape-transformable materials [16, 37].

On a structural level, the properties featured by a majority of mechanical metamaterials can be ascribed to the finite number of soft internal degrees-of-freedom that allow the system to deform via preprogrammed frustration-free, low-energy deformation pathways in the configuration space [37]. As it so happens, often it becomes possible to represent these low-energy deformation modes in an ideal fashion through a mechanism consisting of rigid geometrical units connected together either by soft slender connector joints (3D) or by ideal pin-joints (2D) [18, 38–41]. Conversely, these mechanisms also serve as an intuitive starting point to initiate and adapt the design of mechanical metamaterials to requirements. Traditional design methods mainly comprise of trial and testing, and can only well handle simple design tasks, not to mention that the suggested designs can be periodic and non-generic. In order to solve complex design problems, computer algorithm based inverse strategies provide state-of-the-art solution [43–51]. One way in which they can be utilized is by framing the material design problem as an optimization problem, where we optimize the values of parameters that control the design -

design variables - in order to meet the desired target response. Such 'inverse' material design frameworks offer two other main advantages: *(i)* automating the process by facilitating to optimize the material design for more than one target property, and *(ii)* discovering many near-perfect solutions that fit the target criteria reasonably well, thus enlarging the design space [35].

In this thesis, we present novel inverse strategies to design 2D mechanical metamaterials, whose zero-energy deformations can be modeled by one degree-of-freedom mechanisms consisting of pin-jointed polygons. We demonstrate that by optimizing the characteristic trajectory of these mechanisms, one can design generic metamaterials that exhibit complex programmable mechanics, atypical zero-energy deformations and shape-transformable behavior.

Chapter 2 – In the second chapter of this thesis, we start off by discussing a physical approach aimed to qualitatively model the four different mechanical regimes observed for a laterally confined quasi-2D biholar sheet [20], by a one degree-of-freedom spring-coupled mechanism consisting of pin-jointed rectangles - *soft mechanism*. Once confirming its capability to do so, we show that the experimentally observed mechanical regimes can also be retrieved geometrically. Based on the geometrical analysis, and as the most pertinent result of the chapter, we suggest an inverse strategy to rationally design mechanical metamaterials for several different confinement controlled responses. The main essence is that different types of equilibria that unfold as the control parameter (horizontal confinement in this case) is varied can be manipulated by the trajectory of the underlying mechanism. We modify our soft mechanism by coupling its hinges with torsional springs and observe some of the qualitative agreements with [70] in terms of how the critical values of horizontal strains that separate the mechanical regimes alter as the thickness of the hole-connector beams is increased. Finally, we use the soft mechanism to understand the case where the neighboring holes in the biholar sheet approach to be equi-sized, and mathematically show that at this limiting point, the four mechanism regimes emerge from the unfolding of an imperfect pitchfork bifurcation.

Chapter 3 – In the third chapter, we begin by asking the question which generic systems of specially designed pin-joint quadrilaterals can form perfect or approximate mechanisms. We do this with the ultimate

purpose of designing generic yet flexible 2D mechanical metamaterials based on these mechanisms, which feature an extremely low-energy deformation mode, while ordinarily one would expect them to be rigid. We demonstrate that the problem can be answered by searching for optimal design of a *precursor* one degree-of-freedom mechanism such that it meets a specific target curve that characterizes the internal deformation. We tackle this problem inversely, formulating it as an optimization problem, and in a nutshell, optimize for the design variables in order to match the prescribed target curve. We utilize a search algorithm inspired from the food-searching capability of bird flocks - *Particle Swarm Optimization (PSO)* [60, 90, 91] to carry out the optimization task. We show that the hyperparameter setting of PSO plays a critical role in influencing the solution quality, solution distribution type and the local or global search behavior of the swarm. PSO discovers a plethora of designs that render high quality approximate mechanisms, when structurally one would guess them to be rigid. We prove that for the good-quality solutions, it is highly likely that PSO gets trapped in the deep local minima, while this is not true for the poor-quality solutions. Finally,based on these mechanisms, we fabricate unit cells of soft mode exhibiting metamaterials, via 3D printing and suggest a method to tile these unit cells into regular tessellations, while preserving the original soft mode.

Chapter 4 – In the fourth chapter, we put to test a crucial feature of any automated inverse material design framework, which is to be able to optimize for not just one but multiple target properties. Specifically, by optimizing for different target curves of the *precursor* mechanism, we aim to: *(i)* statistically correlate the performance of our model versus the general complexity of the input target curves, and *(ii)* on top of these computer-designed mechanisms, fabricate bi-stable and tri-stable unit cells and some tilings comprising of them that exhibit multi-stable behavior. Doing this, we establish novel examples of 2D shape-transforming mechanical metamaterials.

Samenvatting

Metamaterialen [1–3], voor het eerst geintroduceerd in het veld van optica, akoestiek, en elektromagnetisme, zijn zorgvuldig ontworpen materialen op macro-, micro- of nanoschaal, waarvan de fysica wordt bepaald door hun architectuur. Deze architectuur bestaat vaak uit speciaal ontworpen periodiek gerangschikte eenheidscellen. Dit concept, waarbij materiaaleigenschappen worden bepaald door het ontwerp van het materiaal, heeft geleid tot de ontdekking van een aantal niet-triviale materialen met functionaliteiten die de wetten van de fysica lijken te tarten. Een voorbeeld hiervan zijn materialen met een negatieve brekingsindex. Bij mechanische metamaterialen [4–19], een recente ontwikkeling, wordt het idee van ontworpen materialen verder toegepast, wat heeft geleid tot zachte vervormbare materialen met extreme mechanische reacties, en geavanceerde functionaliteiten zoals de programmeerbaarheid van de mechanische respons [20], instelbare controle van responsparameters [13], vorm-transformeerbare materialen [16, 37].

De eigenschappen die een groot deel van de mechanische metamaterialen laten zien op een structureel niveau kunnen worden toegeschreven aan een eindig aantal zachte interne vrijheidsgraden, die het systeem toestaan te deformeren via voorgeprogrammeerde frustratievrije, laag-energetische deformatiepaden in de configuratieruimte [37]. Vaak is het mogelijk deze laag-energetische deformatie op een ideale manier voor te stellen door een mechanisme dat bestaat uit stijve geometrische eenheden verbonden door dunne zachte verbindingen (3D) of ideale penverbindingen (2D) [18, 38–41]. Deze mechanismen dienen ook als intuitieve startpunten om materialen te ontwerpen, of materiaalontwerpen aan te passen. Traditionele ontwerpmethoden bestaan vooral uit proberen en testen, en kunnen alleen simpele ontwerpopgaven aan. Daarbij zijn de ontwerpen die hieruit voortkomen vaak periodiek en niet generiek. Om deze complexe ontwerpproblemen op te

lossen, bieden computer algoritmen gebaseerd op geïnverteerde strategieën een 'state of the art' oplossing [43–51]. Een manier waarop algoritmen gebruikt kunnen worden is door het ontwerpprobleem voor te stellen als een optimalisatieprobleem, waarbij de parameters die het ontwerp bepalen (de design variables) worden geoptimaliseerd om de gewenste respons te bereiken. Een dergelijk geïnverteerd ontwerp voor materialen heeft twee belangrijke voordelen: *(i)* het optimaliseren van meerdere gewenste eigenschappen is geautomatiseerd, en *(ii)* er worden meerdere bijna perfecte oplossingen ontdekt die de doelcriteria behoorlijk goed halen, waardoor de ontwerpruimte groter wordt [35].

In dit proefschrift bespreken we nieuwe geïnverteerde ontwerpstrategieen voor 2D mechanische metamaterialen, die kunnen worden gemodelleerd als mechanismen met een vrijheidsgraad bestaande uit polygonen met penverbindingen. We laten zien dat men, door optimalisatie van karakteristieke trajecten van deze mechanismen, een generiek metamateriaal kan ontwerpen met een complexe programmeerbare mechanica, atypische energieloze deformaties en vorm-transformeerbaar gedrag.

Hoofdstuk 2 – In het tweede hoofdstuk van dit proefschrift beginnen we met een fysische aanpak, erop gericht de vier geobserveerde regimes van een lateraal beperkt quasi-2D bipolair vlak [20] kwalitatief te modelleren. Hier gebruiken we een mechanisme met een vrijheidsgraad dat bestaat uit rechthoeken verbonden door penverbindingen - een zacht mechanisme. Nadat we hebben bevestigd dat dit inderdaad lukt, laten we zien dat experimenteel geobserveerde mechanische regimes ook geometrisch verkregen kunnen worden. Het belangrijkste resultaat van dit hoofdstuk, gebaseerd op een geometrische analyse, is een strategie om op een rationele manier mechanische metamaterialen te ontwerpen voor verscheidene responses die door confinement worden gecontroleerd. Het belangrijkste idee is dat verschillende types equilibria die zich ontwikkelen als de controleparameter (horizontale confinement in dit geval) gevarieerd wordt, gestuurd kunnen worden door het traject van het onderliggende mechanisme. Als we in ons zachte mechanisme torsieveren toevoegen aan de verbindingen zien we kwalitatieve overeenstemming met [70] in termen van hoe de kritische waardes van de horizontale spanning die de regimes scheiden veranderen als de dikte van de connector vergroot wordt. Als laatste gebruiken we het zachte mechanisme om het geval te begrijpen waarin aangrenzende gaten in

het bipolaire vlak bijna van gelijke grootte zijn, en laten we mathematisch zien dat in deze limiet de vier regimes ontstaan uit het ontvouwen van een imperfecte hooivorkbifurcatie.

Hoofdstuk 3 – In het derde hoofdstuk beginnen we met de vraag welke generieke systemen van speciaal ontworpen quadrilateralen met penverbindingen perfecte of benaderde mechanismen kunnen vormen. Het doel hiervan is het ontwerpen van een generiek maar flexibel 2D mechanisch metamateriaal gebaseerd op deze mechanismen die een lage energie deformatiemode laten zien, terwijl normaal wordt verwacht dat deze rigide zijn. We laten zien dat dit probleem kan worden aangepakt door te zoeken naar een optimaal ontwerp van een precursor mechanisme met een vrijheidsgraad, zodat het overeenstemt met een specifieke doelcurve die de interne deformatie karakteriseert. We gebruiken hier ook een geïnverteerde strategie, waarbij we dit interpreteren als optimalisatieprobleem, en kort gezegd optimaliseren we de ontwerpparameters zodat ze overeenstemmen met de doelcurve. We gebruiken een zoek-algoritme dat geïnspireerd is op voedselzoekende vogelzwermen — Particle Swarm Optimization (PSO) [60, 90, 91] — om de optimalisatie te verwezenlijken. We laten zien dat de hyperparameter instelling van de PSO een kritische rol speelt in de kwaliteit van de oplossing, de distributie van de oplossing en het lokale of globale zoekgedrag van de zwerm. PSO ontdekt een overvloed van ontwerpen die een hoge kwaliteit van benaderende mechanismen geven, terwijl het structureel lijkt alsof ze rigide zijn. We bewijzen dat het waarschijnlijk is dat voor oplossingen van hoge kwaliteit de PSO gevangen is in diepe lokale minima, terwijl dit niet het geval is voor oplossingen van lage kwaliteit. Tenslotte hebben we, gebaseerd op deze mechanismen, met 3D printers eenheidscellen gefabriceerd uit metamaterialen die een zachte modus laten zien, en stellen we een methode voor om deze eenheidscellen te rangschikken in reguliere betegelingen met behoud van de originele zachte modus.

Hoofdstuk 4 – In het vierde hoofdstuk testen we een cruciale eigenschap van elk geautomatiseerd geïnverteerd materiaal ontwerp, namelijk het in staat zijn om meerdere doeleigenschappen te optimaliseren. Meer specifiek optimaliseren we voor verschillende doelcurves van het precursor mechanisme, teneinde: *(i)* de prestaties van ons model versus de algemene complexiteit van de input curves statistisch te correleren en *(ii)* bovenop

de computer-ontworpen mechanismen bi- en tri-stabiele eenheidscellen te fabriceren en deze te rangschikken zodat zij multi-stabiel gedrag laten zien. Hiermee creëren we nieuwe voorbeelden van 2D vorm-transformerende mechanische metamaterialen.

Publication List

(i) Nitin Singh and Martin van Hecke,
Computer-aided Design of Complex Mechanical Metamaterials,
In preparation.

(ii) Nitin Singh, Corentin Coulais, Bastiaan Florijn, and Martin van Hecke.
The Soft Mechanism,
In preparation.

Curriculum Vitae

I was born on April 23rd, 1991 in Barnala (India). I grew up in the same city, and received my primary, middle and secondary education at the Y S School finishing my matriculation in 2006. I received my senior secondary education at SGGS Collegiate Public School, Chandigarh qualifying the certificate examination in 2008. I started my undergraduate studies in 2009 in the Dept. of Metallurgical and Materials Engineering, Indian Institute of Technology, Kharagpur. At the same institute, I started my integrated master's studies in 2013 and received both B.Tech.(Hons.) and M.Tech.(Dual) degrees in 2014.

After getting selected in an industrial partnership programme (IPP) 'Computational Sciences for Energy Research' financed together by Shell India and the Netherlands Organization for Scientific Research (NWO), in 2014, I started my PhD in the Mechanical Metamaterials group of Prof. M.L. van Hecke, working mainly at AMOLF, Amsterdam, and occasionally at Leiden University. Under his supervision, I have spent the last four years conducting research on the computational design of mechanical metamaterials, the results of which have been compiled in this thesis. During these years, I also gained opportunities to attend several scientific events and conferences: Woudschoten Conference, Woudschoten (2015); Physics@Veldhoven, Veldhoven (2015, 2016, 2017); Casimir Spring School, Heeg (2016); CSER Future Energy Conference, Utrecht (2016); Annual CSER Meeting, Bangalore (2016); and APS March Meeting (Baltimore 2016, New Orleans 2017).

In October 2018, I started working as Data Science Researcher at Shell India, Bangalore.

Acknowledgments

This thesis would have never been there if it was not for the support of people all around. Thanks Shell and NWO for offering such an amazing opportunity to do PhD in the first place. Martin, thank you, for your encouragement and assistance all along, not only in doing science but sometimes outside of it as well. When I look back, I feel grateful to have a kind and empathetic advisor like you. I have had many laughs at your witty sense of humor and funny proverbs. Bastiaan and Corentin, thanks for helping me in the research during the initial period of my PhD. I learned a lot from the discussions we had. Thanks Luc for your expert help in the code development. For the amazing HPC facilities and technical support provided by SURFsara: thank you. Thanks Dion with your technical knowledge in the 3D printing, that helped me fabricate some structures.

Thanks you, my fellow group members: Anne, Luuk, Margherita, Matthieu, Merlijn, Peter and Scott. Jeroen, Danielle and the staff of ICT, HR department at AMOLF: thank you. Thanks, Aditya, Prince and Soumen for the many great laughs and fun times. Thank you, my friends back in India. A special thanks to you Ceren.

I personally want to express my gratefulness towards my family, in particular my parents, sister and younger cousin-brother. Learning in life never ends, however with this PhD, my formal education comes to an end. I would like to express my sincere gratitude towards all the teachers. Your conduct is inspiring and contributions are precious which extend far beyond.

Bibliography

[1] Y. Liu and X. Zhang. *Metamaterials: A new frontier of science and technology*, Chemical Society Reviews **40**, 2494 (2010).

[2] J.P. Turpin, J.A. Bossard, K.L. Morgan, D.H. Wener, and P.L. Werner. *Reconfigurable and Tunable Metamaterials: A review of the Theory and Applications*, Int. J. Antennas Propag. **2014**, 429837 (2014).

[3] M. Kadic, T. Buckmann, R. Schittny, and M. Wegener. *Metamaterials beyond electromagnetism*, Reports on Progress in Phys. **76**, 126501 (2013).

[4] K. E. Evans and A. Anderson. *Auxetic materials: functional materials and structures from lateral thinking*, Adv. Mater. **12**, 617 (2000).

[5] W. Yang, Z. M. Li, W. Shi, B. H. Xie, M. B. Yang. *Review on auxetic materials*, J. Mat. Sci. **39**, 3269 (2004).

[6] Y. Prawoto. *Seeing auxetic materials from the mechanics point of view: A structural review on the negative Poisson's ratio*, Comp. Mat. Sci. **58**, 140 (2012).

[7] M. Kadic, T. Buckmann, R. Schittny, and M. Wegener. *On the feasibility of pentamode mechanical metamaterials*, App. Phys. Lett. **100**, 191901 (2012).

[8] T. Buckmann, M. Thiel, M. Kadic, R. Schittny, and M. Wegener. *An elasto-mechanical unfeelability cloak made of pentamode metamaterials*, Nat. Commun. **5**, 4130 (2014).

[9] R. Lakes, K. W. Wojiciechowski. *Negative compressibility, negative Poisson's ratio, and stability*, Phys. Status Solidi B **245**, 545 (2008).

[10] Z. G. Nicolaou and A. E. Motter. *Mechanical metamaterials with negative compressibility transitions*, Nat. Mater. **11**, 608 (2012).

[11] M. Wyart, H. Liang, A. Kabla, and L. Mahadevan. *Elasticity of Floppy and Stiff Random Networks*, Phys. Rev. Lett. **101**, 215501 (2008).

[12] L. R. Gomez, A. M. Turner, M. van Hecke, and V. Vitelli. *Shocks near Jamming*, Phys. Rev. Lett. **108**, 058001 (2012).

[13] J. L. Silverberg, A. A. Evans, L. McLeod, R. C. Hayward, T. Hull, C. D. Santangelo, and I. Cohen. *Using origami design principles to fold reprogrammable mechanical metamaterials*, Science **345**, 647 (2014).

[14] Z. Y. Wei, Z. V. Guo, L. Dudte, H. Y. Liang, and L. Mahadevan. *Geometric Mechanics of Periodic Pleated Origami*, Phys. Rev. Lett. **110**, 215501 (2013).

[15] C. Lv, D. Krishnaraju, G. Konjevod, H. Yu, and H. Jiang. *Origami based Mechanical Metamaterials*, Scientific Reports **4**, 5979 (2014).

[16] J. T. B. Overvelde, T. A. De Jong, Y. Shevchenko, S. A. Becerra, G. M. Whitesides, J. C. Weaver, C. Hoberman, and K. Bertoldi. *A three-dimensional actuated origami-inspired transformable metamaterial with multiple degrees of freedom*, Nat. Commun. **7**, 5979 (2014).

[17] D. Z. Rocklin, S. Zhou, K. Sun, and X. Mao. *Transformable topological mechanical metamaterials*, Nat. Commun. **8**, 14201 (2017).

[18] J. Paulose, B. G. Chen, and V. Vitelli. *Topological modes bound to dislocations in mechanical metamaterials*, Nat. Phys. **11**, 153 (2015).

[19] C. L. Kane and T. C. Lubensky. *Topological boundary modes in isostatic lattices*, Nat. Phys. **10**, 39 (2014).

[20] B. Florijn, C. Coulais, and M. van Hecke. *Programmable Mechanical Metamaterials*, Phys. Rev. Lett. **113**, 175503 (2014).

[21] G. W. Milton and A. Cherkaev. *Which Elasticity Tensors are Realizable?*, J. Eng. Mater. Tech. **117**, 483 (1995).

[22] T. Buckmann, R. Schittny, M. Thiel, M. Kadic, G. W. Milton, and M. Wegener. *On three-dimensional dilational elastic metamaterials*, New J. Phys. **16**, 033032 (2014).

[23] L. Cabras and M. Brun. *A class of auxetic three-dimensional lattices*, J. Mech. Phys. Solids **91**, 56 (2016).

[24] G. W. Milton. *Complete characterization of the macroscopic deformations of periodic unimode metamaterials of rigid bars and pivots*, J. Mech. Phys. Solids **61**, 1543 (2013).

[25] G. W. Milton. *New examples of three-dimensional dilational materials*, Phys. Status Solidi B **252**, 1426 (2015).

[26] K. Bertoldi, P. M. Reis, S. Willshaw, and Tom Mullin. *Negative Poisson's Ratio Behavior Induced by an Elastic Instability*, Adv. Mater. **22**, 361 (2010).

[27] J. Shim, S. Shan, A. Kosmrlj, S. H. Kang, E. R. Chen, J. C. Weaver, and K. Bertoldi. *Harnessing instabilities for design of soft reconfigurable auxetic/chiral materials*, Soft Matter **9**, 8198 (2013).

[28] I. M. Pryce, K. Aydin, Y. A. Kelaita, R. M. Briggs, and H. A. Atwater. *Highly Strained Compliant Optical Metamaterials with Large Frequency Tunability*, Nano Lett. **10**, 4222 (2010).

[29] N. I. Zheludev and Y. S. Kivshar. *From metamaterials to metadevices*, Nat. Mater. **11**, 917 (2012).

[30] H. Chen, J. F. O'Hara, A. K. Azad, A. J. Taylor, R. D. Averitt, D. B. Shrekenhamer, and W. J. Padilla. *Experimental demonstration of frequency-agile terahertz metamaterials*, Nat. Photon. **2**, 295 (2008).

[31] L. Ju, B. Geng, J. Horng, C. Girit, M. Martin, Z. Hao, H. A. Bechtel, X. Liang, A. Zettl, Y. R. Shen, and F. Wang. *Graphene plasmonics for tunable terahertz metamaterials*, Nat. Nano. **6**, 630 (2011).

[32] T. Tachi. *Generalization of Rigid-Foldable Quadrilateral-Mesh Origami*, Journal of the International Association for Shell and Spatial Structures **50**, 173 (2009).

[33] M. Schenk and S. D. Guest. *Geometry of Miura-folded metamaterials*, Proc. Natl. Acad. Sci. **110**, 3276 (2013).

[34] S. Waitukaitis, R. Menaut, B. G. Chen, and M. van Hecke. *Origami multistability: from single vertices to metasheets*, Phys. Rev. Lett. **114**, 055503 (2015).

[35] M. B. Pinson, M. Stern, A. C. Ferrero, T. A. Witten, E. Chen, and Arvind Murugan. *Self-folding origami at any energy scale*, Nat. Commun. **8**, 15477 (2017).

[36] A. Rafsanjani and D. Pasini. *Bistable Auxetic Mechanical Metamaterials Inspired by Ancient Geometric Motifs*, Ext. Mech. Lett. **9**, 291 (2016).

[37] C. Coulais, E. Teomy, K. de Reus, Y. Shokef, and M. van Hecke. *Combinatorial design of textured mechanical metamaterials*, Nature **535**, 529 (2016).

[38] C. Coulais, C. Kettenis, and M. van Hecke. *A characteristic length scale causes anomalous size effects and boundary programmability in mechanical metamaterials*, Nat. Phys. **14**, 40 (2018).

[39] K. Bertoldi, V. Vitelli, J. Christensen, and M. van Hecke. *Flexible mechanical metamaterials*, Nat. Rev. Mater. **2**, Article number: 17066: 1 (2017).

[40] J. N. Grima, A. Alderson, and K. E. Evans. *Auxetic behaviour from rotating rigid units*, Phys. Status Solidi (b) **242**, 561 (2005).

[41] G. W. Milton. *Complete characterization of the macroscopic deformations of periodic unimode metamaterials of rigid bars and pivots*, J. Mech. Phys. Solids **61**, 1543 (2013).

[42] P. M. Reis, H. M. Jaeger, and M. van Hecke. *Designer Matter: A perspective*, Ext. Mech. Lett. **5**, 25 (2015).

[43] A. Jain, J. A. Bollinger, T. M. Truskett. *Inverse methods for material design*, AIChE J. **60**, 2732 (2014).

[44] Y. Zhanga, W. Gao, S. Chen, H. Xiang, X. Gonga. *Inverse design of materials by multi-objective differential evolution*, Comp. Mater. Sci. **98**, 51 (2015).

[45] H. M. Jaeger and J. J. de Pablo. *Perspective: Evolutionary design of granular media and block copolymer patterns*, APL Mater. **4**, 053209 (2016).

[46] J. P. Wieczorek, O. Gol, and Z. Michalewicz. *An evolutionary algorithm for the optimal design of induction motors*, IEEE Trans. Magnet. **34**, 3882 (1998).

[47] C. W. Glassa, A. R. Oganova, and N. Hansen. *USPEXâĂŤEvolutionary crystal structure prediction*, Comp. Phys. Commun. **175**, 713 (2006).

[48] O. Sigmund. *On the Design of Compliant Mechanisms Using Topology Optimization*, J. Mech. Struct. and Mach. **25**, 493 (2007).

[49] M. Y. Wang, X. Wang, and D. Guo. *A level set method for structural topology optimization*, Comp. Methods in App. Mech. and Eng. **192**, 227 (2003).

[50] E. Michielssen, J. M. Sajer, S. Ranjithan, and R. Mittra. *Design of lightweight, broad-band microwave absorbers using genetic algorithms*, IEEE Trans. Microw. Theory Tech. **41**, 1024 (1993).

[51] H. Lipson. *Evolutionary synthesis of kinematic mechanisms*, Art. Intell. for Eng. Design, Anal. and Manufac. **22**, 195 (2008).

[52] J. W. Bandler. *Optimization Methods for Computer-Aided Design*, IEEE Trans. Microw. Theory Tech. **17**, 533 (1969).

[53] R. M. Hicks and P. A. Henne. *Wing Design by Numerical Optimization*, J. Aircraft **15**, 407 (1978).

[54] K.F. Man, K.S. Tang, S. Kwong. *Genetic algorithms: concepts and applications [in engineering design]*, IEEE Trans. Ind. Elect. **43**, 519 (1996).

[55] K. Deb. *Multi-Objective Optimization Using Evolutionary Algorithms*, Wiley (2001).

[56] D. W. Zingg, M. Nemec, and T. H. Pulliam. *A comparative evaluation of genetic and gradient-based algorithms applied to aerodynamic optimization*, Eur. Jour. Comp. Mech. **17**, 103 (2012).

[57] J. H. Holland. *Genetic Algorithms*, Sci. American **267**, 66 (1992).

[58] N. Hansen and A. Ostermeier. *Completely Derandomized Self-Adaptation in Evolution Strategies*, Evolutionary Comp. **9**, 159 (2001).

[59] H. G. Beyer and H. P. Schwefel. *Evolution Strategies: A Comprehensive Introduction*, Natural Comp. **1**, 3 (2002).

[60] J. Kennedy and R. Eberhart. *Particle swarm optimization*, In Proceedings of IEEE International Conference on Neural Networks. pages 1942-1948 (1995).

[61] M. Gendreau, J. Y. Potvin. *Handbook of Metaheuristics*, Springer US (2010).

[62] J. R. Koza. *Genetic programming as a means for programming computers by natural selection*, Stats. and Comp. **4**, 87 (1994).

[63] J. D. Lohn, G. S. Hornby, and D. S. Linden. *An Evolved Antenna for Deployment on Nasa's Space Technology 5 Mission*, Genetic Programming Theory and Practice II, 301 Springer (2005)

[64] R. Kicinger, T. Arciszewski, and K. De Jong. *Evolutionary computation and structural design: A survey of the state-of-the-art*, Comp. and Structs. **83**, 1943 (2005).

[65] J. A. Cabrera, A. Simon and M.Prado. *Optimal synthesis of mechanisms with genetic algorithms*, Mech. Mach. Theory. **37**, 1165 (2002).

[66] D. Rus and M. T. Tolley. *Design, fabrication and control of soft robots*, Nature **521**, 467 (2015).

[67] I. Harvey, P. Husbands, D.Cliff, A.Thompson and N.Jakobi. *Evolutionary robotics: the Sussex approach*, Robot. Auto. Sys. **20**, 205 (1997).

[68] H. Chen, G. Hautier, A. Jain, C. Moore, B. Kang, R. Doe, L. Wu, Y. Zhu, Y. Tang and G. Ceder. *Carbonophosphates: A new family of cathode materials for li-ion batteries identified computationally*, Chem. of Mater. **24**, 2009 (2016).

[69] H. C. B. Florijn. *Programmable Mechanical Metamaterials.* Ph.D. thesis, Leiden University (2016). hdl:1887/44475.

[70] B. Florijn, C. Coulais, and M. van Hecke. *Programmable mechanical metamaterials: the role of geometry*, Soft Matter **12**, 8736 (2016).

[71] M. Vangbo. *An analytical analysis of a compressed bistable buckled beam*, Sensors and Actuators A: Physical **69**, 212 (1998).

[72] T. G. Abott. *Generalizations of Kempe's universality theorem*, Master's thesis, Massachusetts Institute of Technology (2008). hdl:1721.1/44375.

[73] C. Beentjes. *Symmetry-Breaking in Patterned Elastic Sheets*, Bachelor's thesis, Leiden University (2014).

[74] T. Mullin, S. Deschanel, K. Bertoldi, and M. C. Boyce. *Pattern transformation triggered by deformation*, Phys. Rev. Lett. **99**, 084301 (2007).

[75] Y. Kuznetsov. *Elements of Applied Bifurcation Theory*, Springer US (2004)

[76] J. E. Marsden and T. J. R. Hughes. *Mathematical Foundations of Elasticity*, Dover Publications (1994)

[77] M. F. Schumaker and W. Horsthemke. *Imperfect pitchfork bifurcation with weak noise and an application to superfluid turbulence in liquid helium*, Phys. Rev. A **36**, 354 (1987).

[78] J. Murdock. *Selected Topics in Local Bifurcation Theory*, Normal Forms and Unfoldings for Local Dynamical Systems , 339 Springer (2003).

[79] R. Lakes. *Foam structures with a negative PoissonâĂŹs ratio*, Science **235**, 1038 (1987).

[80] J. N. Grima and K. E Evans. *Auxetic behaviour from rotating squares*, J. Mater. Sci. Lett. **19**, 1563 (2000).

[81] J. N. Grima and K. E Evans. *Auxetic behaviour from rotating triangles*, J. Mater. Sci. Lett. **10**, 3193 (2006).

[82] D. Attard and J. N. Grima. *Auxetic behaviour from rotating rhombi*, Phys. Status Solidi (b) **245**, 2395 (2008).

[83] A. Grant. *Hinged Tessellations* , http://algrant.ca/projects/hinged-tessellations/.

[84] Y. Wang, Z. Luo, N. Zhang, and T. Wu. *Topological design for mechanical metamaterials using a multiphase level set method*, Struct. Multid. Opt. **54**, 937 (2016).

[85] N. T. Kaminakis, G. A. Drosopoulos, and G. E. Stavroulakis. *Design and verification of auxetic microstructures using topology optimization and homogenization*, Arc. App. Mech. **85**, 1289 (2015).

[86] A. Bacigalupo, M. Lepidi, G. Gnecco and L. Gambarotta. *Optimal design of auxetic hexachiral metamaterials with local resonators*, Smart Mech. Struct. **25**, 054009 (2016).

[87] J. C. Maxwell. *On the calculation of the equilibrium and stiffness of frames*, Phil. Mag. **27**, 294 (1864).

[88] C. R. Calladine. *Buckminster Fuller's 'Tensegrity' structures and Clerk Maxwell's rules for the construction of still frames*, Int. J. Solids Struct. **14**, 161 (1978).

[89] W. G. Ellenbroek, V. F. Hagh, A. Kumar, M. F. Thorpe, and M. van Hecke. *Rigidity Loss in Disordered Systems: Three Scenarios*, Phys. Rev. Lett. **114**, 135501 (2015).

[90] R. Poli, J. Kennedy, and T. Blackwell. *Particle swarm optimization*, Swarm Intell. **1**, 33 (2007).

[91] Y. Shi and R. Eberhart. *A modified particle swarm optimizer*, IEEE Int. Conf. on Evol. Comp. Proc. (1998).

[92] J. Nocedal and S. Wright. *Numerical Optimization*, Springer US (2006).

[93] P. Moritz, R. Nishihara, and M. Jordan. *A Linearly-Convergent Stochastic L-BFGS Algorithm*, AISTATS **51**, 249 (2016).

[94] J. Shewchuk. *An introduction to the conjugate gradient method without the agonizing pain*, Technical report, School of Computer Science, Carnegie Mellon University, Pittsburgh, PA (1994). URL https://www.cs.cmu.edu/ jrs/jrspapers.html.

[95] A. Chatterjee and P. Siarry. *Nonlinear inertia weight variation for dynamic adaptation in particle swarm optimization*, Comp. Oper. Res. **33**, 859 (2006).

[96] A. Nickabadi, M. M. Ebadzadeh, and R. Safabakhsh. *A novel particle swarm optimization algorithm with adaptive inertia weight*, App. Soft Comp. **11**, 3658 (2011).

[97] M. Pant, R. Thangaraj, and A. Abraham. *Particle Swarm Optimization: Performance Tuning and Empirical Analysis*, Found. of Comp. Intell. **3**, 101 Springer (2011).

[98] A. L. Gutierrez, M. Lanza, I. Barriuso, L. Valle, M. Domingo, J. R. Perez, and J. Basterrechea. *Comparison of different PSO initialization techniques for high dimensional search space problems: A test with FSS and antenna arrays*, Ant. and Prop. (EUCAP), **5**, 965 Springer (2011).

[99] *The Lisa Cluster*, URL https://userinfo.surfsara.nl/systems/lisa.

[100] A. E. Eiben, R. Hinterding, and Z. Michalewicz. *Parameter control in evolutionary algorithms*, IEEE Trans. Evolu. Comp. **3**, 124 (1999).

[101] D. Chicco. *Ten quick tips for machine learning in computational biology*, BioData Mining **10**, 1 (2017).

[102] J. W. Sammon. *A non-linear mapping for data structure analysis*, IEEE Trans. Comp. **18**, 401 (1969).

[103] B. Lerner, H. Guterman, M. Aladjem, I. Dinstein, and Y. Romem. *Feature extraction by neural network nonlinear mapping for pattern classification*, In Proceedings of 13th International Conference on Pattern Recognition, 1051 (1996).

[104] J. B. Lee, S. Peng, D. Yang, Y. H. Roh, H. Funabashi, N. Park, E. J. Rice, L. Chen, R. Long, M. Wu, and D. Luo. *A mechanical metamaterial made from a DNA hydrogel*, Nat. Nano. **7**, 816 (2012).

[105] R. M. Neville, F. Scarpa, and A. Pirrera. *Shape morphing Kirigami mechanical metamaterials*, Sci. Rep. **6**, 31067 (2012).